On the Estimation of Physical Roughness of a Marginal Sea Ice Zone Using Remote Sensing

Mukesh Gupta

A thesis submitted to the Faculty of Graduate Studies of

The University of Manitoba

in partial fulfillment of the requirements for the degree of

DOCTOR OF PHILOSOPHY

Department of Environment and Geography

UNIVERSITY OF MANITOBA

Winnipeg

Abstract

The surface roughness of both open water and sea ice cover of the marginal ice zone (MIZ) in the Arctic Ocean change as a function of space and time. The MIZ roughness controls many aspects of mass, gas, and energy fluxes across the ocean-sea ice-atmosphere (OSA) interface, all of which are currently being impacted by a changing climate. The rapid reduction of sea ice in the Arctic in the past few decades has resulted in a MIZ consisting of variable sea ice roughness that necessitates improved methods for observations using ice-based, shipborne, airborne, and spaceborne platforms. This thesis is an attempt to provide insight into improved techniques for the detection and classification of various MIZ roughnesses in the southern Beaufort Sea using state-of-the-art *in situ* and satellite-based microwave remote sensing methods. The analysis of variance (ANOVA) of the polarimetric backscattering coefficients of sea ice yields statistically significant, separable ice classes. The ANOVA of the root-mean-square height and brightness temperatures (37 and 89 GHz) of sea ice do not yield any ice classes. Polarimetric coherences and ratios at C-band (5.5 GHz) have shown potential in discriminating sea ice roughness. A proposed two-dimensional (2D) backscattering model of surface roughness (by incorporating deviation in the orientation (i.e. the ice slopes) in azimuth and range direction) further shows the dependence of circular coherence, a discriminator of roughness, on both the surface roughness and sea ice dielectric properties. The thesis provides a new 2D formula for the relationship between sea ice slopes in azimuth and range direction.

Microwave brightness temperature of open water is significantly correlated with wave height but not with the wind speed, having the strongest correlations for the horizontal polarization channel at both 37 and 89 GHz. Analysis of AMSR-E brightness temperature at 89 GHz and root-mean-square height (spring to melt onset) shows a significant correlation between the two, for spatial scale of 1–4 km. This thesis provides a modified formula for the relationship between non-dimensional form of energy and wave age at wind speeds 0–10 m/s. The brightness temperature (April–June) of sea ice at horizontal polarization of 89 GHz is found to decrease with increasing physical roughness, and is attributed to the dominant contributions from rapidly varying thermodynamic properties of snow-covered sea ice during the melt season. I also found that the changes in sea ice surface dielectric properties occur much faster temporally than those detected by satellite sensor making it difficult to interpret ice signatures at sub-pixel level (< 5.4 km). A combined analysis of physical roughness, active polarimetry and passive microwave emission of MIZ at compatible spatial and temporal scales has led to improved understanding of the behavior of the Arctic MIZ.

Acknowledgements

At the outset, I would like to take this opportunity to gratefully acknowledge the logistical and financial support, from my supervisor, Dr. David G. Barber. I would also like to thank Dr. John (Jay) Doering, Dr. Jens Ehn, and Dr. Tim Papakyriakou for their academic support, feedback, and encouragement as a member of my Ph.D. evaluation committee. I would also like to thank Dr. Monique Bernier for fulfilling the role of an external examiner for my Ph.D. oral examination. I am thankful to Dr. Ronald Stewart, Head and Dr. Michael Campbell, acting Head, the Department of Environment and Geography for providing support at the department level.

The International Polar Year (IPY)–Canada, ArcticNet, the Natural Sciences and Engineering Research Council (NSERC), and the Canada Research Chairs (CRC) Program, which provided funding for the Circumpolar Flaw Lead (CFL) System Study project, are acknowledged. I gratefully thank Canadian Coast Guard crew of *Amundsen* for their exceptional support in the acquisition of data at sea during overwintering in the Arctic. I am thankful to Dr. Roger DeAbreu for providing valuable comments and suggestions for an assessment of my Ph.D. proposal. Thanks are also due to Rosenstiel School of Marine and Atmospheric Science (RSMAS), University of Miami for lending ship-based laser system, called LAWAS (Laser Wave Slope). I would like to thank Dr. Matthew Asplin, Dr. Brent Else, Dr. Byong Hwang, Bruce Johnson, Kyle Swystun, and Dr. Sarah Woods for their support with ship-based laser system. I am thankful to our colleagues, fellow scientists and students from

various Canadian and international institutes and universities who helped in various capacities during the course of my Ph.D.

The list is long; it is not possible for me to list by name here all who have helped. I would like to thank CEOS scientists and students, in particular, Dr. Randall K. Scharien for his valuable assistance with manuscripts (Chapter 4 and 5), personal communication and scientific discussions. The scholarly conversations with Dr. Jennifer V. Lukovich provided stimulus and encouragement; and her help in editing my Ph.D. Candidacy report and thesis is gratefully acknowledged. Scientific conversations with Dr. Simon Prinsenberg and his contributions to helicopter roughness data were invaluable. Discussions on microwave scattering, and radar remote sensing with Alexander Komarov were very useful. I would like to extend my sincere gratitude to my colleague Dr. Klaus P. Hochheim, who lost his life in a helicopter crash in the Canadian Arctic in September of 2013 while conducting sea ice research.

I would like to personally thank Wayne Chan for interesting technical conversations. The technical expertise of Vlad Petrusevich provided great help during hardware maintenance. I am thankful to the administrative staff of CEOS, Department, and Faculty of Graduate Studies for logistics. I am grateful to Late Ms. Pat Gutoski, Graduate Assistant, who I first met upon arrival in Canada for enrolment into my Ph.D. program in 2007. Words cannot express my gratitude to my own family in India; and Audrey and Bert Epp family, who hosted me upon my arrival to Canada, under the Welcome Family program of the University of Manitoba.

August 14, 2014, Winnipeg Mukesh Gupta

Table of Contents

List of Tables

List of Figures

List of Copyrighted Material

My thesis is of the 'sandwich' style, which is typical of M.Sc. and Ph.D. students who are working within the CEOS Arctic Group.

I reproduced Chapter-3 of this thesis with minor modifications from Gupta et al. (2014)– [Detection and classification of surface roughness in an Arctic marginal sea ice zone, *Hydrological Processes*, 28(3), 599–609, doi:10.1002/hyp.9593], with permission from John Wiley and Sons, Ltd.

I reproduced Chapter-4 of this thesis with minor modifications from Gupta et al. (2013)– [C-band polarimetric coherences and ratios for discriminating sea ice roughness, *International Journal of Oceanography*, vol. 2013, Article ID 567182, 1–13, doi:10.1155/2013/567182]. Copyright © 2013 Mukesh Gupta et al. This is an open access article distributed under the Creative Commons Attribution License, which permits unrestricted use, distribution, and reproduction in any medium, provided the original work is properly cited.

I reproduced Chapter-5 of this thesis with minor modifications from Gupta et al. (2014)– [Microwave emission and scattering from ocean surface waves in the southern Beaufort Sea, *International Journal of Oceanography*, vol. 2014, Article ID 872342, 1–12, doi:10.1155/2014/872342]. Copyright © 2014 Mukesh Gupta et al. This is an open access article distributed under the Creative Commons Attribution License, which permits unrestricted use, distribution, and reproduction in any medium, provided the original work is properly cited.

I reproduced Chapter-6 of this thesis with minor modifications from Gupta et al. (2014)– [Sub-pixel evaluation of sea ice roughness using AMSR-E data, *International Journal of Remote Sensing*, 2014, doi:10.xxxx/xx, Manuscript# TRES-PAP-2014-0395, *in review*].

Chapter 1

Introduction

1.1. Rationale and Context

Satellites records, starting in 1970s, and sea-truth observations of the Arctic have confirmed the rapid shrinkage in sea ice volume in the northern hemisphere (Kwok and Cunningham, 2010; Kwok and Rothrock, 2009; Nghiem et al., 2007; Stroeve et al., 2012, 2014). The perennial sea ice regime that dominated the Arctic is gradually turning into a seasonal ice regime resulting in more prevalent marginal ice zones (MIZs) (Barber et al., 2009), which are the portions of the sea ice cover sufficiently near to the ice-free ocean such that interactions with the open sea result in the modification of the properties of the ice so that they are different from properties deeper within the pack (Weeks, 2010). MIZs are highly deformed and are known for enhanced dynamics and vertical exchange of energy, mass, and momentum between ocean-sea ice-atmosphere (OSA), termed OSA interaction (Claussen, 1991). Recent studies have highlighted the occurrence of changing sea ice roughness, circulation, meteorological conditions, and OSA interactions throughout the Arctic (Barber and Hanesiak, 2004; Esau, 2007; Hutchings and Rigor, 2012; Lukovich and Barber, 2005; Moore et al., 2014; Pizzolato et al., 2014). Satellite-based algorithms for the detection of multiyear ice are no longer applicable within a new ice regime, because these algorithms misinterpret the type of ice regime actually found in

the Arctic (Barber et al., 2009). Rough sea ice is a habitat for numerous animals that live on, within, and under sea ice (Stirling et al., 2004). Recent burgeoning interest in hydrocarbon exploration in the Arctic urgently requires more knowledge of ice dynamics in the MIZ. The thinning and shrinking sea ice cover in the Arctic necessitates further investigation of physical processes in the MIZs and improved understanding of how the physical roughness and enhanced OSA interactions in the MIZ affect the Arctic and global climate systems.

There is little knowledge of the processes that govern the spatial and temporal evolution of the physical roughness of the MIZ. Surface waves play a significant role in creating surface roughness; however, there are gaps in understanding how surface waves evolve within the MIZ as a function of fetch (Doble and Bidlot, 2013; Williams et al., 2013). More research is required to understand the role of wave roughness on the contributions of thermodynamic forcing in MIZ evolution. It is also important to understand how large period waves (swell) create roughness in the MIZ because large period waves can easily break up sea ice into fragments (Asplin et al., 2012). The increased number of ice floes in the MIZ and their distribution respond to surface waves to create enhanced surface roughness (Lu et al., 2008). All these processes and dynamics create feedback mechanisms that become important in the emergence of a rough MIZ. Many of these processes can be understood only through sea-truth (*in situ*) observations; however, some scale-dependent processes can be better understood from satellite observations.

Microwave observations of sea ice tell us its evolution mechanism, which forms the basis for our understanding of the evolution of associated physical processes in the MIZ.

Satellite-based microwave observations not only cover large spatial extents but also provide useful data under all-weather conditions. Active microwave remote sensing of first-year and multiyear ice (both seasonally rough and smooth classes of each) at varying frequencies, particularly C-band (5.5 GHz), and polarizations, is still an evolving area of research (Geldsetzer and Yackel, 2009; Kim et al., 2012). Microwave polarimetry is a more recent tool and much less is known as to how this type of energy interacts with sea ice surface roughness (Wakabayashi et al., 2004). Sea ice roughness affects passive microwave emission differently depending on microwave frequency, polarization, and sensor-surface geometry. There is still a perplexing ambiguity in deciphering dielectric and surface roughness contributions from sea ice to the passive microwave emissions detected at the satellite sensor due to insufficient *in situ* data suitable for such work (Hong, 2010; Stroeve et al., 2006). Helicopter-based laser profiling and LiDAR (Light Detection and Ranging) imaging of rough sea ice further aid these investigations (Haas et al., 2009; Rivas et al., 2006).

This thesis addresses to minimize this ambiguity by utilizing sea-truth, airborne, and spaceborne microwave data with focus on physical roughness of the MIZ. There is a need for robust techniques to adequately detect and classify sea ice types and roughness within the MIZ. Polarimetric classification and development of associated techniques, e.g., polarimetric coherences and ratios are of much interest. An analysis of surface wave conditions in the vicinity of the MIZ and its linkages with *in situ* polarimetric parameters will provide insight into wave transition from an open sea, through the MIZ, into a fully ice-covered ocean. Finally, the satellite-based passive microwave observations of the evolution of snow-covered first-year ice, and rapidly changing dielectrics and physical

roughness of ice from spring to melt onset is anticipated to fill some gaps in understanding complex processes of the Arctic.

1.2. Objectives

The research work in this thesis was conducted as part of Circumpolar Flaw Lead (CFL) System Study (Barber et al., 2010) overwintering project of the fourth International Polar Year (IPY) program (2007–08) aboard the Canadian Research icebreaker *Amundsen*. This is the first IPY program since the first satellite-based continuous monitoring of Arctic sea ice started in the mid-1970s. A ubiquitous increase in spatial and temporal extents of the MIZ is now being observed across the length and breadth of the Arctic (Martin et al., 2014; Stroeve et al., 2014), resulting in greater surface roughness (both ocean and sea ice surface roughness) and enhanced OSA interactions in the MIZ. The overarching goal of this research is to understand the physical roughness of the southern Beaufort Sea, which is a highly complex MIZ, using microwave remote sensing methods, which include ship-based observations and satellite-based passive microwave emissions assisted with helicopter-based laser roughness measurements from the mixed ice-open water environment. To achieve this goal, four sub-objectives of this research utilizing microwave remote sensing techniques, are addressed:

1. To detect and classify sea ice roughness purely based on statistical analysis of ship-based and airborne laser altimeter, and ship-based microwave methods

2. To discriminate ice surface roughness using ship-based polarimetric active and passive microwave methods and to improve one-dimensional model of ice roughness.

3. To validate relationships between geophysical variables associated with open water surface roughness (wave height, power spectral density) and microwave backscattering and emission.

4. To evaluate the sub-pixel level (< 5.4 km) linkages between physical roughness and AMSR-E brightness temperature at 89 GHz from spring to melt onset.

1.3. Thesis Structure

This thesis contains seven chapters. Chapter-1 provides a rationale and broad purview of this research and its scientific significance. Chapter-2 introduces the reader to a comprehensive background and literature review, which explores the physical processes that give rise to roughness in the MIZ; why it is important in terms of various OSA interactions; and how microwave remote sensing methods can be used to address physical surface roughness of the MIZ. Chapters 3–6 are research papers that make individual chapters, and are designed to address thesis objectives 1–4, respectively.

Chapter-3 addresses thesis objective-1 and examines the detection and classification of statistically separable sea ice classes in the MIZ through a range of spatial and temporal scales. The analysis of variance (ANOVA) has been performed on the helicopter-based and ship-based laser roughness data, ship-based active and passive microwave data, to

achieve statistically significant classes of sea ice types based on differences in variances. This work has been peer-reviewed and published in the journal *Hydrological Processes*:

Gupta, M., Barber, D. G., Scharien, R. K., and Isleifson, D. (2014). Detection and classification of surface roughness in an Arctic marginal sea ice zone. *Hydrological Processes*, 28(3), 599–609, doi: 10.1002/hyp.9593.

Chapter-4 addresses thesis objective-2 and evaluates the utility of C-band polarimetric backscatter, coherences and ratios as a discriminator of sea ice surface roughness. Circular, co-, and cross-polarized coherences and polarization ratios have been computed for different sea ice surfaces to examine sensitivity to surface roughness. An existing one-dimensional backscatter model has been modified to two-dimensions as an improvement in the model for surface roughness. This work has been peer-reviewed and published in the *International Journal of Oceanography*:

Gupta, M., Scharien, R. K., and Barber, D. G. (2013). C-band polarimetric coherences and ratios for discriminating sea ice roughness. *International Journal of Oceanography*, vol. 2013, Article ID 567182, 1–13. doi:10.1155/2013/567182.

Chapter-5 addresses thesis objective-3 and estimates open water roughness in the southern Beaufort Sea. It investigates the relationships between geophysical variables associated with open water roughness (wave height, spectral density) and microwave backscatter/emission. Active co- and cross-polarization ratios and polarimetric coherences are used to interpret open water roughness. This work has been peer-reviewed and published in the *International Journal of Oceanography*:

Gupta, M., Scharien, R. K., and Barber, D. G. (2014). Microwave emission and scattering from ocean surface waves in the southern Beaufort Sea. *International Journal of Oceanography*, vol. 2014, Article ID 872342, 1–12. doi:10.1155/2014/872342.

Chapter-6 addresses thesis objective-4 and evaluates sea ice roughness at sub-pixel levels (< 5.4 km) using AMSR-E data at 89 GHz channel. The paper uses helicopter-based laser roughness measurements in the southern Beaufort Sea to investigate how it corresponds to passive microwave brightness temperature as detected by the satellite at the same time. Temporal evolution of passive microwave signatures from spring to summer melt (April–June) has been studied. This work is in review and has been submitted to the *International Journal of Remote Sensing*:

Gupta, M., and Barber, D. G. (2014). Sub-pixel evaluation of sea ice roughness using AMSR-E data. *International Journal of Remote Sensing*, Manuscript# TRES-PAP-2014-0395 (*in review*)

Chapter-7 summarizes the thesis and its findings, and suggests avenues of future research.

Appendix-A describes the contributions of individual authors of the journal papers presented in the Chapters 3–6.

Appendix-B lists my contributions made in several other peer-reviewed publications at the Centre for Earth Observation Science, during my time as a Ph.D. student and Graduate Research Assistant at the University of Manitoba, Winnipeg.

Chapter 2

Background and Literature Review

2.1. Introduction

2.1.1. What is Roughness?

Ocean surface roughness is a direct manifestation of physical processes that occur across the ocean-sea ice-atmosphere (OSA) interface (Gupta, 2013). These processes may occur from above the ocean surface (wind forcing, snow storms, atmospheric turbulence), and from beneath the ocean surface (ocean currents, biological production, various types of ocean circulation). In a rapidly changing Arctic environment due to rapid sea ice reduction in recent years (Barber et al., 2009), further knowledge and understanding of ocean surface roughness has become of paramount importance because it allows for an understanding of the processes that occur in the OSA system.

Physical roughness is the vertical displacement of ocean surface from the mean sea level. It can be measured in different ways; for example, by taking the average of surface heights or as root-mean-square (rms) height of the surface. The geometrical properties of a rough sea ice surface can be explained in terms of two important parameters: rms surface height, and correlation length. Physical roughness depends on the direction of measurement and surface orientation. Ocean surface roughness is estimated from the wave slope and significant wave height as will be described in later sections. The most

common methods for measuring physical roughness utilize surface-based, ship-based, airborne, and spaceborne laser altimeter/profiler.

Statistical Description

No two surfaces are identical; however, they may exhibit similar statistical properties. The distribution $p(h)$, of surface heights h, is usually assumed to be Gaussian (Longuet-Higgins, 1957). σ is the standard deviation of surface heights (Eq. 2.1). The surface profiles are different because of the different length scales over which height changes occur along the surface.

$$p(h) = \frac{1}{\sigma\sqrt{2\pi}} exp\left(-\frac{h^2}{2\sigma^2}\right). \quad (2.1)$$

Most work with surface roughness analysis involves measurement of single parameter, i.e. surface height. However, a single parameter is insufficient to specify surface roughness and therefore, frequency, amplitude, and autocorrelation components must be considered to understand the anisotropy and surface orientation. The correlation length is a measure of the range over which fluctuations in one region (e.g., surface profile) are correlated with those in other region. It describes the change of surface height with distance along the surface. Two points that are separated by a distance larger than the correlation length will each have fluctuations, which are relatively independent. The correlation length L, and rms height σ, are interrelated with the following empirical relationship for sea ice (Manninen, 1997):

$$L = k_0 exp\left(-\frac{a}{b}\right)\sigma^{1/b}. \tag{2.2}$$

where k_0, a, and b are the regression coefficients.

With varying correlation lengths for same rms height, a surface may be distinguished by its autocorrelation function. The autocorrelation coefficient can be computed using the following formula,

$$a_k = \frac{\sum_{t=1}^{N-k}(x_t - \bar{x})\,(x_{t+k} - \bar{x})}{\sum_{t=1}^{N}(x_t - \bar{x})^2}, \qquad k = 0, 1, 2, \ldots \tag{2.3}$$

where x is the sample height, N is total number of samples, t denotes serial number in the data series and k is increment. Studies have shown that unless the discretisation interval is at least as small as one tenth of the correlation length then the full exponential nature of the surface will not be measured (Ogilvy and Foster, 1989).

Another method of measuring surface roughness is by Fourier analysis, i.e. to represent the surface in terms of sinusoids, which have different frequencies and amplitudes. The power spectral density function (power spectrum) describes the intrinsic properties of the surface. It is obtained from the Fourier transform of the surface profile $x(t)$,

$$X(k) = \frac{1}{N}\sum_{t=1}^{N} x(t)\exp\left(-\frac{j2\pi kt}{N}\right), \qquad k = 1, \ldots, N \tag{2.4}$$

The power spectral density of roughness is expressed as $|X(k)|^2$ (m^2), where k is the spatial frequency (m^{-1}); t is time series; N is number of samples; x is the surface height profile; $j = \sqrt{-1}$. Eq. (2.4) characterizes the spectral behavior of sea ice roughness detected using laser altimeters (Rivas et al., 2006).

2.1.2. Why is Roughness Important?

The roughness of the sea has been a topic of investigation from the perspectives of overcoming difficulties in navigation and understanding its impact on the regional and global climate system. In an ice-covered marine environment, surface roughness also plays a role in creating a habitat for a number of organisms and animals that live within, above, and/or beneath the sea ice. In recent years, the growing interest in hydrocarbon exploration in the Arctic region has necessitated active research on sea ice roughness and motion for the purpose of developing infrastructure to cope with hazards potentially caused by sea ice.

The ocean surface, be it sea ice or mixed ice/open water, is always rough in practical terms. Ocean surface roughness, for the sake of understanding its relationship with related physical processes can be described according to three distinct surface types: ice-covered ocean surface, MIZ, and open water (Figure 2.1). The dominant processes of energy, mass and momentum exchange occur in the three surface types at different temporal and spatial scales. The measurements of roughness in these three environments require different instrumentation and techniques to individually understand how surface roughness acts to increase the OSA coupling. Some of the widely used methods in this investigation are wind measurements, surface height measurements, and EM energy

response at the OSA interface. Surface-based, airborne, and/or satellite-based instruments are employed to acquire the data at different temporal and spatial scales.

Figure 2.1. Schematic diagram showing various processes and mechanisms in a marginal ice zone environment.

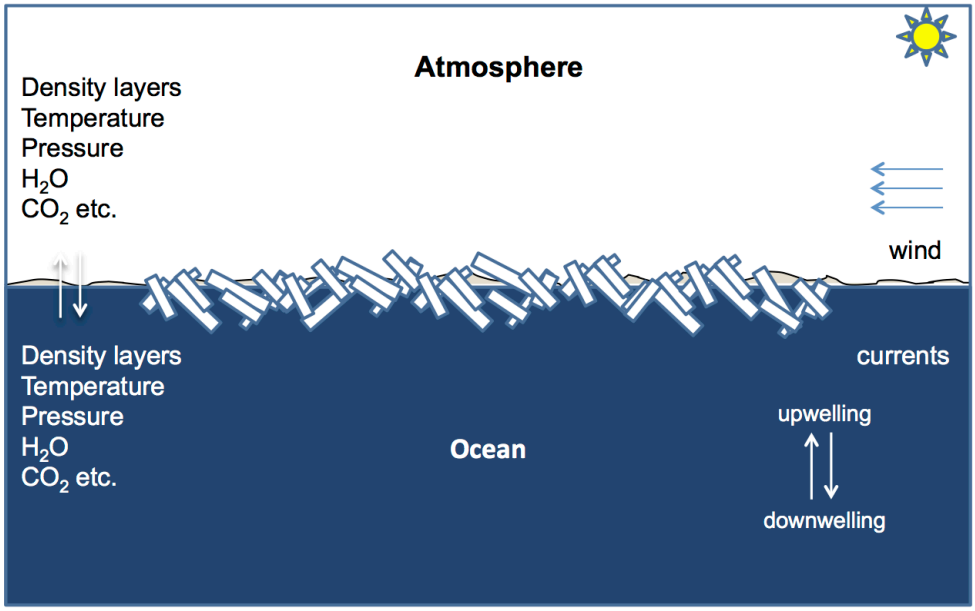

2.2. Physical Processes Creating Roughness in the MIZ

Surface roughness in the context of sea ice is defined as the vertical displacement of ice around a mean ice level at both surface and bottom (Steiner et al., 1999). There are physical processes and mechanisms that simultaneously work in open water, MIZ, and sea ice areas (Figure 2.1). The formation process of sea ice itself creates roughness types at smaller scales. In this section, I describe the physical processes of sea ice, MIZ, and open water regimes at different spatial and temporal scales. These processes ultimately lead to the deformation of ice to create surface roughness.

2.2.1. Ice-Covered Ocean

Sea Ice Formation, Growth, and Decay

The formation of different types of rough sea ice may be described mainly in two parts; first under calm conditions where there is no significant atmospheric or oceanic turbulence, and secondly under the influence of turbulent conditions. Wind forcing and internal stress result in the formation of pressure ridges and severely deformed sea ice. The shape, size, and structural development of sea ice depend mainly on the atmospheric forcing and to a lesser extent on the oceanic forcing.

Figure 2.2. Field photographs of different types of sea ice taken during CFL-IPY Project.

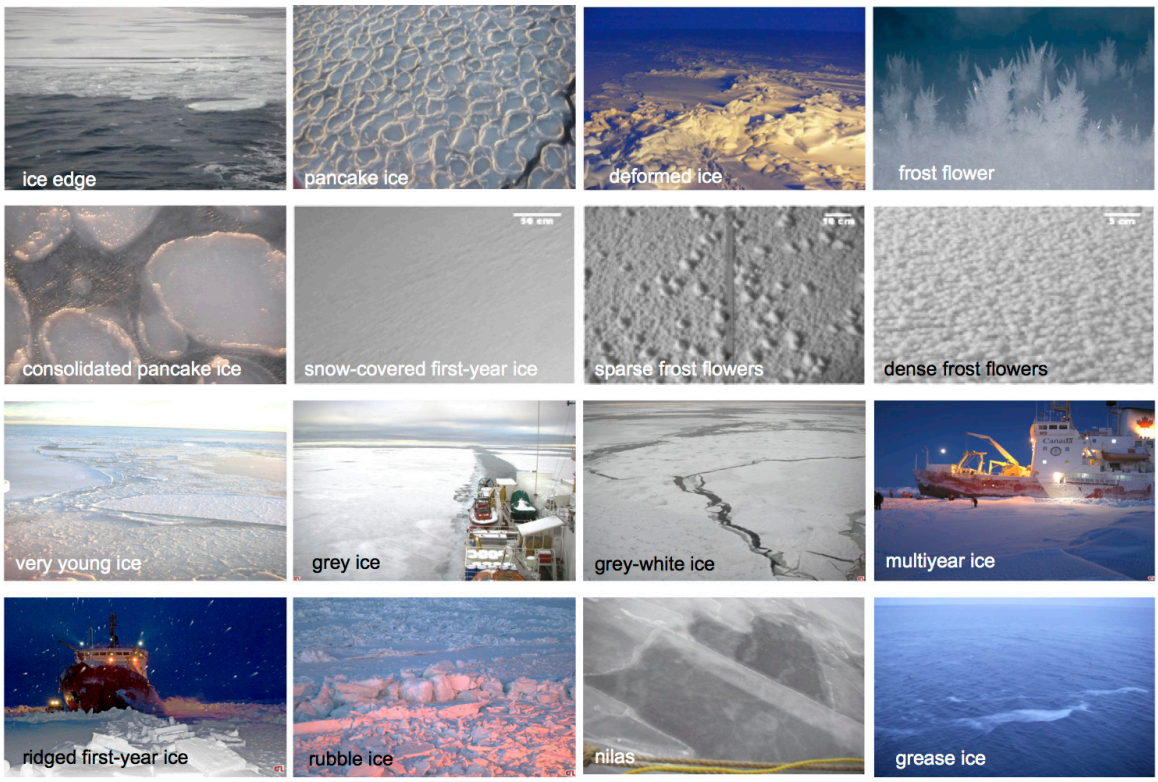

The presence of salts in seawater lowers its freezing point to about –1.8°C (Untersteiner, 1986). Under calm conditions ice crystals begin to form as discs with a

vertical c-axis. The growth of the crystal occurs in a direction perpendicular to the c-axis. With slight turbulence in the water, the crystals break and join together to form a suspension called *grease ice* (Figure 2.2). In calm conditions, this thin layer of grease ice freezes and forms a transparent layer of ice called *nilas*. Nilas further thickens to form congelation ice in its primitive form. Here, roughness of grease ice can only be estimated from the wave height, whereas nilas ice is flat.

Ice formed under turbulent conditions goes through compression due to wave energy and forms an ice type called *pancake ice*. Pancake ice has noticeable small-scale roughness due to upturned peripheries (Martin and Kauffman, 1981). When a large number of pancakes coalesce, an ice type known as *consolidated pancake ice*, which is essentially the first-year ice formed under rough conditions, is formed. Consolidated pancake ice is rough ice and may have considerable measured rms height.

When sea ice grows, the salt does not enter the ice crystal structure, therefore, only pure water is frozen and brine is rejected, but partly trapped in the interstices between crystals. The movement of brine from sea ice follows mainly three mechanisms, e.g., brine migration due to temperature gradients, gravity drainage through interconnected channels, and further expulsion due to freezing around brine pockets. Brine also drains downwards during summer due to flushing caused by fresh water. The salinity of young ice (ice in the transition stage between nilas and first-year ice, 10-30 cm in thickness) is about 10 psu, and that of multiyear ice (defined below) ~0–3 psu. If the ice survives more than two consecutive summers, it becomes completely fresh water multiyear ice free from any salts. This process of formation and growth sees a number of ice roughness types as it goes through different phases.

A significant change in the surface roughness, ice morphology, and topography is observed after the onset of melt in mid-June in the Arctic. The melt water forms a network of ponds over the surface. The depth and area of initially small and shallow melt ponds increase as the summer progresses (Maykut, 1986). Eventually, the melt water drains into the sea through holes called *thaw holes*. The melt water that does not drain through thaw holes refreezes in the fall. This melting and freezing cycle repeats over the years and produces an ice type known as *multiyear ice*. Multiyear ice is less salty and much rougher than the first-year ice.

Rheological Properties of Ice

Ice rheology examines how the stress in ice depends on its material properties and strain (Leppäranta, 2005). Sea ice, with the exception of fast ice (attached to the shore), is always mobile. Some of the major forces acting on sea ice are Coriolis force, ocean currents, and wind forcing. Two most obvious features observed in sea ice are pressure ridges and leads in the pack ice. Ice rheology plays a large role in response to different stresses acting on sea ice.

Ice is polycrystalline and behaves as a viscoelastic solid. However, ice in the MIZ can be explained through different ice rheology representations, for example, plastic (Hibler, 1989) and a rheology based on ice floe mechanics (Shen et al., 1987). Ice has near-zero tensile strength, which means if we apply divergent stresses in two-dimensions, it will dilate and easily break apart. Ice has very high compressive strength, i.e. it is difficult to crush the ice under compression. Ice also has significant shear strength, which implies that when shear stress is applied on ice, it is likely to slip and deform. This shear property

facilitates the main cause of rafting and piling up of ice and the formation of rubble, pressure ridges, and hummocks under the influence of differential forces at the ice edge and in the MIZ due to wind and waves (Leppäranta, 2005).

Ice Motion

The formation of deformed sea ice is closely related to the motion of sea ice. Sea ice moves as per the motion of surface ocean currents at large temporal scales. Local wind forcing causes the sea ice motion at small temporal scales. In both cases, the main driving force is the wind forcing (Leppäranta, 2005). Diverging/converging wind patterns create diverging/converging sea ice motion, which causes ice to deform. Under various forces, the ice moves in the ocean in a divergent or convergent manner thereby creating surface roughness. The forces given below control the motion of sea ice,

$$F = \tau_a + \tau_w + F_C + F_i + F_t, \tag{2.5}$$

where τ_a and τ_w are wind and water drag respectively, F is total force, F_C is Coriolis force, F_i is internal stress, and F_t is sea surface tilt. Four major external forces working on an ice floe control its deformation and movement (Figure 2.3).

Figure 2.3. Various forces acting on an ice floe (directions are arbitrary).

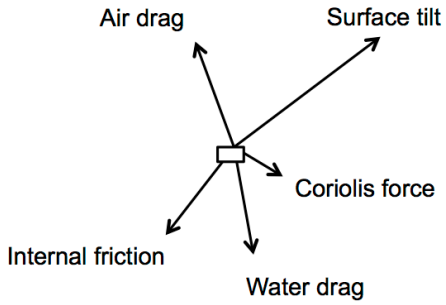

a. Wind forces- a detailed account of wind drag is discussed in the following sections.

b. Water drag- it is the frictional force between ice and seawater, which is controlled by water density, temperature, and underwater currents.

c. Coriolis force- this is one of the precisely calculated forces on sea ice unlike wind and water drag, which are computed using semi-empirical formulae. The Coriolis force arises due to Earth's rotation. An ice floe experiences acceleration caused by rotation of the Earth deflecting the original trajectory of the floe to the right in the northern hemisphere. The magnitude of Coriolis force is given by:

$$F_C = 2m\omega U \sin\phi \tag{2.6}$$

where m is the mass of the ice floe, ω is angular velocity of Earth = 7.272×10^{-5} rad/s, U is ice velocity, and ϕ is latitude. The Coriolis force is also observed in the atmosphere. It is zero at the equator and maximum towards the poles.

d. Other forces are, for example, internal ice stress- it acts on a unit area of ice in an ice floe due to transmitted stress within the ice floe. Winds or ocean currents play a greater role in generating internal stresses in addition to other forces acting on ice. The

net stress can be the result of all the stress vectors on a given ice floe. The sustainability of stress within the ice is dependent on ice thickness distribution and physical properties, which affect the strength of ice cover. Multiyear ice, which is thicker and harder than first-year ice, is likely to sustain greater internal ice stresses.

Free drift also contributes to ice motion explained above. Free drift is defined as the drift of sea ice in the absence of internal friction of ice. In the case when ice is free to move without water friction, well-known cycloid (inertial) motion (also present in water) of ice floes is observed, which is also called *inertial oscillation*. The floe moves in the direction of the wind but it is deflected to the right (in the northern hemisphere) under the influence of the Coriolis force. The period of oscillation equals $T = 2\pi/f = \pi/(\Omega \sin \phi)$, where f is Coriolis frequency, Ω is rotation rate of Earth, and ϕ is latitude. The period is about 12 hours at the poles and it increases toward the equator.

Thermodynamics and Dynamics

Thermodynamic processes along with dynamic processes occurring at the OSA interface control the thickness of sea ice. If the oceanic heat flux exceeds the heat flow through the thick ice, sea ice will melt regardless of the season (Perovich et al., 1989). In an ice-covered ocean, rates of freezing and melting depend on the distribution of ice thickness and open water (leads, polynyas), which, in turn, depends on ice transport (dynamics) (Hibler, 1979). In addition, rates of freezing and melting are also influenced by radiation and heat exchanges with the atmosphere and the ocean. The thermodynamic and dynamic processes are intrinsically linked with each other (Thorndike et al., 1975). Thermodynamic processes make equilibrium by accretion in thin ice areas and by

ablation in the thick areas while dynamic processes make thick pressure ridges and open water areas through convergence and divergence of ice, respectively. Both processes act together at different spatial and temporal scales to modify the surface and bottom of sea ice, and moderate the OSA coupling. Snow cover also contributes to the determination of magnitude and rate of sea ice growth and decay by controlling the thermodynamics (Maykut, 1978). The physical properties of snow affect the conductive and radiative energy exchange across OSA interface (Barber and Nghiem, 1999). This thesis deals with the effects of snow roughness, how it affects total physical roughness as detected using remote sensing to be discussed in the later sections.

Snow Roughness

Sea ice is usually covered by snow, which plays an important role in modifying the surface roughness at smaller as well as larger scales (Figure 2.4). It also alters the albedo (ratio of reflected to incident flux density) of the ice surface. Knowledge of the snow roughness is necessary for accurately modeling the turbulent heat fluxes (Andreas, 1987). The link between surface roughness of snow and the associated turbulent fluxes, and aerodynamic roughness length is a challenging task and is an open research area (Manes et al., 2008).

Figure 2.4. Cartoon showing influence of snow layer on sea ice.

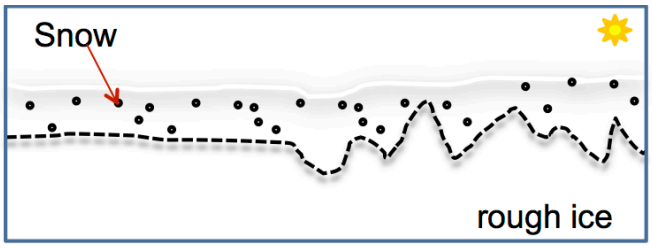

2.2.2. Open Water

Basics

The manifestations of physical roughness in open water are whitecaps, wave height, sea spray, swell, and wave slope. Here, I describe major physical mechanisms operating in open waters that are responsible for surface roughness.

Most waves are driven by the wind. Waves are moving energy traveling along the ocean-atmosphere interface, often transferring energy from a storm far out at sea over distances of several thousand kilometers. If the wave steepness exceeds 1/7, the wave breaks because the wave is too steep to support itself (Trujillo and Thurman, 2011). The wave can break anywhere along the ice edge, shoreline or out at sea. As the wave travels, the water passes the energy along by moving in a circle. The diameter of these circles is equal to the wave height. The circular orbital motion dies out quickly below the surface. This depth is called the *wave base* and it is equal to one-half of the wavelength measured from still water. Only wavelength controls the depth of the wave base, so the longer the wave, the deeper is the wave base. If the water depth is greater than the wave base, the waves are called *deep-water waves*. Deep-water waves have no interference with the ocean bottom. These include all wind-generated waves in the open ocean, where water depths far exceed wave base.

Wave energy is transferred depending on wind speed, which controls how fast waves (i.e. change in roughness) move. Wave speed is more correctly known as *celerity*, which is used only in relation to waves where no mass is in motion, just the waveform. The speed of deep-water waves is mainly dependent upon wavelength. Wave speed, $S = 1.25\sqrt{L}$, where L is wavelength. This means, the longer the wavelength, the faster the wave travels. Waves, in which depth is less than one-twentieth of the wavelength, are called *shallow-water waves*. These waves touch the ocean floor, which interferes with the wave's orbital motion. The wave speed, $S = 3.13\sqrt{d}$, where d is water depth. This means deeper the water, the faster the wave travels (Trujillo and Thurman, 2011).

A wind-generated wave having its origin in a windy region of the ocean may travel across great expanse of open water without subsequent aid of wind, and it terminates when it breaks to release its energy either at shore, ice edge, or open water. As the wind blows over the ocean surface, it creates pressure and stress. These factors deform the ocean surface into small commonly called *ripples or capillary waves*. As the capillary wave develops, the sea surface takes on a rougher appearance, which is further developed into gravity waves (Figure 2.5). Further energy imparted by the wind increases the height, length, and speed of the wave.

Figure 2.5. Wave development from capillary to gravity wave with the wind.

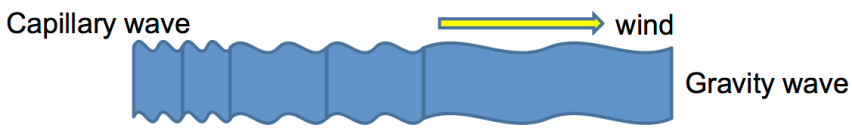

A minimum fetch and duration of wind is required for waves to grow for given wind speed. Waves cannot grow because an equilibrium condition, called *fully developed sea*,

is achieved. In this situation, waves lose as much energy breaking as whitecaps under the force of gravity as they receive from the wind (Trujillo and Thurman, 2011). The longer wavelengths waves move faster than the waves with shorter wavelengths. Due to this progression, the sorting of waves based on wavelengths occurs, in other words, it is called *wave dispersion*. As stated, longer wavelength waves travel faster and move toward the shore covering large distances even after wind speed has diminished. In this situation, when longer waves travel faster than the wind, the wave steepness decreases. Such long wavelength waves are called *swells*, which are uniform and carry large amount of energy with them. Swells can be responsible for breaking up large ice floes in very short duration of time (Asplin et al., 2012). High waves that have periods up to 60 s have been observed in the Arctic (Hunkins, 1962).

Wind-wave coupling

The surface transfer processes of momentum, sensible heat, and humidity are strongly affected by the movement and distortion of the ocean surface by the wind, i.e. by wind-generated waves. These wave motions enhance transfer rates. The wind-generated waves, being the visual manifestation of the air-sea interaction, play an active role in process of coupling with the atmosphere (Geernaert, 1999).

Janssen (1989) introduced a wind-generated wave theory following Miles (1957) who applied the theory of wave growth for a wave spectrum to find that sea surface roughness is dependent on the ratio of the drag and total wind stress. Charnock relation (Charnock, 1955), i.e. roughness proportional to square of friction velocity, considers short gravity waves, and irregularities such as foam. A reliable statistical description of the short wave

spectrum is of crucial importance to better determine the exchange of momentum and heat between the ocean and the atmosphere, as the capillary and gravity waves support a significant fraction of the total stress at the sea surface (Kudryavtsev et al., 1999; Makin and Kudryavtsev, 1999).

The surface fluxes of sensible heat and humidity (latent heat flux) can be evaluated in the frame of the wind-generated wave theory. It has been shown by Makin and Mastenbroek (1996) that the different wind-speed dependences of the drag coefficient and the exchange coefficient for sensible heat can be explained by the difference in exchange mechanisms of momentum and heat at the sea surface. Organized wave-induced motions correlated with the waves (the form drag) transport the momentum, and molecular processes transport the heat. The sensible heat and humidity flux above waves are thus determined by the diffusivity of turbulence, which is affected by waves. In this case, waves have only indirect impact on heat (sensible and latent) fluxes. This explains a well-established experimental fact that the sensible heat and humidity exchange coefficients over the sea are not much dependent on the wind speed (Anderson, 1993; DeCosmo et al., 1996). However, waves can directly influence sensible heat and humidity fluxes.

Sea Spray, Swell, and Whitecaps

Foam, sea spray, swell, wave height, and whitecaps are important surface roughness elements in open water. Ocean currents and winds are the dominant factor in generating these elements. These enhance the turbulent OSA transfer of mass and energy by increasing the ocean surface area (Andreas, 1992). The presence of these elements on the

ocean surface moderates the radiative transfer significantly. The spray droplets evaporate and can change the balance of sensible heat and moisture in the marine surface boundary layer. The sea spray, whitecap coverage, and surface waves are interlinked. The effect of the evaporating droplets on heat and humidity transfers in the marine surface boundary layer is determined by the evaporation function. The spray droplets concentration is related to the bubble production at the sea surface, and the latter to the whitecap coverage of the sea. This whitecap coverage can be calculated directly from the wave spectrum, via the dissipation due to breaking function. In this way the heat fluxes in presence of sea spray can be calculated from the properties of the sea surface roughness (wave breaking) and peculiarities of the momentum exchange above waves (Geernaert, 1999).

Significant wave height is the mean of the highest one-third wave heights observed at a location in the sea. It is computed as the zeroth moment of the wave spectrum. The average energy density E, per unit area is related to significant wave height, H_{m0} by (Holthuijsen, 2007):

$$E = \frac{1}{16}\rho g H_{m0}^2. \tag{2.7}$$

where ρ is water density, g is gravitational acceleration.

Wave height is directly related to the energy in a wave. As waves gain energy, their steepness increases. When wave height reaches a critical value of one-seventh of wavelength, wave breaks and whitecaps form. Whitecaps are generated by the ocean wave breaking due to excessive wind energy supplied to the ocean surface (Wu, 1979). Whitecap fraction of sea surface W, is empirically related to the wind speed, U_{10} by:

$$W = \alpha U_{10}^{3.75}. \quad (2.8)$$

where coefficient, α varies from 1.3 to 2.9.

Fetch in Open Ocean

The length of time and distance on the ocean surface (fetch) over which the wind blows in one direction determine the intensity and longevity of the generated effects on the ocean surface. The ocean surface remains smooth at zero wind speed. Fetch-limited sea (when the range of frequencies and wave heights are limited, and the wave heights are less than those of a fully developed sea) occurs when the fetch length is too short and the wind is not in contact with the waves over a distance sufficient to impart the maximum energy to the waves.

Momentum Transfer

Momentum exchange across the OSA interface is an important mechanism in moderating the ocean surface roughness. The physical process behind momentum exchange is the turbulence in oceanic and atmospheric boundary layers. Turbulence is an energetic, rotational, and random motion that results in the dispersion and transfer of momentum at rates far higher than those through molecular diffusion alone (Thorpe, 2007).

Momentum exchange across OSA interface is usually parameterized in terms of air-water drag coefficient. Air-water drag coefficient over the ocean surface is further dependent on a number of geophysical variables including water depth, wave steepness

(Toffoli et al., 2012), directional wave spreading (Ting et al., 2012), wind stress, and the presence of ice floes (Lu et al., 2011).

The air-ice drag coefficient is one of the main parameters required for the modeling of sea ice dynamics. Air-ice drag coefficients depend on the sea ice roughness characteristics in the turbulent boundary layers of ocean and atmosphere (Leppäranta, 2005). The turbulent fluxes are measured using a number of methods such as eddy correlation method (Shirasawa and Ingram, 1997; Fujisaki et al., 2009), profile method (Andreas and Claffey, 1995; McPhee, 2002), and inertial dissipation method (Leavitt, 1980; Edson et al., 1991).

2.3. MIZ Roughness Influence on the Ocean-Sea Ice-Atmosphere Processes

The physical processes described in above section create the MIZ roughness, which subsequently modifies the surface energy budget. The fluxes of mass, heat, and momentum, in the presence of a gradient, increase due to higher surface roughness of MIZ.

2.3.1. Wind-Generated Wave Coupling with MIZ

Ocean waves play an important role in ice dynamics in the MIZ because they are the primary energy source that is responsible for the breakup of sea ice and thus determine floe sizes in the MIZ. The wave energy propagates in ice floes in the form of flexural-gravity waves resulting in energy loss due to the wave scattering at edges. Subsequently,

the floe collision occurs that leads to the wave attenuation. Here, I describe fetch-limited and infinite fetch interactions of waves with sea ice floes, followed by effect of fetch on the atmospheric boundary layer, generation of turbulence, and in the end, a few techniques of measurements.

Fetch-Limited MIZ

In a fetch-limited MIZ, when the wind blows across the MIZ composed of small floes, the ice further breaks up into a series of ice forming band-like structure (see Figure 6.10 by Wadhams, 1983). Fetch-limited MIZ interaction with waves, due to high-winds, leads to greater ice floe collisions and deformation (Overeem et al., 2011). Since MIZs contain less than 100% ice concentration, a stable oceanic boundary layer is unlikely to exist. The absence of pressure ridge is compensated by the colliding floe edges that produce higher drag coefficients. Based on the wind interactions Squire and Moore (1980) categorize the MIZ into three distinct regions: ice edge, transition zone, and the interior zone. These three zones individually respond to wind forcing differently. The wave motion impeded by ice floes reduces from ice edge towards the interior zone under fetch-limited wave regime.

Role of Infinite Fetch

Larger fetch essentially means high-energy waves are generated by the wind blowing over longer time periods. In this case, the energetic waves penetrate deeper into the MIZ, which breaks up the ice floes in the interior zone of the MIZ. Infinite fetch wind-generated waves can have large amplitudes and period, which allows them to travel great

distances from open water into the ice fields across the MIZ. Asplin et al. (2012) reported the breaking up of ice due to long-crested waves of 13.5 s.

In the MIZ, limited fetch results in smaller waves, whereby the wave structure on the water surface changes as the distance from the upwind edge of a lead increases. The waves closest to the upwind edge of the lead are capillary waves, changing over to gravity waves as the fetch increases (Alam and Curry, 1997). In the presence of infinite fetch, the sea surface eventually comes into equilibrium with the wind field. It is mainly the longer fetches that play a greater role in deforming the ice field/ocean surface and facilitating ice motion. The limited fetches also produce less significant roughness, as the wind stress is not carried over long distances to impact a larger ocean surface.

2.3.2. The Effect on Atmospheric Boundary Layer

The wind-generated waves eventually lead towards modifying the atmospheric boundary layer. The wind forcing in the MIZ creates variable drag on the MIZ surface. Arya (1973, 1975) provided a method to measure drag over sea ice by dividing the total drag into two types: 1) skin friction drag, and 2) form drag. Skin friction corresponds to wind resistance due to horizontal surfaces such as melt ponds and leads whereas form drag is due to nearly vertical structures such as pressure ridges.

The Structure of Atmospheric Boundary Layer

The atmospheric boundary layer or turbulent layer is the layer of air directly above the Earth's surface in which the effects of the drag, heating and cooling are felt on the time

scales less than a day, and where significant fluxes of momentum, heat, and mass are exchanged between the surface and the atmosphere (Figure 2.6) (Garratt, 1992).

Figure 2.6. Vertical structure of the atmosphere above ocean.

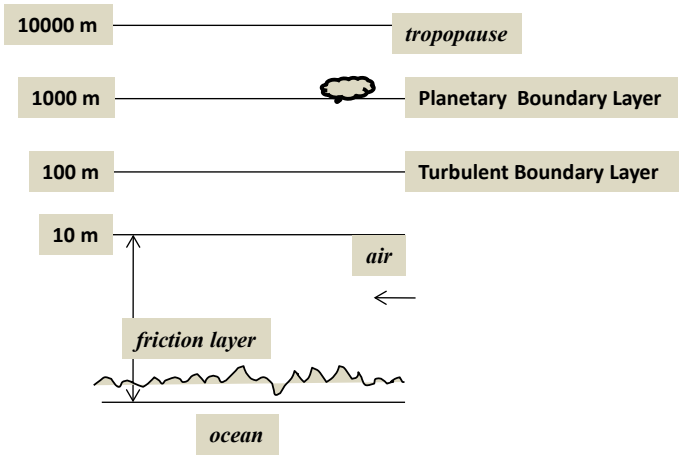

A surface is basically an interface separating two different media. It has no energy, mass of its own, but it is the area of contact of mass and energy exchange between the two media. In the marine cryosphere, the underlying surface changes from water to ice and vice versa seasonally, and overlying surface changes in its physical properties such as density, temperature.

2.4. Remote Sensing of MIZ Roughness

The biggest advantage of remote sensing methods over field measurements in studying OSA processes is the high temporal and spatial coverage provided by the satellites. Microwaves remote sensing is more useful in the Arctic environments as it provides all

weather capability of data acquisition. The microwaves (0.3–300 GHz) are sensed through two means: radiometer (passive) and radar (active). A radiometer senses the radiation emitted by the object, whereas the radar senses the reflection or backscatter of its own radiation impinged onto the object. Remote sensing reflectance based optical methods, radar and laser altimeters, acoustic-sensing methods are also described. The physical basis of microwave remote sensing of sea ice lies in how microwaves interact with the sea surface. The EM waves can reflect from the surface or from the volume of rough ice.

2.4.1. Sea Ice Roughness

To study the roughness of sea ice surface, it is important to understand the EM scattering mechanism from sea ice. The roughness can be estimated by active or passive microwave methods of observation. There are a number of satellites for both active and passive microwave observation of sea ice. The major challenge that still persists is the classification of ice roughness as observed through the remote sensing methods. This is due to the changes occurring in ice surface signatures at much smaller temporal and spatial scales than provided by satellites. Other remote sensing methods, e.g., sonar, LiDAR are also described.

Active Microwave Remote Sensing

Surface scattering can be a dominant scattering mechanism under several circumstances. For example, in the first-year ice, which has very high salinity levels and therefore a high dielectric constant, there is little transmission of EM energy into the ice, resulting in little

to no volume scattering. Additionally, if first-year ice is rough, the scattering is further enhanced mainly due to the surface geometry. Sea ice with lower dielectric constants (for example multiyear ice with fresh surface layer) can also cause surface scattering if dielectric constant fluctuations within multiyear ice are negligible, ice is lossy, and spatial fluctuations occur on scales smaller than the EM wavelength (Carsey, 1992).

While first-year ice primarily scatters EM radiation from the surface due to its high salinity, volume scattering is observed in multiyear ice due to low salinity and the presence of air bubbles in the space once occupied by brine pockets. Therefore, the EM wave easily penetrates deeper into multiyear ice. At higher frequencies the air bubble size becomes comparatively larger than the wavelength, which further increases volume scattering. The surface roughness of multiyear ice contributes significantly to the backscattering for higher frequencies (X, Ku bands).

In the presence of water on the ice surface (first-year or multiyear), EM waves cannot penetrate the ice surface. This usually occurs in the melting season when due to rising surface temperatures dry snow turns into wet snow and melt ponds appear on the surface. Surface scattering dominates in the summer season and if we compare backscattering from multiyear and first-year ice in summer, the backscattering coefficient from multiyear ice is larger due to additional effect of surface roughness exposed due to melted snow (Carsey, 1992). Melting on first-year ice decreases backscattering coefficient whereas it increases on multiyear ice due to exposed surface roughness, which is relatively non-existent, or less compared to multiyear ice. Rough and dry first-year ice shows larger surface scattering than rough and dry multiyear ice at higher frequencies.

Even lower frequency (1.2 GHz) EM waves do not penetrate much in dry and saline first-year ice.

The use of polarimetric synthetic aperture radar (pol-SAR) represents a promising approach for satellite-based monitoring of surface roughness and, concurrently, discriminating sea ice types within a MIZ (Nghiem and Bertoia, 2001). A pol-SAR records the amplitude and phase information of backscattered energy for four transmit-receive polarizations (HH, HV, VH, and VV), thereby facilitating the derivation of the full polarimetric response of the target. It is recognizable that the diversity in polarization achievable by pol-SARs or even by dual-polarization SAR systems provides more complete inference of target features (e.g., sea ice) than conventional, single channel SARs. Furthermore, recently launched pol-SARs are capable of higher spatial resolution (< 10 m) imaging, leading to enhanced potential for monitoring complex ice environments such as the MIZ. Discrimination of ice types using SAR has been conventionally achieved by utilizing different combinations of linearly polarized backscattering coefficients (Kwok et al., 1992; Melling, 1998; Wohl, 1995). Multiyear ice, smooth first-year ice, rough first-year ice (Figure 2.2) and new ice/open water in the Beaufort and Chukchi Seas during March have been identified using a single polarization SAR image intensity-based classification scheme (Wohl, 1995), while others have used single polarization SAR image texture analysis to discriminate new ice, first-year ice, and multiyear ice during the month of March in the Beaufort Sea and the Mould Bay respectively (Barber and LeDrew, 1991; Holmes et al., 1984). Dual co-polarized backscattering coefficient differences in HH and VV have been used to discriminate first-year ice, multiyear ice, and lead areas in the Beaufort Sea during March (Nghiem and

Bertoia, 2001). However, the complexities in polarimetric signatures associated with the dynamic mixture of surface roughness and ice type conditions in a MIZ require utilization of polarimetric radar backscatter, so that the material (dielectric) and geometrical properties of the surface, which influence backscatter, may be individually assessed.

Ship-based observations of co- (linear) and cross-polarized backscatter, circular polarimetric coherences (ρ_{HHVV}, ρ_{HHVH}, and ρ_{RRLL}), as well as co-polarized and cross-polarized polarization ratios (γ_{co} and γ_{cross}), can be used to evaluate their utility for ice surface discrimination from satellite using a polarimetric radar operating in C-band (5.5 GHz). The coherency matrices can be derived as co-polarized Eq. (2.9), cross-polarized Eq. (2.10) and circular (RRLL: right-right left-left rotation of the electric field vector about the line of sight) Eq. (2.11) coherences in magnitude form (Lee et al., 2000; Schuler et al., 2002) as,

$$\rho_{\mathrm{HHVV}} = \frac{\langle |S_{\mathrm{HH}} S_{\mathrm{VV}}^{*}| \rangle}{\sqrt{\langle |S_{\mathrm{HH}}|^2 \rangle \langle |S_{\mathrm{VV}}|^2 \rangle}}, \tag{2.9}$$

$$\rho_{\mathrm{HHVH}} = \frac{\langle |S_{\mathrm{HH}} S_{\mathrm{VH}}^{*}| \rangle}{\sqrt{\langle |S_{\mathrm{HH}}|^2 \rangle \langle |S_{\mathrm{VH}}|^2 \rangle}}, \tag{2.10}$$

$$\rho_{\mathrm{RRLL}} = \frac{\langle |S_{\mathrm{HH}} - S_{\mathrm{VV}}|^2 \rangle - 4\langle |S_{\mathrm{HV}}|^2 \rangle}{\langle |S_{\mathrm{HH}} - S_{\mathrm{VV}}|^2 \rangle + 4\langle |S_{\mathrm{HV}}|^2 \rangle}, \tag{2.11}$$

$$\gamma_{co} = \frac{S_{\mathrm{VV}}}{S_{\mathrm{HH}}}, \tag{2.12}$$

$$\gamma_{cross} = \frac{S_{\mathrm{HV}}}{S_{\mathrm{HH}}}. \tag{2.13}$$

where S is the complex scattering matrix. The elements of S are complex numbers containing magnitude and phases of transformed electric field. An asterisk (*) represents the complex conjugate. The brackets $\langle . \rangle$ represent ensemble averages of the observed data. Polarimetric ratios γ_{co} and γ_{cross} are simply power ratios of backscattered energy. Polarimetric coherences and polarization ratios have utility in reducing the ambiguities caused by the non-linearity between system response and target properties. Regarding Arctic sea ice, some literature is available on the use of ρ_{HHVV}, ρ_{RRLL} and γ_{co} at different EM frequencies. C-band backscatter coefficients (HH, HV, and VV) and ρ_{HHVV} have been used to characterize various first-year ice types (compressed, rubble and ridge, and smooth) and multiyear ice (Rignot and Drinkwater, 1994). Thin sea ice has been effectively discriminated from first-year ice using C-band γ_{co} ratio (Geldsetzer and Yackel, 2009). ρ_{HHVV} and γ_{co} have been used to discriminate Arctic leads using L-band radar signatures (Winebrenner et al., 1995). In a similar study, Wakabayashi et al. (2004) described polarimetric characteristics of different first-year ice types (thin ice, smooth, and rough) using L-band ρ_{RRLL} and γ_{co}, and showed the utility of coherences and ratios in discriminating ice types. Nakamura et al. (2005) discriminated ice surface using γ_{co} ratio in an observational study of lake ice using airborne L- and X-band Synthetic aperture radar (SAR). These studies lack a holistic overview of the utility of different polarimetric coherences and ratios to discriminate thin first-year ice types in a MIZ.

SAR scattering of MIZ is a major and very important tool for improving our knowledge of surface roughness in the MIZ as the microwave signatures of MIZ vary with the changing surface dielectric and physical properties. SAR sensors are extremely sensitive to these changes occurring in the MIZ surface and have been operated on

airborne as well as satellite platforms. Successful SAR missions are: SIR-C, ERS SAR, ENVISAT ASAR, RADARSAT-1 SAR, JERS-1 SAR, ALOS PALSAR (past); RISAT-1, RADARSAT-2, (current); Sentinel-1/3, ALOS-2, RADARSAT Constellation Mission (future).

Passive Microwave Remote Sensing

Passive microwave signatures of MIZ change with time as seawater undergoes transitions during various stages of sea ice formation from early freeze-up through the melting season. The passive microwave signatures depend on the dielectric constant, which is, in turn, dependent on the salinity, temperature, and wetness of sea ice. Ship- or surface-based observations of passive emissions provide point measurements whereas the satellite sensors look at the bulk characteristics of an area, which may contain many different ice types. The EM frequency and the satellite altitude determine the spatial resolution capability of a sensor. Because the altitude of the satellite remains fixed, a large number of frequencies are used to achieve the desired range of spatial resolutions. The contribution of emissions comes from the volume of sea ice/ water covered by the skin depth for a particular EM wave. The difference between H- and V-polarized emissivity of open water is usually large (Ulaby et al., 1986); the V-polarization brightness temperature is usually higher than the H-polarization brightness temperature. The Fresnel reflectivity in the vertically polarized component is always smaller than the reflectivity in the horizontally polarized component according to Fresnel's law. Emissivity of ice surface is one minus the reflectivity. Therefore, for high microwave reflectivity of the ice surface relates to low microwave brightness temperatures.

The passive microwave satellite data can be useful in estimating sea ice concentrations using NASA Team 2, Bootstrap, and OSI-SAF (Ocean and Sea Ice Satellite Application Facility) algorithms. These algorithms are basically good for estimating ice concentrations at regional scale rather than providing details on the surface roughness and associated ice types at smaller scales. Stroeve et al. (2006) have used polarization ratios and gradient ratios for studying the impact of surface roughness on sea ice concentration retrieval using passive microwave data at multiple frequencies. Svendsen et al. (1983) have shown that H-polarization at 89 GHz is sensitive to changes in physical roughness.

The presence of snow (dry or wet) on sea ice can significantly alter the passive microwave emission that reaches the sensor (Barber et al., 1998). Snow itself undergoes metamorphism during different seasons, thus changing the bulk emissivity of the sea ice surface. Lohanick (1990) measured brightness temperature in a profile over multiyear ice to show that the snow cover (dry and wet) could mask the underlying ice features, for example, melt ponds.

The atmospheric effects are considerable for airborne and satellite-based observations of brightness temperature. The attenuation of microwave signal from cloud liquid water is pronounced at higher frequencies. The emissivity and brightness temperature of sea ice and snow changes seasonally with the changes in sea ice type and physical and dielectric nature of the surface (Comiso, 1990; Parkinson et al., 1987). Livingstone et al. (1987) divided sea ice into five stages depending on the seasons: winter, initial warming, melt onset, advanced melt, and freeze-up. The brightness temperatures increase as the free water content of snow increases (Grenfell and Lohanick, 1985). It decreases as the freeze-up season approaches.

Passive microwave emission is affected by ice surface roughness as a complex function of the frequency, polarization, sensor-surface geometry of the radiometer, and complex permittivity of the material bounded below by the rough surface (Kong et al., 1979; Grenfell and Lohanick, 1985; Grenfell, 1992; Barber et al., 1998; Grody, 2008). Brightness temperature has been used to estimate sea ice concentration, ice temperature and snow depth from satellite data (Comiso et al., 2003). Due to greater surface area of rough sea ice, the brightness temperature detected by the satellite sensor increases, and thus the derived sea ice concentration is affected. Stroeve et al. (2006) have discussed the impact of surface roughness on AMSR-E sea ice products, whereas Hong (2010) detected small-scale roughness using AMSR-E observations.

Satellite-based passive microwave sensors provide nearly complete temporal (one day) data coverage (especially for Polar Regions; e.g., sea ice concentration, extent), which SARs and altimeters do not provide. The spatial resolution of passive microwave sensors is, however, approximately limited to 5.4 km (for 89 GHz). This restricts sub-pixel evaluation (higher resolution) of MIZ passive emission signatures using satellite-based passive sensors. Stroeve et al. (2006) studied the impact of sea ice surface roughness on the AMSR-E products. Some of the passive microwave satellite missions are: SSM/I, AMSR-E, SMMR (past); AMSR-2, SSMI/S, SMOS MIRAS (current).

Altimetry

Sea ice surface roughness estimation from laser altimetry is based on the average pulse shape of ground reflections. The pulse shape represents the probability density of the height variations if the pulse length is short compared to the surface height variations.

The rms surface height (roughness) can be estimated from the mean-square width of the received pulse for horizontal, random rough ice surface with Lambertian reflectance.

Satellite-based laser and radar altimeters have shown their immense usefulness in estimating surface elevation, freeboard (the difference between surface elevation and the sea surface height, in other words, the vertical distance between the air-snow interface and the local sea surface), ice edge identification, and thickness of snow and ice layers in ice-covered marine system (Kwok et al., 2007; Kwok and Rothrock, 2009).

Figure 2.7. Illustration of helicopter-based altimetry over a marginal ice zone.

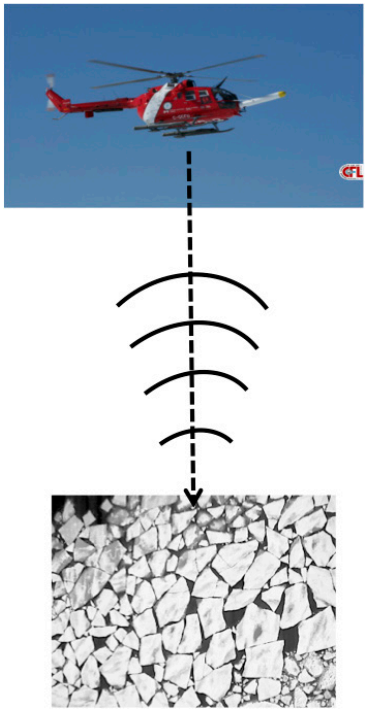

Satellite or airborne altimetry is useful for measuring physical roughness in an MIZ and is one of the ways that can be employed in parameterizing the drag coefficient using remote sensing (Figure 2.7). However, altimeters provide point/profile measurements and do not cover large swaths, which is a requirement in measuring MIZ roughness. The

altimeter data can be re-sampled to match the spatial resolution of other microwave satellite data such as SSM/I. The altimeter's sensitivity for detecting ice edge is greater than that of passive microwave sensors. Some of the satellite altimeters used in Arctic applications are: Seasat, ERS-1/2, ENVISAT Radar Altimeter-2, GLAS (past); Cryosat-2, Saral (current); Sentinel-3, ICESat-2 (future).

Other Techniques

Other remote sensing techniques, e.g., optical remote sensing, sonar, EM induction, SAR interferometry, and photogrammetry can be successfully applied to get information on the surface roughness of sea ice.

Most optical remote sensing detection of ice roughness relies on the spectral reflectance viewed from one incidence angle. Surface roughness affects both the spectral reflectance, and the angular distribution of reflected radiance. However, multi-angular data [e.g., Multi-angle imaging spectroradiometer (MISR)] can also be used for characterizing sea ice roughness (Nolin et al., 2002).

Submarine upward looking sonar data is the most useful means of acquiring roughness data at the bottom of sea ice and thereby, through proxy, the surface roughness of large regions of sea ice (Wadhams, 1988). Ice thickness or keel depth is determined from the return travel time of an acoustic pulse (420 kHz) reflected off the underside of the sea ice (Fissel et al., 2008).

EM induction, operated from above the sea ice (surface or airborne), takes the advantage of the fact that sea ice has a very low electrical conductivity, while seawater is a very good conductor (Haas et al., 2009). A low frequency, primary EM field generated

by the transmitting coil of an EM system penetrates the sea ice almost unaffected, while it generates eddy currents in the seawater below the sea ice underside. These eddy currents induce a secondary EM field, which propagates upwards through the sea ice and whose strength is measured with the receiving coil of the EM system. The strength of the secondary EM field is directly related to the distance between the coil and the conductive seawater surface, which coincides with the ice underside. With known height of the EM system, ice thickness is computed from the difference between the EM system height and electromagnetically determined height above water-ice interface. It, thus also provides the bottom roughness in addition to the surface roughness derived from laser altimeter mounted on the same platform (Prinsenberg et al., 2006).

SAR interferometry (InSAR) offers new possibilities for research in sea ice roughness scattering and sea ice mechanics. Interferometric coherence is mainly dependent on the temporal characteristics of the scattering from sea ice. Interferometric phase is dependent on the deformations of ice (Dammert et al., 1998). *Fast ice* (sea ice which forms and remains attached to the coast) compared to mobile sea ice experiences small slips and deformations. Interferometric phase measurements are very sensitive to these deformations, slips, and displacement. InSAR technique is helpful in providing insights into the rheology and motion of fast ice. The coherence over sea ice changes very fast; which restricts InSAR to be used over fast changing sea ice (Dammert et al., 1998).

Sea ice features can be accurately measured using photogrammetric theory (Hall and Rothrock, 1987). Oblique pictures taken from the ship can provide floe size and surface roughness. However, geometric distortion occurs when a camera lens is in an oblique orientation (Lu and Li, 2010). The ship-borne photography has advantages due to easy

operation, and automated data acquisition. The techniques described in this particular section are not the focus of my Ph.D. research.

2.4.2. Open Water Roughness

Satellite sensors provide a wealth of information on open water. It allows the estimation of winds and waves, two of the main factors of surface roughness, taking the advantage of the motion of ocean surface waters. Active and passive microwave methods and radar altimetry are useful in wave and wind detection compared to optical remote sensing methods. Other remote sensing methods, e.g., acoustic sensing and LiDAR are also described.

Active Microwave Remote Sensing

As described earlier, wind and waves are the major causes of creating surface roughness in the open ocean; the measurements of satellite-based, vertically polarized radar backscatter from the ocean surface translate via empirical expressions into wind speed, wave height, and direction. This relationship exists because the wind roughens the water surface via the production of gravity-capillary waves, which, in turn, effectively backscatter radar signals via Bragg scattering for different grazing angles (Plant, 1990) (Figure 2.8). Capillary and gravity waves serve as roughness elements on the ocean surface to scatter EM waves. Applications of radar instruments for ocean remote sensing brought the demand for wave number spectrum models in the short gravity and capillary-gravity range, dynamically coupled with the atmosphere.

The backscatter observations of open water represent composite signals that contain contributions from the full suite of ocean surface variables. The total backscatter (σ_0) from the ocean surface is the sum of Bragg scattering, specular reflection and non-Bragg scattering components (Eq. 2.14):

$$\sigma_0^p(Total\ NRCS) = \ \sigma_0^p(Bragg) + \sigma_0(specular) + \sigma_0^p(non\text{-}Bragg). \quad (2.14)$$

Valenzuela (1978) provided a review of the theories addressing EM wave interaction with ocean waves, citing Bragg (resonant) scattering as the most important mechanism of ocean surface-EM interaction. Bragg scattering occurs when incident EM energy is coherently backscattered from periodic waves matching the Bragg limit $2k \sin\theta$, k being the radar wave number and θ, the angle of incidence (Figure 2.8). Non-Bragg scattering also plays an important role as long surface waves, which are much larger than conventional radar wavelengths and beyond the Bragg limit, modify the backscatter by changing the slope of Bragg waves relative to the radar–a process known as *tilt modulation*. Energy dissipation over different length scales and breaking wave mechanisms are largely linked to non-Bragg scattering, though their effects on backscatter are less understood.

Figure 2.8. An illustration of the law of Bragg (resonant) scattering.

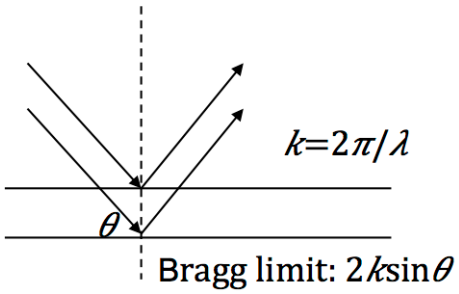

Active C-band wavelength represents an optimization between surface wave height and radar wavelength, and is more reliable than shorter wavelengths Ka- and X-band that are strongly influenced by capillarity and molecular viscosity (water temperature) (Phillips, 1988). There are numerous studies readily found on the relationship between C-band co-polarization backscatter (HH and VV) and wind speed and direction, with geophysical model transfer functions (CMOD) widely used to retrieve wind information from backscatter coefficients (Stoffelen and Anderson, 1997; Hersbach et al., 2007). A power law relationship holds for backscatter and friction velocity (Jones and Schroeder, 1978). A power relationship exists between C-band backscatter and wind speed (Keller et al., 1989). They also observed normalized radar cross-sections (NRCS) decreasing with ocean-atmosphere temperature difference with increasing temperature difference and wind speed. Thompson et al. (1998) found that the observed co-polarization ratio is larger than predicted by backscatter models that rarely address non-linearity of the long-wave portion of a rough ocean surface. They provided an expression for polarization ratio as a function of incidence angle that was modified by Mouche et al. (2005) who related it to the wind speed, wind direction, sea state, and swell. The results of Mouche et al. (2005) show that the co-polarization ratio (γ_{co}) (Eq. 2.12) is dependent more on wave steepness

than on wave height and wind speed. However, the transfer of wind energy in modifying various components of the ocean surface is less understood. Though, it is widely observed that wind speed increases backscatter, the backscatter signal received at the sensor originates from different sources/elements (described earlier) initially induced by wind energy. At C-band, the waves, which induce tilt modulation in rough seas, are typically three to ten times larger than the incident radar wavelength (Kudryavtsev et al., 2003a, b). Kudryavtsev et al. (2003a) suggested a composite backscatter model for describing backscatter (at moderate incidence angles 20°–60°) from ocean surface waves, which included non-Bragg scattering components caused by breaking waves (wavelength from few millimeters to few meters) based on wave breaking statistics proposed by Phillips (1985). The γ_{co} can be used to study the discrepancy between the Bragg model and observations and it can explain non-Bragg component of scattering (Kudryavtsev et al., 2003a). The hydrodynamic modulation transfer function at HH is stronger than that at VV for non-Bragg scattering for incidence angles 40°–60° under different wind conditions (Kudryavtsev et al., 2003b).

C-band radar backscatter varies with air-sea temperature difference such that the radar backscatter is significantly higher when temperature difference is less than zero than when it is greater than zero (Keller et al., 1985). Bragg scattering is the significant source of scatter for C-band satellites, e.g., ERS and RADARSAT. These systems image the spatial variability of gravity-capillary waves with wavelengths of the order of 5 cm.

Gerling (1986) identified linear patterns in radar backscatter measured by Seasat, hypothesizing that they were created by atmospheric vortices. He also suggested that such patterns might be useful for inferring both wind direction and boundary-layer height.

However, recent studies have shown that inferring boundary-layer depth using only the spacing of SAR streaks is a more complex task than had been hoped (see Fig. 3 by Gerling, 1986).

Wind, as we saw in earlier section, is the main driving force for most of roughness created on the ocean surface. Microwave scatterometers are instruments that transmit low-power pulses of radiation toward the ocean at intermediate incidence angles and measure the intensity of the signals scattered back at the same angles from surface areas a few kilometers on a side. Microwaves at Ku- (14 GHz) and C-band (5.5 GHz) penetrate only a few millimeters into seawater, so all backscatter originates at the surface and is caused by the roughness of the surface; a perfectly calm sea surface produces no detectable scattering in the direction of the incident radiation. Changes in the average roughness of the ocean surface over scales of several kilometers are caused primarily by changes in the wind speed or direction at the ocean surface. Standard assumptions of scatterometry are that the backscatter cross-section over such scales depends only on parameters of the scatterometer and on the mean wind, increases with wind speed, is a maximum when the antenna looks upwind, and is a minimum when the antenna looks nearly perpendicular to the wind, or crosswind. These assumptions allow the wind speed and direction to be determined from cross-sections measure for the same patch of the ocean, but with the antenna directed at several different azimuth angles.

Other instruments such as radar altimeters that look straight down and real and synthetic aperture radars that image surface are capable of measuring wind speed or direction but not both simultaneously and routinely. However, only microwave scatterometers are the most successful. The relationship between backscatter (σ_0),

incidence angle (θ), polarization (p), wind speed (U) and wind direction (χ) is called *geophysical model function* and has the following form (Stoffelen and Anderson, 1997; Hersbach, 2010) as given by Eq. (2.15):

$$\sigma_0 = A_0(U, \theta, p)[1 + A_1(U, \theta, p)cos\,\chi + A_2(U, \theta, p)cos\,2\chi]^k. \quad (2.15)$$

where A's are coefficients, k is a parameter.

Among the various microwave techniques developed for measuring ocean surface waves from satellites, imaging radars are considered to contain the greatest amount of information. They have the potential of measuring wavelength, wave direction, and wave height of the ocean waves (Alpers et al., 1981, Wang et al., 2012). The detectability of ocean waves by radar becomes possible by the modulation of the radar cross-section by the long ocean waves. The cross-section modulation by the long ocean waves is attributed to: (1) the *tilt modulation*- the change in the local incidence angle of the facet through the long wave slope, (2) *hydrodynamic modulation*, which modulates the energy and wave number of the short Bragg scattering waves, and (3) *velocity bunching* - by definition (Alpers, 1981) produces wavelike patterns on the image even if no modulation of the microwave backscattering cross-section by long wave were present (Hasselmann and Hasselmann, 1991). The tilt modulation is due to the purely geometric effect that Bragg scattering waves are seen by the radar at different local incidence angles depending on their location on the long waves. The modulation is larger for HH polarization than for VV polarization. The hydrodynamic contribution of the cross-section modulation is characterized by a non-uniform distribution of the short waves with respect to the long

ocean wave field, which is attributed to interactions between short and long waves. The simple hydrodynamic interaction theory can only be valid for a relatively smooth sea, where nonlinear effects, which lead to a steepening of waves and eventually to wave breaking, are unimportant. This theory is not applicable for very large wave heights (turbulent sea). The simple hydrodynamic interaction theory is better applicable for the modulation of surface wave with wavelengths in the decimeter range than in the centimeter range. This is because the distribution of the shorter ripple waves is more strongly affected by the wind than the distribution of the longer ripple waves. The physical process, which renders long ocean waves detectable by SAR images, is to a large extent cross-section modulation.

Passive Microwave Remote Sensing

Ocean surface roughness modifies ocean-atmosphere interaction and concurrently affects observed passive microwave brightness temperatures. Passive microwave brightness temperatures are observed to increase with increasing surface roughness (foam, whitecaps, and bubbles) due to increase in surface area exposed to the sensor. Polarimetric passive microwave signatures of the ocean surface at various frequencies are well-modeled by a two-scale polarimetric emission model (Germain et al., 2002; Yeuh, 1997), however, the assimilation of effects of wind direction, wind-generated waves, atmospheric stability, and sea foam into polarimetric emission models of ocean surface are not considered in literature and are topics of further research. Observed, frequency-dependent, brightness temperature is significantly affected by the undulations of the ocean surface and is dependent on the wind-induced wave structure, i.e. the sea state or

surface roughness, and foam coverage (Hollinger, 1971; Ulaby et al., 1986). Kravtsov and Churyumov (2000) mathematically described the effect of steep irregularities and wave slope on the brightness temperature. Inclusion of additional parameters of whitecaps and foam was suggested in the retrieval algorithms using satellite remote sensing (Monahan and O'Muircheartaigh, 1986). Wave height/surface roughness can also be linked to brightness temperature as a close function of surface wind speed (Strong, 1971). Nordberg et al. (1971) provided the measurements of microwave emission at 1.55 cm (19 GHz) wavelength from a foam-covered and wind-driven sea. In all above-mentioned different surface conditions, the brightness temperature is observed to be increasing with an increase in foam coverage and whitecaps.

Altimetry

Laser and radar altimeters on satellites provided a wide range of ocean surface data. Short-pulse radar altimeters aboard low-orbiting satellites have the capability of measuring the mean height of the ocean surface, the roughness of this surface, and the wave height. The mean height measurement uses the round trip travel time of radar pulses to estimate the distance from the satellite to the surface. The roughness of the ocean surface causes stretching of the return pulse; which is a direct measure of the ocean wave height. Contributions to the received radar signal occur when the scattered energy from specular points on the rough ocean surface is returned to the radar antenna (Rufenach and Alpers, 1978). These points are received at different delays since they come from different depths in to the rough surface. The delayed signals add randomly causing stretching of the leading edge of the return pulse. The received pulse increases in

amplitude after being reflected from the surface up to a peak value. The time evolution of the backscattered signal as recorded by the receiver is given by the convolution of the incoming pulse $I_0(t)$ with the impulse response function $H(t)$ (Eq. 2.16).

$$I(t) = \ H(t) * I_0(t) = \int_{-\infty}^{+\infty} H(t-t')I_0(t')dt'. \tag{2.16}$$

$$H(t) = \ S(t) * R(t)$$

where $H(t)$ is the convolution of the radar sea surface impulse response function $S(t)$, which describes the backscattering of the pulse and the receiver response function $R(t)$. For a simplified case, a nearly smooth flat sea surface, the mean backscattered signal is proportional to the area illuminated by the pulse. If the sea surface is rough, however, specular points are encountered above and below mean sea level. For a rough sea, the surface response function $S(t)$ is the convolution of a step function and the probability density function for specular points having heights above the mean level. Specular points for a nadir-looking altimeter are characterized by tangent planes on the ocean waves where the normal of these planes are vertical to the mean sea surface. In the analysis of a rough surface, it can be assumed that the ocean wave field obeys Gaussian statistics.

Other Techniques

Among other techniques, optical (LiDAR) remote sensing, optical (passive) remote sensing, and acoustic sensing can be useful for surface roughness detection.

Surface roughness detection using LiDAR remote sensing methods heavily depends on the atmospheric perturbation because the laser beam is absorbed and scattered by the atmosphere. The transmitted laser beam is perturbed by the turbulence in the atmosphere as it propagates to the target. At the ocean surface, the laser radiation is scattered in a diffuse manner. Because the surface is rough, the optical path length (distance traveled in a system by light) between each scattering point and the receiver is random and manifests itself as a phase change in the optical wave at the receiver. As the beam is scanned over the surface, the phase changes randomly; as the surface becomes rougher, the amount of phase fluctuation increases and causes the phase variance to increase (Holmes et al., 1994). This implies that there exists a relationship between the optical phase variance and the surface height variance. This is the basis on which optical remote sensing of surface roughness is investigated.

Surface roughness can be estimated using the ratio between surface-reflected solar radiance measured form two view angles at nearly the same time. The ratio is primarily a function of the difference between shading observed from the two view angles and under the same illumination as proxy for relative surface roughness (Mushkin and Gillespie, 2005). However, this technique is less useful due to the moving targets (waves) at the ocean surface. Sun's glitter pattern (obtained from optical photographs) on the sea surface can be used to derive the distribution of wave slope at various wind speeds (Cox and Munk, 1954). This distribution can provide important information about the reflection and refraction of acoustic and/or EM radiation, and about the complex problem of wind stress on the water surface. Shifrin (2001) provided the reflection statistics from

a rough sea surface using MODIS (Moderate Resolution Imaging Spectroradiometer) data.

Underwater acoustic wave gauge can be used to measure statistical characteristics of sea surface roughness (Karaev et al., 2011). Backscattering of acoustic waves from the sea surface provides similar statistical information as that using EM waves. However, the acoustic remote sensing method is restricted to point measurements through airborne, submarine, and ship-based surveys.

2.5. Conclusions

Surface (physical) roughness of the MIZ is not only complex to understand but also equally difficult to measure, estimate, and parameterize using surface-based and remote sensing techniques. While frequent field visits and synoptic data collection are unable to provide a comprehensive dataset in MIZ, satellite data open the pathway to acquiring such dataset. However, satellite remote sensing techniques still have scope for improvements to parameterize and estimate surface roughness in the MIZ. This thesis provides state-of-the-art work using *in situ*, airborne, and satellite data for understanding surface roughness of the MIZ in terms of discrimination of ice types and roughness, utility of advanced microwave polarimetry, validation of geophysical variables from open water, and a seasonal evaluation of ice roughness at sub-pixel level.

Chapter 3

Detection and Classification of Surface Roughness in an Arctic Marginal Sea Ice Zone

M. Gupta[1*], D. G. Barber[1], R. K. Scharien[1, 4], and D. Isleifson[2, 3]

Hydrological Processes, 28(3), 599–609, 30 January 2014, doi:10.1002/hyp.9593

[1]Centre for Earth Observation Science, Department of Environment and Geography, Clayton H. Riddell Faculty of Environment, Earth and Resources, University of Manitoba, 463, Wallace Building, Winnipeg R3T 2N2, Manitoba, Canada

[2]The Department of Electrical and Computer Engineering, University of Manitoba, Winnipeg R3T 2N2, Manitoba, Canada

[3]Now at: Magellan Aerospace, Winnipeg R3H 0S5, Canada

[4]Now at: Department of Geography, University of Victoria, Victoria V8W 2Y2, British Columbia, Canada

[*]Corresponding Author

Abstract

Sea ice dynamic and thermodynamic processes are important and highly variable elements of the marginal ice zone (MIZ). This study examines the detection and classification of statistically separable sea ice classes in the MIZ through a range of temporal and spatial scales. A helicopter-based laser system was used to obtain large-scale and a ship-based laser profiler to identify small-scale roughness types respectively. The analysis of variance (ANOVA) of surface height data from helicopter- and ship-based laser systems, active microwave (AMW) C-band backscattering data and passive microwave (PMW) (37 and 89 GHz) brightness temperature data reveal different classes that statistically differ from one another. We found significant statistical difference in variances in AMW data with six classes that differ in VV polarization, three classes in VH polarization and five classes in HH polarization in the MIZ (e.g., snow-covered first-year ice, ice rubble, pancake ice, frost flowers, melt pond, flooded ice, and ice edge) of southern Beaufort Sea. The PMW emission was not as effective at discrimination, yielding only one statistically separable class. The results can potentially be extended to satellite-based investigations of the MIZ at regional scales.

3.1. Introduction

The marginal ice zone (MIZ) is any portion of the polar sea ice cover sufficiently near to the ice-free ocean such that interactions with the open sea result in the modification of the properties of the ice so that they are different from properties deeper within the pack (Weeks, 2010). The MIZs go through significant physical forcing both spatially and temporally, resulting in varying surface roughness. In turn, this roughness plays an important role in how the MIZ affects prevalent physical and biological processes.

Significant physical processes in MIZ include momentum exchange across the air-ice boundary (MIZEX'84: Campbell et al., 1987; Claussen, 1991; Perrie and Hu, 1996; Birnbaum and Lupkes, 2002; Ivanov et al., 2003; Fer and Sundfjord, 2007), wave dynamics in the MIZ (Wadhams et al., 1988; Squire et al., 1995), heat (Perovich et al., 1989) and salt fluxes (McPhee et al., 2008), turbulence over MIZ (Drue and Heinemann, 2002), and floe size dynamics (Lu et al., 2008). These processes have various feedbacks, each of which being directly or indirectly linked with the roughness of the MIZ. Deformation of ice at large- or small-scale in the MIZ can create potential habitats for organisms inhabiting the ocean-ice (e.g., Arctic Cod, Fortier et al., 2006) and ice-atmosphere (e.g., Polar Bears; Stirling et al., 2004) interfaces. We provide an account of large- and small-scale (physical) roughness in the following paragraphs.

We formally define sea ice roughness as the vertical displacement of ice around a mean ice level at both the ice-atmosphere (termed the sail) and the ocean-ice (termed the keel) following Steiner et al. (1999). To investigate sea ice roughness at large-scale, airborne or spaceborne methods are preferable to eye-based techniques as these are manual and difficult to automate the ice classification at regional scales. Laser techniques

include both profiling lasers, Light Detection and Ranging (LiDAR) and traditional transit survey techniques. Laser-based airborne observations of large-scale sea ice surface roughness were done as early as the 1970s (Ketchum, 1971; Hibler, 1972, 1975). Helicopter-based laser altimeters have also been successfully used for determination of large-scale surface roughness (Prinsenberg et al., 2006; Haas et al., 2009; Goebell, 2011). LiDAR profiles have also been useful in estimating spectral behaviour of sea ice surface roughness (Rivas et al., 2006).

Active microwave (AMW) scattering data is very useful to infer sea ice surface roughness under time-varying surface properties. The evolution of scattering signatures from FYI and multiyear ice (both seasonally rough and smooth classes of each) for varying frequencies, particularly C-band (e.g., Ulaby et al., 1986; Grenfell et al., 1998; Perovich et al., 1998; Geldsetzer and Yackel, 2009; Kim et al., 2012) and Ku-band (Tonboe and Toudal, 2005), and polarizations is still a topic of ongoing research. Polarimetry is a more recent research tool and much less is known as to how this type of energy interacts with sea ice surface roughness. Polarimetry (use of multiple polarization combinations and ratios) is capable of separating the surface roughness component of the scattering signature from the total observed scattering (Cloude and Papathanassiou, 1999; Hajnesk et al., 2003; Wakabayashi et al., 2004; Nakamura et al., 2005; Arai, 2011) and thus shows promise as a tool in estimating the roughness of elements of the MIZ.

Passive microwave (PMW) emission is affected by ice surface roughness as a complex function of the frequency, polarization, sensor-surface geometry of the radiometer, and complex permittivity of the material bounded below by the rough surface (Kong et al., 1979; Grenfell and Lohanick, 1985; Grenfell, 1992; Barber et al., 1998; Grody, 2008).

Brightness temperature (T_b) has been used to estimate sea ice concentration, ice temperature and snow depth from satellite data (Comiso et al., 2003). Due to sea ice roughness, the T_b detected by the satellite sensor changes, and thus the derived sea ice concentration is affected. While Stroeve et al. (2006) discussed the impact of surface roughness on AMSR-E sea ice products, Hong (2010) detected small-scale roughness using AMSR-E observations.

In this paper, we investigate helicopter- and ship-based laser systems, AMW scatterometer and PMW radiometer, as tools to retrieve, understand and classify the surface roughness of various elements of the MIZ. This is a necessary precursor to understanding how AMW scattering data from satellite-based synthetic aperture radar (SAR), and PMW satellite data, may be used to understand the spatial and temporal dynamics of sea ice surface roughness in the MIZ. More specifically, we intend to develop an understanding of surface roughness of the MIZ mainly at small-scales by:

1. Providing an overview of the southern Beaufort Sea MIZ to set the context for a detailed examination of the surface roughness of this MIZ (Section 3.2)
2. Examining the statistical discrimination of surface roughness elements of the MIZ and classifying roughness based on physical properties defined using ship-based and aerial survey data (Section 3.5)
3. Describing the AMW and PMW characteristics of roughness classes created in point 2 (above) using ground- and ship-based data (Section 3.5)

3.2. Study Area

Our study area was located in the southern Beaufort Sea and the Amundsen Gulf in the western Canadian High Arctic (Figure 3.1). A seasonal polynya known as the Cape Bathurst Polynya forms in the area and hosts a number of flaw leads during the winter (Barber and Hanesiak, 2004; Galley et al., 2008). In the present study, only the MIZ associated with first-year ice (FYI) in the southern margin of the polynya is considered. The data were acquired under the auspices of the Circumpolar Flaw Lead (CFL) System Study (Barber et al., 2010) during the International Polar Year (IPY) 2007-08 on the Canadian research icebreaker *Amundsen* over the period October 2007–August 2008. A detailed list of total collected data is provided in Table 3.1. The chosen samples for this study were selected as to cover larger surface variability and roughness types.

3.3. Methods

3.3.1. Helicopter- and Ship-Based Data

To acquire surface roughness data, a moving ship-based laser profiler was used. The laser was mounted pointing vertically downwards (approximately 7 m above the mean sea level) on the end of a beam, and was positioned approximately 3 m from the railing of the port side of the foredeck on the *Amundsen*. The laser wavelength is 905 ± 5 nm with a pulse width of 20.5 ± 5% ns and beam divergence 3.3 mrad ± 5% (1 mrad: 10 cm beamwidth per 100 m distance). The *RIEGL* (Horn, Austria) laser rangefinder model used is LD3100VHS-GF having average power of 640.0 ± 5% μW from a 50 mm wide

aperture. The 90 data points are recorded at every 1.34 s. With a ship speed of 1.03 m/s (2 knots) the spatial resolution was 1.5 cm.

Figure 3.1. Study area map showing ship-based laser observation sites, scatterometer and radiometer (EM) data collection sites, and helicopter flight locations. Dates and total number of acquired data points are given in Table 3.1.

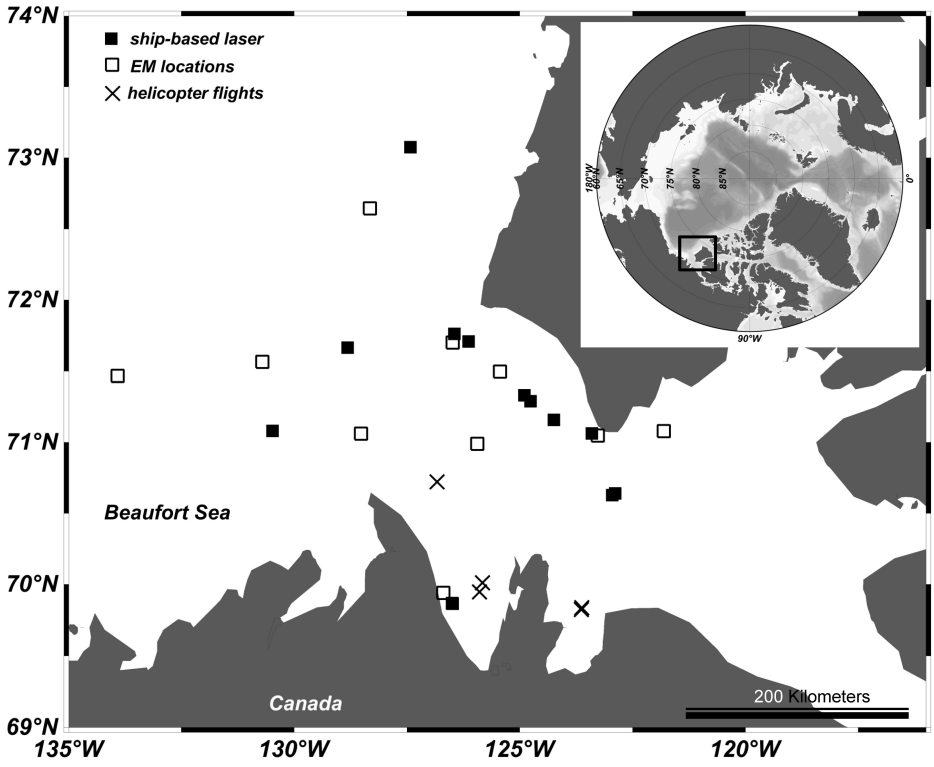

Sea ice surface roughness were measured with a helicopter-based laser system, ADM 3-Alpha Geophysical unit, built by Optech Inc. of Toronto, ON, Canada with a listed accuracy of 1.5 cm. It is a 905 nm infrared rangefinder laser with beam divergence 5 mrad (0.28°). The sampling rate of the ice thickness and roughness data is 10 Hz corresponding to a spatial sampling interval of about 4-5 m for the normal helicopter speed of 46.30 m/s (90 knots) from 130 m altitude. Trimble® (www.trimble.com) GPS

data were acquired every 45 m (at helicopter speed of 90 knots) along the flight line with laser data.

Table 3.1. Table of data summary and instrument specifications. Detailed geographic map of data collection sites is provided in Figure 3.1.

		Field-of-view (FOV) (m)	Footprint (m^2)	Dates	Number of sites
Ship-based laser		0.02	nadir: 1.55	1–5, 15, 16, 18–21, 25 November 2007	12
Helicopter-based laser		0.65	nadir: 1054.37	16–19, 22, 23 April 2008 2, 3, 5, 6, 11, 13–15, 17, 21, 23–25, 28, 31 May 2008 2–4, 7–9, 11, 13, 16, 17, 21 June 2008	34
Scatterometer (AMW)		20°: 0.81 60°: 2.87	at 55°: 2.13	15, 19–21, 25 November 2007 8, 13 June 2008 1, 4, 8–11, 13, 26, 28 July 2008	16
Radiometer (PMW)	37 GHz	30°: 1.68 80°: 45.76	at 55°: 6.62	1, 15, 19–21, 25 November 2007 17, 18 June 2008	8
	89 GHz	30°: 1.65 80°: 44.67	at 55°: 6.36		

3.3.2. Active Microwave Scattering Data

A C-band (central frequency 5.5 GHz) fully polarimetric scatterometer system, developed by ProSensing Inc. (Amherst, MA, USA) was used to collect data on backscattering signatures from various sea ice roughness regimes. The transmitted signal is a linear frequency modulated pulse (chirp). It acquired data in terms of the combinations of linear polarizations, i.e. HH, VH, HV, and VV. These data were acquired over a 20°–60° incidence angle range (5° increments) and a 60° scan width in azimuth. Except for 13

June 2008, when the scatterometer system was installed on the ice to collect data over melt ponds and adjacent snowpack, all other backscattering data were collected during November 2007 and June-July 2008 (Table 3.1) using a ship-based mount 7.56 m above the mean sea level on the port side of the *Amundsen*. The scatterometer had a footprint of 1.1 m^2 in the range direction at 45° incidence angle when operating from onboard the ship (Isleifson et al., 2010), with the footprint increasing in size with incidence angle (Geldsetzer et al., 2007).

3.3.3. Passive Microwave Emission Data

Dual-polarized (H and V) PMW radiometers (Radiometrics®, Boulder, CO, USA) operating at 37 and 89 GHz frequencies were used to acquire emissions of the MIZ surface. The system was installed on the rail mount on the port side of the ship ~12 m above the mean sea level. Voltages were recorded and converted to T_b by the sensor temperature method (Farmer et al., 1990) at incidence angles 30°–125° at 5° increments. A minimum of 2–5 scans was collected for each surface type. Apart from the surface scans, the T_b data were also acquired during the ship transit at a fixed incidence angle of 53°.

3.3.4. Analysis of Variance (ANOVA)

Due to complexity and diversity of electromagnetic (EM) responses and surface roughness of MIZs, sophisticated statistical techniques are required to extract information from the data. The sources of variation in the data can be studied through analyzing

variance in combination with various suitable statistical tests. Our data does not show any particular probability density distribution; therefore, we use non-parametric methods (e.g., Kolmogorov-Smirnov test) to analyze the distributions in the data. Classification of statistically separable surface roughness were attempted from laser surface height data, backscattering data, and T_b data using one-way ANOVA tests performed separately on the laser surface heights, AMW backscattering coefficients and PMW T_bs, respectively. Assumptions of ANOVA were tested first, i.e. normality using the Kolmogorov-Smirnov test, homogeneity of variances (homoscedasticity) using Bartlett's or Levene's test, and serial correlation (independence). Based on this analysis, a follow-up test, Tukey-Kramer method (hereinafter referred to as Tukey's method), for homogeneous subset extraction was used to separate different groups. The assumptions for Tukey's method (i.e., homoscedasticity and independence of datasets) were tested first. Where these conditions are not met, non-parametric test Kruskal-Wallis or Wilcoxon Signed tests (Z-statistic) were performed to check the equality of medians (Brase and Brase, 2009). Comparison circles have been used to show the differences in the groups graphically.

3.4. Results

3.4.1. Laser Data

In Figure 3.2(a), the surface roughness (height) measured by the airborne laser altimeter is plotted with distance over a 7 km (0.06° on map) straight-line flight around 69° 54' N, 123° 24' W. Corresponding histograms for each ice types are shown in Figure 3.2(b). Helicopter-based laser data belonged to several visually identifiable roughness types (a

few are given here), e.g., close ice (floating ice with 7-8 tenths ice concentration) (7 June 2008), melt pond (9 June), flooded ice (13 June), ice rubble (16 June), ice edge (17 June) and ice intruded with seawater (21 June); an ice ridges (April-May) (see Table 3.2 for details). Similarly, the ship-based laser data belonged to the following five of the visually identifiable sea ice roughness types: snow-covered FYI, ice rubble, pancake ice, snow-covered frost flowers, and dense frost flowers. During 1–25 November 2007 (the onset of winter), a large number of small-scale ice roughness types were sampled. The statistical analysis of ship-based laser profiler yields only one statistically separable roughness class, despite five visually identified roughness classes. We find that the statistical analyses of helicopter-based laser data did not yield different roughness types, whereas, we have visually identified several roughness classes.

Figure 3.2. (a) Some of the surface height profiles of helicopter-based laser data on different dates in June 2008. Quantitative information of this data is provided in the Discussion section, (b) Histograms of ice types shown in Figure 3.2(a).

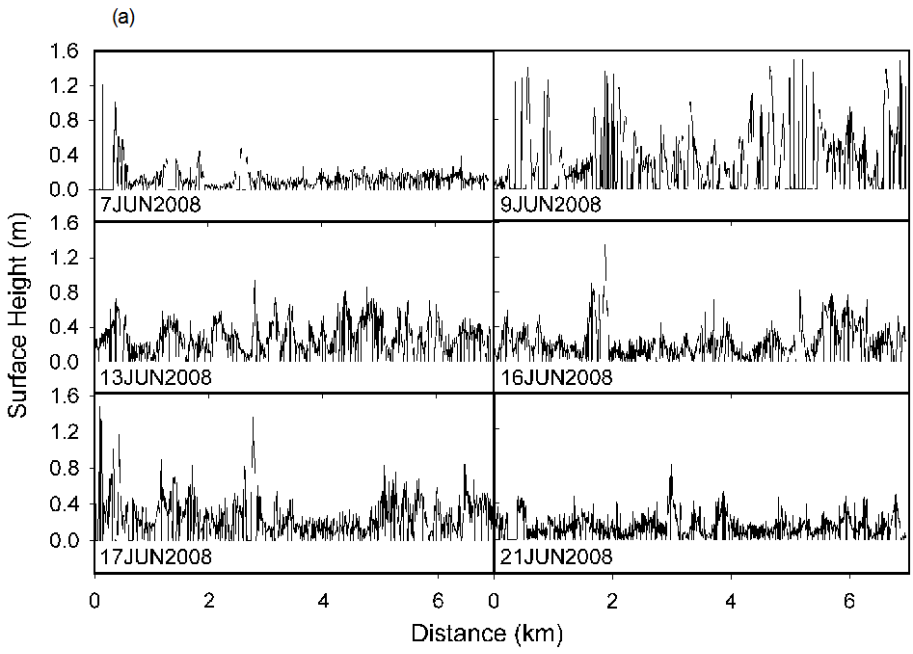

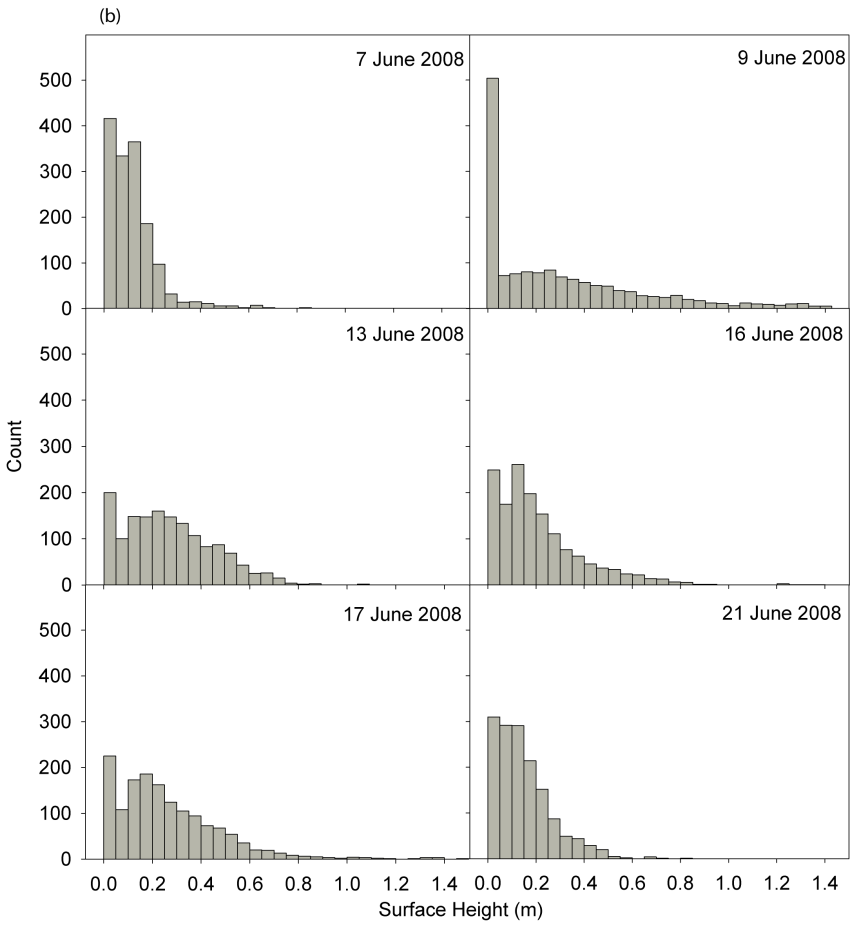

3.4.2. Backscattering Coefficients

Although, manual observation of sea ice types is not enough for discriminating ice types and surface roughness, we found a few distinct sea ice types from ship-based data (Figure 3.3(a)). Corresponding histograms of each ice type are provided in Figure 3.3(b). The fall in each plot of HH, VH, and VV with incidence angle is due to an expected decrease in the amount of returned energy to the radar sensor with increasing incidence angle. The backscattering intensity in VV polarization is mostly higher than the rest. Table 3.2 shows the ANOVA for HH, VH, and VV polarization and Fig 4(*a*) shows the groups displayed as alphabets and plotted as comparison circles, are derived from the ANOVA

using AMW backscattering coefficient (HH, VH, and VV polarization) using Tukey's method. It is clear that the microwave backscattering signal is mixed for intermediate incidence angles. Six different sea ice characteristic groups are formed from VV backscattering coefficient (six: *A* through *F*), three groups from VH (three: *A* through *C*) and five groups from HH backscattering coefficient (five: *A* through *E*) are statistically distinguishable.

3.4.3. Brightness Temperature

The T_b data were also acquired over a variety of ice surfaces, e.g., snow-covered FYI, rubble ice, pancake ice, snow-covered and dense frost flowers. The plots of the T_b versus incidence angle show similar patterns (Figure 3.5). The horizontal polarization is (as expected) colder than the vertical polarization in both frequencies for all sea ice types. However, we do not find any homogeneous groups (only one Tukey group: *A*) in the T_b at any of the used frequency/polarization. Figure 3.4(*b*) shows groups, displayed as alphabets and plotted as comparison circles.

Table 3.2. One-way ANOVA of backscattering coefficients. DF: degrees of freedom, SS: sum of squares, MS: mean squares, Inc: incidence angle, F: *F*-statistic, P: *P*-value, S: pooled standard deviation, R^2 (adj): adjusted R^2.

Source	DF	SS	MS	F	P	
Inc	8	3823.3	477.9	31.68	0.000	VV
Error	193	2911.5	15.1			
Total	201	6734.9				
S = 3.884	R^2= 56.77%	R^2 (adj) = 54.98%				
Inc	8	960.0	120.0	7.46	0.000	VH
Error	193	3102.4	16.1			
Total	201	4062.4				
S = 4.009	R^2= 23.63%	R^2 (adj) = 20.47%				
Inc	8	4700.1	587.5	37.47	0.000	HH
Error	193	3025.8	15.7			
Total	201	7725.9				
S = 3.959	R^2= 60.84%	R^2 (adj) = 59.21%				

3.5. Discussion

3.5.1. Statistical Analyses of Laser Data

Analytical/statistical approach (such as using laser altimeter) is preferable to eye-based technique to classify ice roughness, as it can be potentially used from spaceborne platform facilitating regional/larger spatial coverage (Rivas et al., 2006).

Figure 3.3. (a) Shown are the backscattering coefficients of some of the observed sea ice types. The observed sea ice types are snow-covered FYI (15 November), rubble ice (19 November), pancake ice (20 November), snow-covered frost flowers (21 November) and dense frost flowers (25 November). From the plots, the role of surface roughness is indistinct; however, the plots are unique for each ice type, (b) Histograms of ice types shown in Figure 3.3(a).

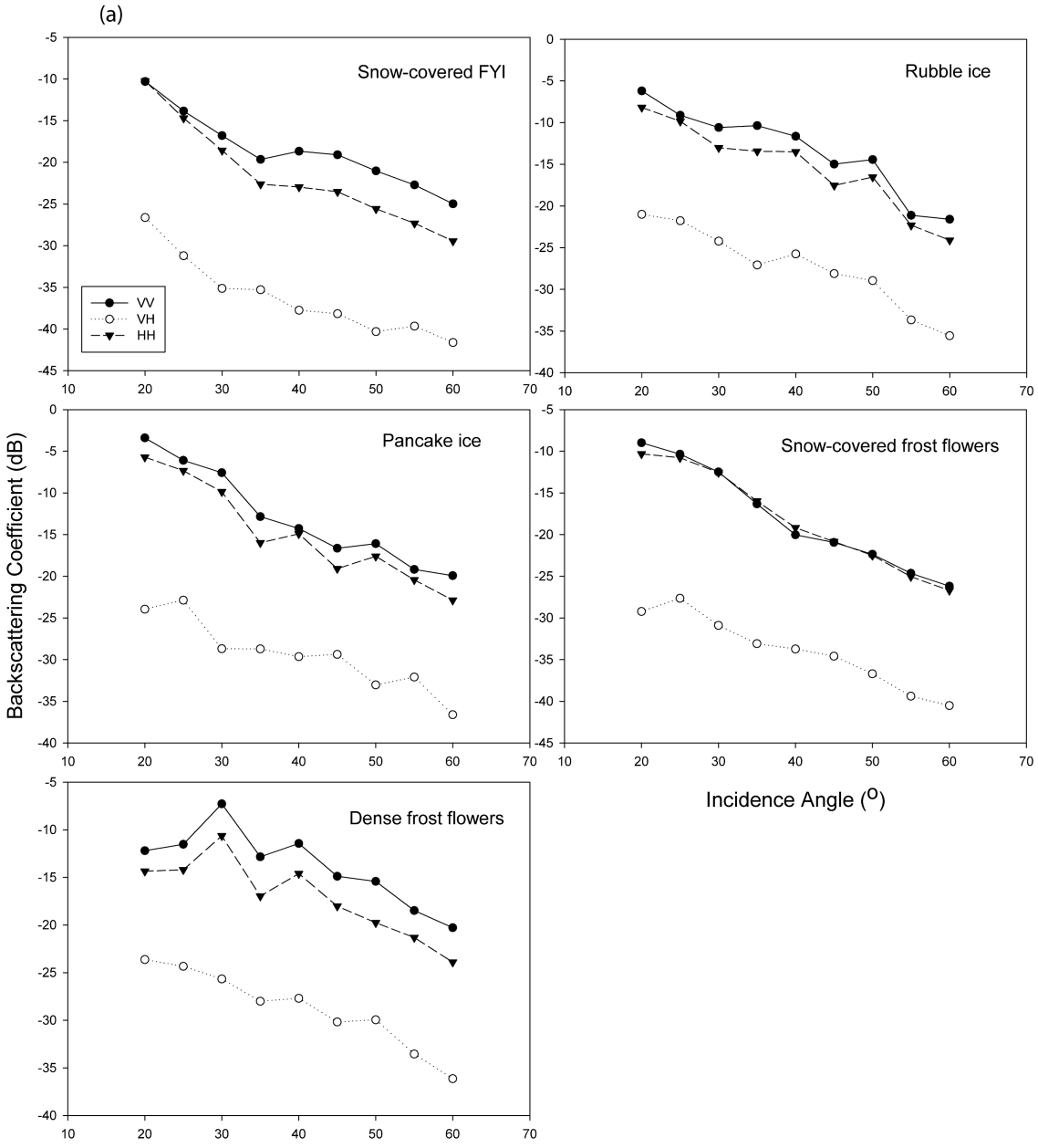

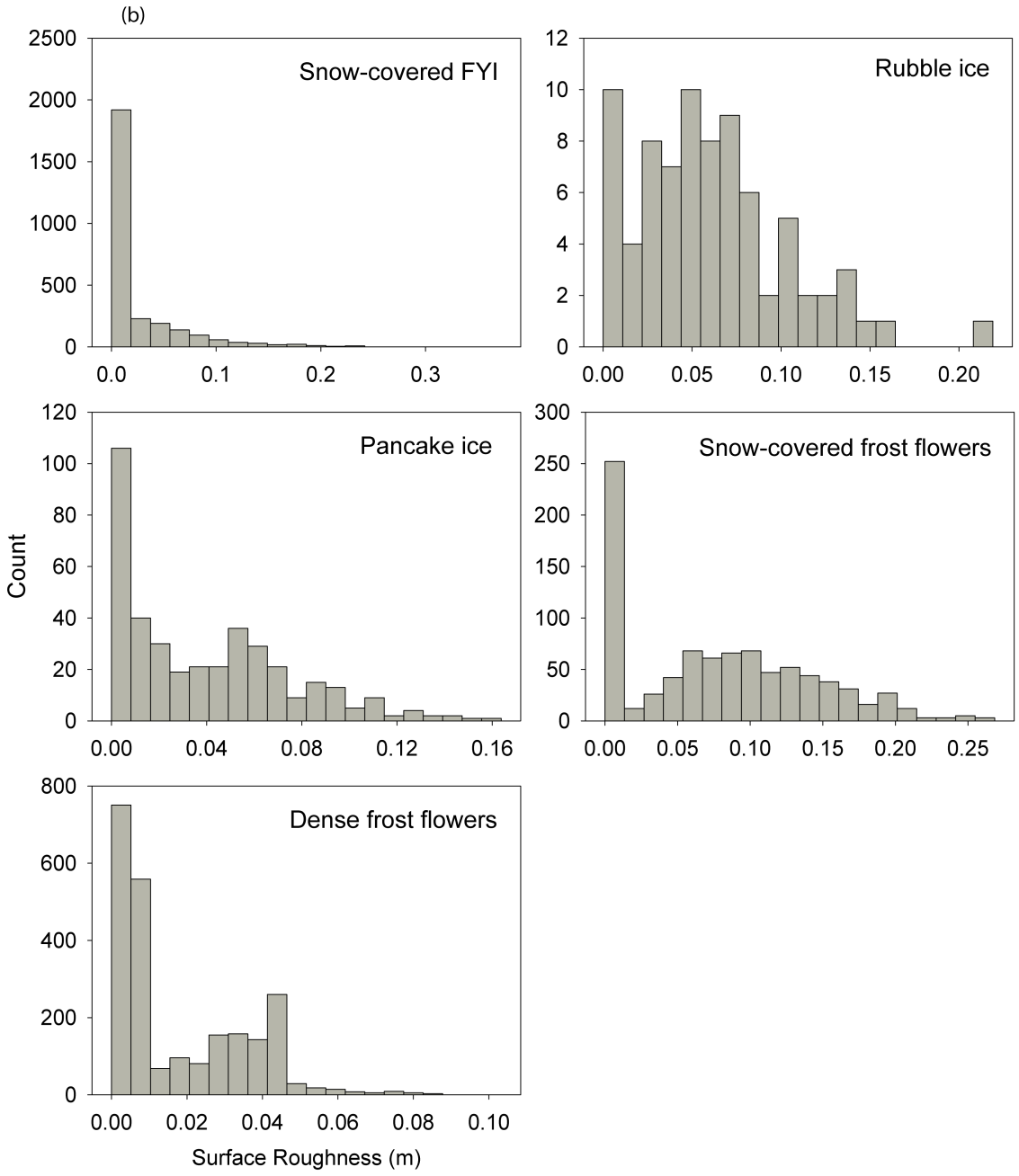
(b)
Snow-covered FYI
Rubble ice
Pancake ice
Snow-covered frost flowers
Dense frost flowers
Count
Surface Roughness (m)

Figure 3.4. (a) Groups, displayed as alphabets and plotted as comparison circles, are derived from the ANOVA using AMW backscattering coefficient (HH, VH, and VV polarization) using Tukey's method. It is observed that five (HH: *A*-*E*), three (VH: *A*-*C*), and six (VV: *A*-*F*) different groups are distinct, (b) Similar group as in (a) but for T_b 37-H, 37-V, 89-H, and 89-V. We observe only one group for each data (*A*). The line across each diamond represents the group mean. The vertical span of each diamond represents the 95% confidence interval for each group. The gray line across the plots and circles is grand mean. Groups that are not different show as thin red circles; groups that are different from selected group show as thick gray circles; and selected circle, as an example, is thick red.

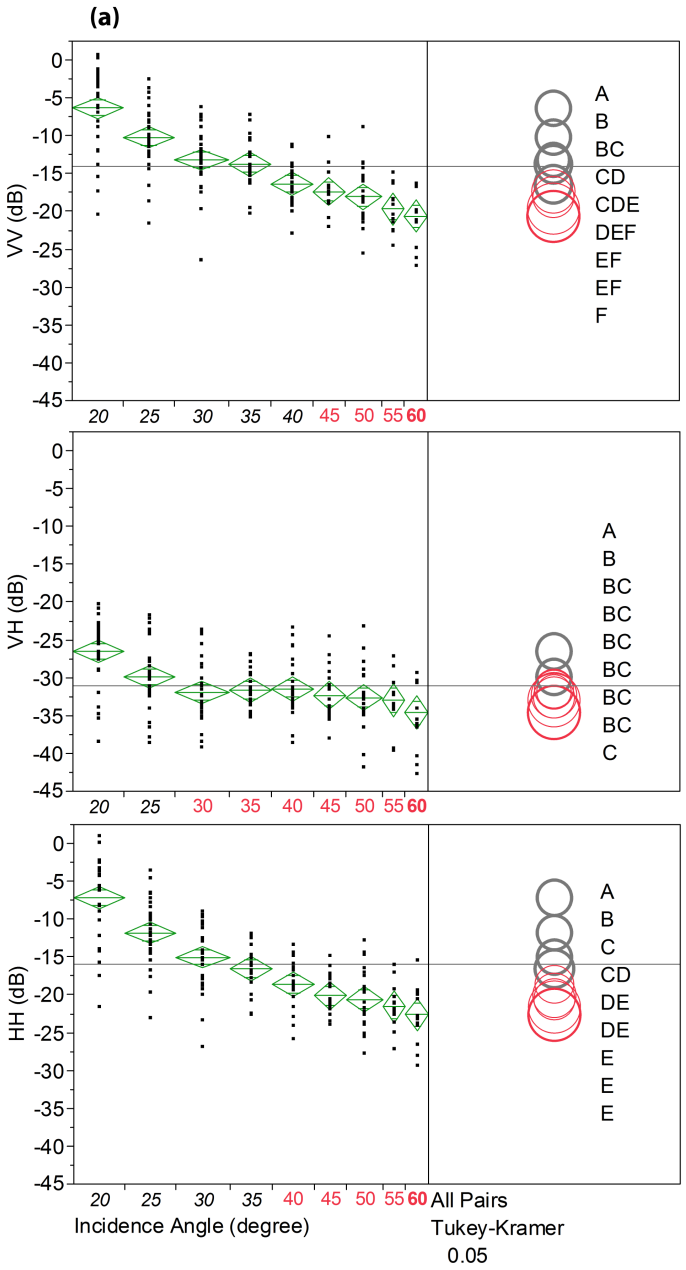

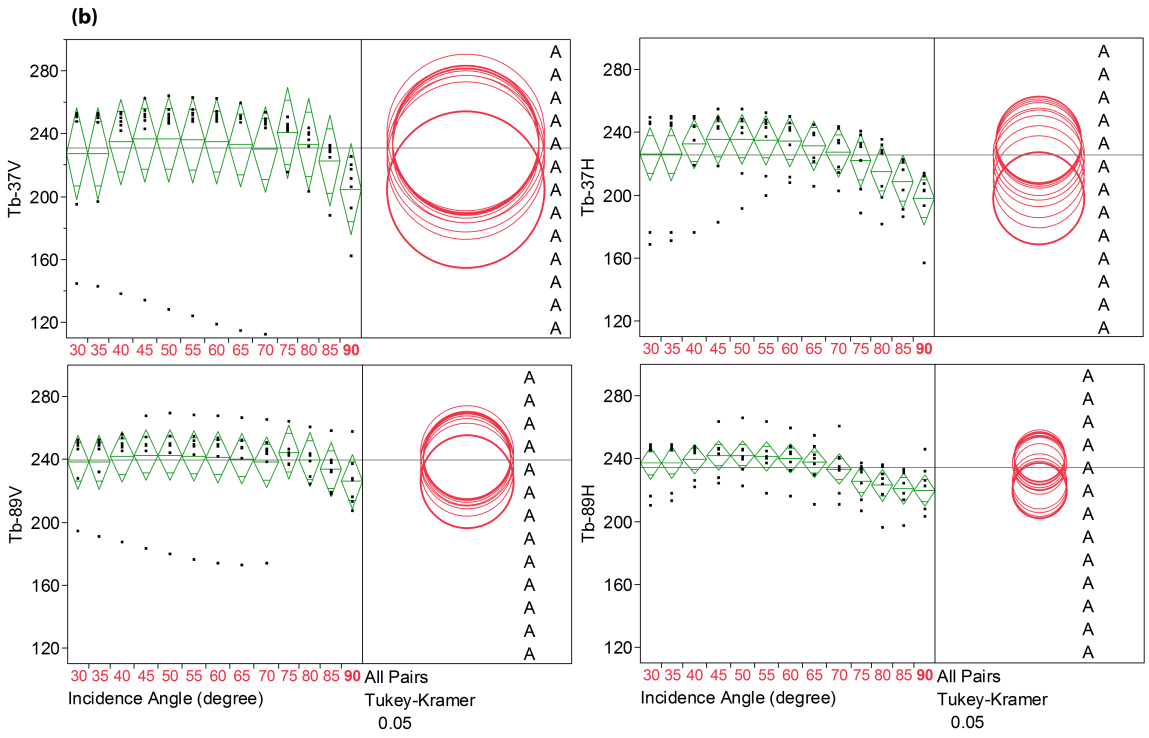

In our data, there is no specific standard nomenclature applicable to the identified roughness type, so large-scale roughness has been identified using helicopter-based video data. These corresponded to larger-scale roughness types compared to ship-based roughness types, which are small-scale. These survey flights were obtained opportunistically as we conducted scientific operations in the study region. They are considered representative, but not exhaustive, of the range of surface roughness types present in this portion of the southern Beaufort Sea MIZ. Helicopter-based laser data is capable of addressing large-scale roughness (footprint: 1054.37 m^2) of ice floes typically found in MIZ. The ship-based laser, on the other hand, is capable of resolving small-scale roughness features associated with ice types (footprint: 1.55 m^2) (Table 3.1).

Figure 3.5. T_b plot of different types of sea ice at 37 and 89 GHz frequencies. These five sea ice types were visually identified and the statistical analysis of T_b data did not discriminate ice roughness types.

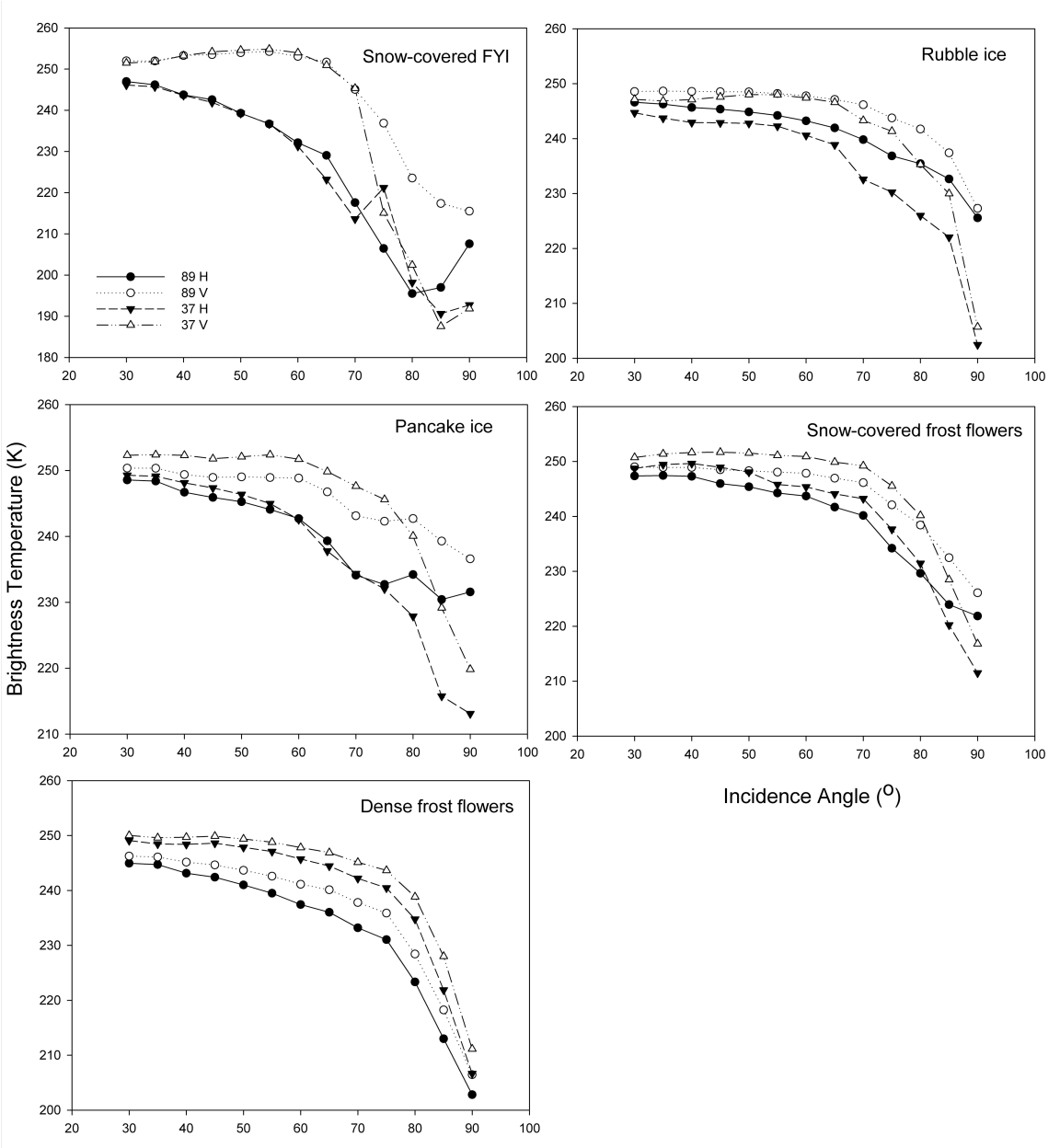

The total number of ship-laser profiler data samples is 17, and all profiles are mutually independent. Kolmogorov-Smirnov normality test (KS = 0.329, *P*-value < 0.010) suggests that the population is non-normal. Levene's test (p = 0.000) for equal variances

shows the majority of data centred on 95% Bonferroni confidence interval for standard deviations. Levene's test predominantly suggests that the variances are significantly different. Non-parametric test, Wilcoxon Signed Rank, was also used to check the differences in the variances (Z-statistic based on positive ranks = 50.074, $p < 0.001$), which again suggests a statistically significant difference in the medians. Therefore, groups cannot be formed in this dataset.

Helicopter-based laser altimeter data consisted of a number of profiles from different sea ice regimes spanning- rough ice, mixtures of ice and open water, and a wide variety of sea ice topography. A total of n = 34 different profiles, with varying number of data points in each, were used (total N = 21125; mean = 0.40 m; standard deviation = 0.58 m). The Kolmogorov-Smirnov normality test (KS = 0.238, $p < 0.010$) and the equality of variances examination (Levene's test statistic with 95% Bonferroni confidence interval for standard deviation = 154.97; *P*-value = 0.000) suggest that the data is non-normal and the variances in the data are significantly different. Tukey's method is able to form groups if a few profile variances are similar in the data, but the data shows that individual profile variances are too different to form groups. Therefore, groups of similar variances cannot be formed on the basis of ANOVA.

3.5.2. Statistical Analyses of Backscattering Coefficients

The scatterometer (footprint at 55°: 2.13 m^2) is capable of addressing small-scale roughness. In a recent study, Kim et al. (2012) have detected small-scale roughness from RADARSAT-2. We acquired data over different sea ice types with varying surface roughness, the challenge being the separation of dielectric properties and the surface

roughness from the observed signal. As our data is taken from FYI (saline) dominated MIZ, the majority of the radar return from the ice is backscattered energy from the surface, with negligible penetration (~10 cm) into the ice (Hallikainen and Winebrenner, 1992). Therefore, the plots in Figure 3.3 represent backscattering predominantly caused by the surface roughness. An important point to consider is the relationship between information contained in the backscattering coefficient and the manual observation of ice type/surface roughness. We observe that it is extremely difficult to separate out surface roughness/ice types through only visual methods; hence, we use the statistical methods, e.g., ANOVA, for separation of different classes that vary in their variances.

The backscattering data in VV follows a normal distribution evidenced through a Kolmogorov-Smirnov normality test (VV: KS = 0.065, p = 0.042; VH: KS = 0.064, p = 0.045; HH: KS = 0.058, p = 0.093). The Levene's test for equal variances shows that the null hypothesis cannot be rejected (VV: p = 0.114; VH: p = 0.571; HH: p = 0.100), i.e. the variances of backscattering coefficients are not significantly different and the data are considered mutually independent. The assumptions of Tukey's method and the ANOVA are met.

The alphabetic letters in a Tukey group represent the classes of means that are similar in the data. The lowest mean starts from letter *A*. For example, in VV analysis, there are six different groups (*A*-*F*). The overlapping between the groups suggests that at a particular incidence angle, the backscattering signatures of different sea ice/roughness are mixed. In other words, different ice types/roughness have similar backscattering coefficient at an incidence angle. Some of these classes carry mixed signatures of different ice types/roughness at median incidence angles. At low mean (e.g., *A*, *B*) and at

high mean (e.g., *E*, *F*), the groups are distinct to an ice type/roughness. It is difficult to pinpoint from here which type of ice contributes to which group. This analysis is based only on the sample means of backscattering coefficient. It is possible that different types of ice/roughness may have the same mean in the data at different incidence angles. However, field measurements of dielectric constant of identified groups will help ascertain the link between obtained classes and ice type/roughness. In addition to five visually observed surface types, more data acquired over a large number of surface types will further improve the statistical classification. The number of classes identified for HH, VH, and VV result from the EM response of sea ice observed at different incidence angles.

3.5.3. Statistical Analyses of Brightness Temperature

The T_b typically gradually decreases with increasing incidence angles due to less energy that returns to the sensor at the larger incidence angles (Figure 3.5). However, the increase in the T_b is directly related to increase in the surface area covered by the footprint of the sensor (the larger the surface area, the larger is the emission per square unit of the ice surface). At the same time, the observations were taken only from one direction for the surface area exposed to the radiometer sensor. The directional dependence of T_b measurements is not considered due to this limitation (Stroeve et al., 2006). We performed ANOVA to further investigate the T_b based on variance in the data.

The Kolmogorov-Smirnov normality test of T_b data at 37 and 89 GHz for both polarizations (37V: KS = 0.291; 37H: KS = 0.161; 89V: KS = 0.227; 89H: KS = 0.122; $p < 0.010$ for both polarizations) suggests that the data is non-normal. The data do not

qualify for the ANOVA in this case. The test for homogeneity (Levene's test) of variance, however, shows $p > 0.050$ (for all polarizations), which means the data variances are not significantly different. It satisfies the assumptions required for conducting Tukey's method for grouping. As the data are non-normal, we also apply non-parametric Kruskal-Wallis test for 37 H ($p = 0.008$), 37 V ($p = 0.002$), 89 H ($p = 0.004$), and 89 V ($p = 0.220$) for testing medians. The null hypothesis cannot be rejected for 89 V data, which means the population medians are all equal for 89 V. For all other frequency/polarization combinations, medians are not equal. This shows that ice types that have different statistical variances in surface heights (also determined through visual observation), may not necessarily show different statistical variances in T_bs. Thus, ice classes identifiable from detectable physical roughness are not fully comparable to ice classes identifiable from T_bs. The radiometers could only resolve small-scale roughness underlying the footprint (at 55° incidence: 6.62 m^2 for 37 GHz and 6.36 m^2 for 89 GHz).

3.6. Conclusions

We have provided the ANOVA of the surface roughness using ship-based, aerial, and, AMW and PMW methods. A number of visually identifiable ice types were obtained from the helicopter- and ship-based data but manual identification appeared insufficient. We identified small-scale roughness classes using a ship-based laser profiler, and large-scale roughness classes using a helicopter-based laser altimeter. A more detailed statistical discrimination of roughness using ANOVA of AMW and PMW data was presented.

The ANOVA of AMW data suggests that group variances may differ significantly when observed from different angle of incidences. We observe that at mid incidence angles (40°–50°) the observed groups overlap, which implies that the microwave signatures of the surface are statistically manifested as similar at the same incidence angle. This is true for all polarization combinations, e.g., HH, VH, and VV. The potential utility of being able to discriminate roughness/ice classes is to obtain mid incidence group variances from polarimetric satellite data (Kim et al., 2012) (e.g., in orbit; RADARSAT-2, and RISAT-1; future missions: RADARSAT Constellation Mission (RCM), and Sentinel-1, 3), which can provide large temporal (revisit twice a day) and spatial information (required sub-meter or nearly so) on the ice types/roughness. Future mission such as Sentinel-3, which is likely to have dual frequencies, can provide a great promise for significant improvement in small-scale surface roughness detection. This can be regarded as a considerable improvement over visually identified ice types/surface roughness classes.

The nature of T_bs over different sea ice surfaces remains the subject of investigation. We observed that, although the surface types were dissimilar, the T_bs of visually identifiable surfaces did not differ significantly, except for the cases where snow cover was significant. This in fact, leads us to conclude that directional dependence of T_b could be of utmost importance for meaningful extraction of surface roughness from the T_b (Stroeve et al., 2006). The surface area of sea ice exposed to the radiometer sensor may be considerably large or small depending on the measurement direction. The data were obtained from different visible sea ice surface types with large spatial and temporal variability and sea ice surface types. This suggests that PMW emissions of sea ice (based

on our dataset) may not contain detectable variances in surface roughness within the FOV/footprint of the sensor. 89 GHz provides a smaller footprint and thus can be a good resource for small-scale surface roughness studies at sub-pixel scales (millimeter to meter). In other words, the surface roughness of sea ice when observed through PMW emissions may not adequately discriminate surface roughness elements contained within the MIZ. Algorithms incorporating multiple PMW frequencies (such as in AMSR-E, SSMIS) can significantly improve roughness classification.

The statistical discrimination of sea ice surfaces found in MIZ using microwave methods (active and passive) can be further explored using satellite remote sensing and can pave the way for remote discrimination of surface roughness. We have not considered the effect of surface roughness anisotropy on backscattering coefficient (dependence of backscattering on the direction of measurement to account for slope, orientation and surface geometry) due to lack of large number of surface types, which may considerably affect the results. Unfortunately, difficulties associated with extreme weather conditions and limitations to navigation in the Arctic restrict a detailed data acquisition; however, a tank experiment could be a useful alternative. Integration of backscattering with physical roughness under changing seasons to develop new radiative transfer models is envisaged as avenues of future research. Following our findings, similar results can be obtained and compared for entire/different regions of the Arctic Ocean for winter and summer seasons.

Chapter 4

C-Band Polarimetric Coherences and Ratios for Discriminating Sea Ice Roughness

Mukesh Gupta[1*], Randall K. Scharien[1, 2], and David G. Barber[1]

International Journal of Oceanography, vol. 2013, Article ID 567182, 1–13, 26 April 2013, doi:10.1155/2013/567182

[1]Centre for Earth Observation Science, Department of Environment and Geography, Clayton H. Riddell Faculty of Environment, Earth and Resources, University of Manitoba, 463, Wallace Building, Winnipeg R3T 2N2, Manitoba, Canada

[2]Now at: Department of Geography, University of Victoria, Victoria V8W 2Y2, British Columbia, Canada

[*]Corresponding Author

Abstract

The rapid decline of sea ice in the Arctic has resulted in a variable sea ice roughness that necessitates improved methods for efficient observation using high-resolution spaceborne radar. The utility of C-band polarimetric backscatter, coherences, and ratios as a discriminator of ice surface roughness is evaluated. An existing one-dimensional backscatter model has been modified to two-dimensions (2D) by considering deviation in the orientation (i.e. the slopes) in azimuth and range direction of surface roughness simultaneously as an improvement in the model. It is shown theoretically that the circular coherence (ρ_{RRLL}) decreases exponentially with increasing surface roughness. The cross-polarized coherence (ρ_{HHVH}) is found to be less sensitive to surface roughness; whereas the co-polarized coherence (ρ_{VVHH}) decreases at far range incidence angles for all ice types. A complete validation of the adapted 2D model using direct measurements of surface roughness is suggested as an avenue for further research.

4.1. Introduction

Arctic sea ice is going through a rapid decline (Kwok and Cunningham, 2010; Kwok and Rothrock, 2009). Thinner first-year ice (FYI) is replacing multiyear ice, leaving an ice cover, which is more sensitive to deformation and changes in atmospheric and ocean forcing. Increased open water and marginal ice zones (MIZs), due to the enhanced mobility of a relatively thinned pack ice, are further susceptible to increases in surface roughness and greater surface roughness variability (Nghiem et al., 2007). Greater surface roughness in the MIZ is of importance due to higher rates of heat flux (McPhee et al., 2008) and momentum (Andreas et al., 2010) exchanges occurring across the ocean-sea ice-atmosphere interface, greater biological productivity (Lavoie et al., 2009), and potential limitations imposed on ship navigation. Although the literature contains information on how the MIZ responds to wind and wave forces, it is necessary to investigate the electromagnetic (EM) response of the MIZ to facilitate satellite-based observations. Satellite-based observation is necessary due to the scarcity of surface observations in a MIZ, as well as the difficulties in collecting physical measurements due to the instability and roughness of the ice floes.

The use of polarimetric synthetic aperture radar (pol-SAR) represents a promising approach for satellite-based monitoring of surface roughness and, concurrently, discriminating sea ice types within a MIZ. A pol-SAR records the amplitude and phase information of backscattered energy for four transmit-receive polarizations (HH, HV, VH, and VV), thereby facilitating the derivation of the full polarimetric response of the target. It is recognizable that the diversity in polarization achievable by pol-SARs or even by dual-polarization SAR systems provides more complete inference of target features

(e.g., sea ice) than conventional, single channel SARs. Furthermore, recently launched pol-SARs are capable of higher spatial resolution (< 10 m) imaging, leading to enhanced potential for monitoring complex ice environments.

Discrimination of ice types using SAR has been conventionally achieved by utilizing different combinations of linearly polarized backscattering coefficients (Kwok et al., 1992; Melling, 1998; Wohl, 1995). Multiyear ice, smooth FYI, rough FYI and new ice/open water in the Beaufort and Chukchi Seas during March have been identified using a single polarization SAR image intensity-based classification scheme (Wohl, 1995) while others used single polarization SAR image texture analysis to discriminate new ice, FYI, and multiyear ice during the month of March in the Beaufort Sea and the Mould Bay respectively (Barber and LeDrew, 1991; Holmes et al., 1984). Dual co-polarized backscattering coefficient differences in HH and VV have been used to discriminate FYI, multiyear ice, and lead areas in the Beaufort Sea during March (Nghiem and Bertoia, 2001). However, the complexities in polarimetric signatures associated with the dynamic mixture of surface roughness and ice type conditions in a MIZ during fall freeze-up remain to be examined. Such an examination requires utilizing polarimetric radar backscatter, so that the material (dielectric) and geometrical properties of the surface, which influence backscatter, may be individually assessed.

In this study, ship-based observations of co- (linear) and cross-polarized backscatter, circular polarimetric coherences (ρ_{VVHH}, ρ_{HHVH}, and ρ_{RRLL} respectively), as well as co-polarized and cross-polarized polarization ratios (γ_{co} and γ_{cross} respectively), are used to evaluate their utility for ice surface discrimination capabilities using a polarimetric radar operating in C-band (5.5 GHz). Characteristics of these polarimetric parameters for a

variety of ice types in a MIZ during fall freeze-up are assessed with the following objectives:

1. To investigate the performance of polarimetric ρ_{RRLL} for sea ice surface roughness discrimination by adapting the one-dimensional backscatter model of Schuler et al. (2002) to two-dimensions and introducing roughness as deviations in range and azimuth directions.
2. To evaluate the utility of C-band polarimetric backscatter, coherences, and polarization ratios as a discriminator of surface roughness or ice type in a MIZ during fall freeze-up.

Figure 4.1. Geographic map of study area showing sampling locations.

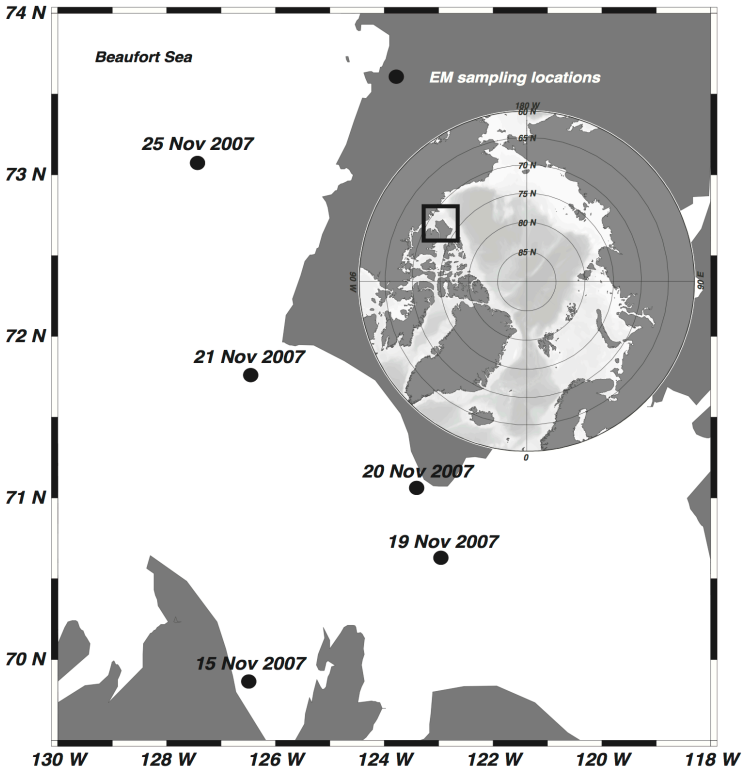

4.2. Methodology

4.2.1. Study Area

The study area is located in the southern Beaufort Sea and Amundsen Gulf regions in the western Canadian Arctic (Figure 4.1). The seasonal Cape Bathurst Polynya forms in the region and hosts a number of flaw leads during the winter (Barber and Hanesiak, 2004). During fall freeze-up, this area contains a variable mix of ice types under various stages of formation, e.g., new ice, pancake ice, frost flowers, deformed ice, gray ice, and nilas (Figure 4.2). The photographs in Figure 4.2 *a*, *b*, *c*, and *e* were taken at an oblique angle from the port side of the Canadian Research Icebreaker *Amundsen* at approximately eight meters height using a hand-held digital camera after a given scatterometer scan; and Figure 4.2 *d* was taken at nadir angle on the ice floe at about one meter height. In the present study, thin FYI types are considered (first stage: 30-50 cm- as per World Meteorological Organization nomenclature), which include snow-covered FYI, pancake ice, frost flowers and deformed FYI located within the MIZ. Data described in the following sections were acquired as part of the Circumpolar Flaw Lead (CFL) System Study project of the International Polar Year (IPY) 2007-08 over the period October 2007- August 2008 (Barber et al., 2010). Ancillary meteorological data were collected through a ship-based AXYS Technologies Inc., (Sydney, BC, Canada) Automatic Voluntary Observing Ships (AVOS) system. This system was mounted approximately 20 m above sea level on the wheelhouse to minimize the ship's influence and could measure air temperature and wind speed.

4.2.2. Theoretical Formulation

Sea ice is a distributed radar target, and the conditions of stationarity and homogeneity seldom hold for dynamically changing ice in a MIZ. The radar backscattering is therefore analyzed using temporally and spatially varying stochastic processes. Backscatter from sea ice is incoherent and either partially or completely polarized, as described by the polarimetric covariance matrix. The electric field vector of an incident (*i*) and scattered (*s*) EM wave can be given by,

$$\boldsymbol{E}^i = E_{Hi}\widehat{\boldsymbol{h}} + E_{Vi}\widehat{\boldsymbol{v}}, \tag{4.1}$$

$$\boldsymbol{E}^s = E_{Hs}\widehat{\boldsymbol{h}} + E_{Vs}\widehat{\boldsymbol{v}}. \tag{4.2}$$

where, *H* and *V* represent horizontal and vertical polarizations respectively. $\hat{h}$ and $\hat{v}$ are the unit vectors in the horizontal and vertical directions of polarization respectively. The incident (*i*) and scattered field (*s*) can be either *H* or *V*. The scattered electric field is related to the incident electric field by the scattering matrix, *S* defined as,

$$\begin{bmatrix} E_{Hs} \\ E_{Vs} \end{bmatrix} = \frac{e^{-jkr}}{r} \begin{bmatrix} S_{HH} & S_{HV} \\ S_{VH} & S_{VV} \end{bmatrix} \begin{bmatrix} E_{Hi} \\ E_{Vi} \end{bmatrix}, \tag{4.3}$$

$$\begin{bmatrix} S_{HH} & S_{HV} \\ S_{VH} & S_{VV} \end{bmatrix} = S. \tag{4.4}$$

where, $\frac{e^{-jkr}}{r}$ term accounts for wave propagation effects in amplitude and phase. If the orientation of a surface such as sea ice in azimuth direction is rotated by an angle, the

corresponding new backscatter matrix can be constructed as provided by Lee et al. (2000).

The coherency matrices can be derived as co-polarized Eq. (4.5), cross-polarized Eq. (4.6) and circular (RRLL: right-right left-left rotation of the electric field vector about the line of sight) Eq. (4.7) coherences in magnitude form (Lee et al., 2000; Schuler et al., 2002) as (for derivation of ρ_{RRLL}, see Appendix-4A),

$$\rho_{\mathrm{VVHH}} = \frac{\langle |S_{\mathrm{VV}} S_{\mathrm{HH}}^{*}| \rangle}{\sqrt{\langle |S_{\mathrm{VV}}|^2 \rangle \langle |S_{\mathrm{HH}}|^2 \rangle}}, \tag{4.5}$$

$$\rho_{\mathrm{HHVH}} = \frac{\langle |S_{\mathrm{HH}} S_{\mathrm{VH}}^{*}| \rangle}{\sqrt{\langle |S_{\mathrm{HH}}|^2 \rangle \langle |S_{\mathrm{VH}}|^2 \rangle}}, \tag{4.6}$$

$$\rho_{\mathrm{RRLL}} = \frac{\langle |S_{\mathrm{HH}} - S_{\mathrm{VV}}|^2 \rangle - 4\langle |S_{\mathrm{HV}}|^2 \rangle}{\langle |S_{\mathrm{HH}} - S_{\mathrm{VV}}|^2 \rangle + 4\langle |S_{\mathrm{HV}}|^2 \rangle}, \tag{4.7}$$

$$\gamma_{co} = \frac{S_{\mathrm{VV}}}{S_{\mathrm{HH}}}, \tag{4.8}$$

$$\gamma_{cross} = \frac{S_{\mathrm{HV}}}{S_{\mathrm{HH}}}. \tag{4.9}$$

where S is the complex scattering matrix; and an asterisk (*) represents the complex conjugate. The brackets $\langle . \rangle$ represent ensemble averages of the observed data. There were approximately 34 pulses sent per incidence angle. An ensemble average was performed on those 34 pulses. Raw data were processed into range profiles and were averaged in the azimuth for each measured incidence angle. Polarimetric ratios γ_{co} and γ_{cross} are simply power ratios of backscattered energy. Polarimetric coherences and polarization ratios have demonstrated utility in reducing the ambiguities caused by the non-linearity

between system response and target properties. Regarding Arctic sea ice, some literature is available on the use of ρ_{VVHH}, ρ_{RRLL} and γ_{co} at different EM frequencies. C-band backscatter coefficients (HH, HV, and VV) and ρ_{VVHH} have been used to characterize various FYI types (compressed, rubble and ridge, and smooth) and multiyear ice (Rignot and Drinkwater, 1994). Thin sea ice has been effectively discriminated from FYI using C-band γ_{co} ratio (Geldsetzer and Yackel, 2009). ρ_{VVHH} and γ_{co} have been used to discriminate Arctic leads using L-band radar signatures (Winebrenner et al., 1995). In a similar study, Wakabayashi et al. (2004) described polarimetric characteristics of different FYI types (thin ice, smooth, and rough) using L-band ρ_{RRLL} and γ_{co}, and showed the utility of coherences and ratios in discriminating ice types. Nakamura et al. (2005) discriminated ice surface using γ_{co} ratio in an observational study of lake ice using airborne L- and X-band SAR. These studies lack a holistic overview of the utility of different polarimetric coherences and ratios to discriminate thin FYI types in a MIZ.

4.2.3. Active Microwave Backscattering Data

C-band polarimetric backscattering data were collected using a completely stationary ship-mounted scatterometer system developed by ProSensing Inc. (Amherst, MA, USA) and mounted 7.56 m above the mean sea level on the port side of the *Amundsen* (Table 4.1). The system acquires backscatter and phase data in terms of the combinations of linear transmit and receive polarization combinations, HH, HV, VH, and VV at incidence angles 20°–60° (5° increments) over a 60° azimuth range. The calibration of the instrument was performed through the methods given elsewhere (Geldsetzer et al., 2007; Isleifson et al., 2010). Polarimetric backscattering data were collected from homogeneous

samples of snow-covered (dry and fresh) first-year ice (SCFYI), deformed FYI (DFYI), consolidated pancake ice (PI), snow-covered frost flowers (SCFF), and dense frost flowers (DFF) on different dates during November 2007. Data from each ice type sample comprised three to four contiguous scatterometer scans, which took up to 35 minutes to complete. The scatterometer had a footprint of 1.1 m^2 in the range direction at a 45° incidence angle (Isleifson et al., 2010) with the footprint increasing in size with incidence angle (Geldsetzer et al., 2007).

Table 4.1. Technical properties and specifications of C-band scatterometer.

System parameter	Value
RF output frequency	5.25–5.75 GHz
Transmit power at bulkhead connector	12 dBm
Antenna diameter	0.61 m
Transmit bandwidth	500 MHz
Antenna beamwidth	5.5°
Antenna gain	28 dB, nominal
Cross-polarization isolation	> 30 dB, measured at the peak of the beam
Transmit/receive polarizations	Linear, Vertical and Horizontal
Sensitivity, minimum NRCS at 15 m range	–40 dB m^2/m^2

Figure 4.2. Photographs of ice types used in the study. a) Snow-covered first-year ice (SCFYI), b) Deformed first-year ice (DFYI), c) Consolidated pancake ice (PI), d) Snow-covered frost flower (SCFF), and e) Dense frost flower (DFF).

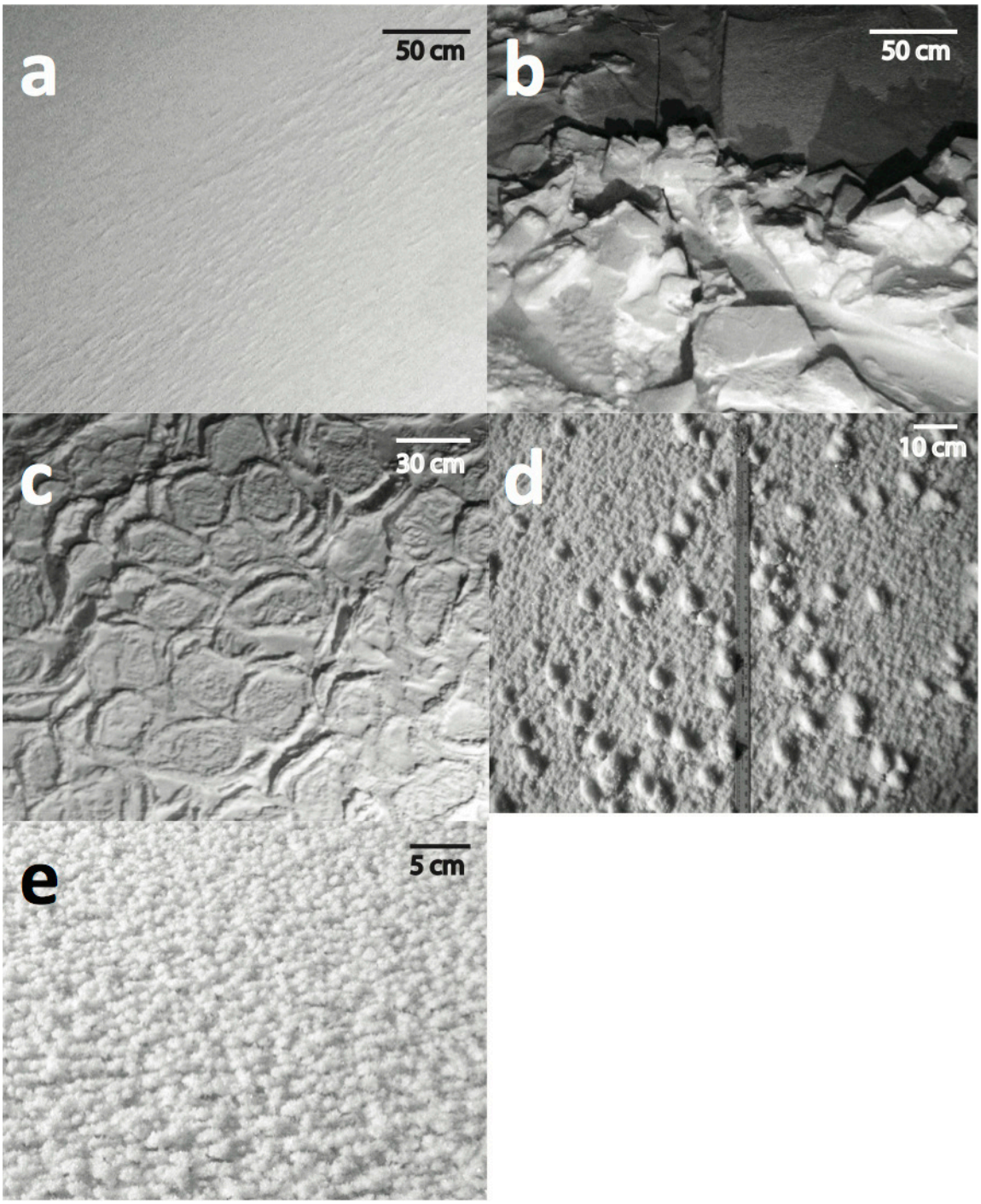

Towards objective 2, scan data for each ice type were grouped by incidence angle representing near (20°–25°), mid (35°–40°), and far (55°–60°) range groupings. These groupings best represent the diversity of scattering mechanisms available across the acquired incidence angle range. In the near range, surface scattering is expected to dominate the measured C-band backscatter, while surface-volume scattering is increasingly expected to influence C-band backscatter beyond approximately 30°, i.e. mid to far ranges (Nghiem et al., 1995). Furthermore, combining data from adjacent incidence angles doubled the number of samples from 8 to 18 depending on ice type, although at the expense of range resolution. Scatterometer data had unequal number of data points in each range group, which does not fulfil parametric ANOVA requirements for statistical significance testing. Polarimetric coherences and ratios of ice types were tested for independence from each other for each incidence angle grouping. Testing was done using the non-parametric Kruskal-Wallis H statistic, with $\alpha = 0.01$ significance level (one-tailed) used as the threshold for statistical independence.

4.2.4. Surface Roughness and Circular Coherence

In pursuit of objective 1, a polarimetric backscattering model; which is mainly a Bragg backscattering (coherent scattering) model modified for surface roughness considering the surface slope by slightly changing the tilt of the surface from the horizontal, is used. Microwave measurements of surface roughness using co- or cross-polarization backscattered power are most successful in flat areas. In sea ice microwave remote sensing, the dielectric constant and topography (slope in range and azimuth) are important. According to Eq. (22) by Schuler et al. (2002) in the one-dimensional

scattering model, the circular coherence is only sensitive to surface roughness. Surface roughness has been considered as a change in the slope of ice in azimuth and ground range directions (Lee et al., 2000; Nghiem et al., 1992; Schuler et al., 2002). This is implemented mathematically in the Bragg backscattering model by considering roughness as a depolarizer, which conforms to reflection symmetry, i.e. the backscattering properties are identical on either side of the plane of incidence and HV = VH (Nghiem et al., 1992; Yueh et al., 1994). The distribution of azimuth slope angles θ_1 is considered as one-dimensional Gaussian-distributed (Schuler et al., 2002).

The rotation matrix (Lee et al., 2000) and the coherency matrix Schuler et al. (2002) are calculated after introducing the rotation in azimuth anti-clockwise about range direction. In this case, ρ_{RRLL} is derived as (Schuler et al., 2002),

$$\rho_{\mathrm{RRLL}} = e^{-8\sigma_{\theta_1}^2} . \tag{4.10}$$

where, σ_{θ_1} is the standard deviation of the orientation angle distribution in azimuth direction, and θ_1 is slope angle in azimuth direction. From Eq. (4.10), the ρ_{RRLL} is only dependent on the orientation of ice surface in the range direction, or the standard deviation of the orientation angle distribution (i.e. surface roughness). Here, the surface roughness is introduced through rotation by angle, θ_2 in the range direction anti-clockwise about azimuth direction (Figure 4.3). Angle θ_2 is not shown in Figure 4.3 due to complexity of the geometry. In this case also, the corresponding distribution of shift in orientation angle is Gaussian-distributed.

The new rotation matrix U_2 is given by,

$$U_2 = \begin{bmatrix} \cos 2\theta_2 & 0 & -\sin 2\theta_2 \\ 0 & 1 & 0 \\ \sin 2\theta_2 & 0 & \cos 2\theta_2 \end{bmatrix}. \quad (4.11)$$

The new averaged coherency matrix over the Gaussian distribution $p(\theta_2)$ can be calculated as,

$$\langle T \rangle_{\theta_2} = \begin{bmatrix} \zeta A & \mu B & 0 \\ \mu B^* & 2C & 0 \\ 0 & 0 & (1-\zeta)A \end{bmatrix}. \quad (4.12)$$

where $\mu\,(\theta_2) = \int \cos 2\theta_2 p(\theta_2)\, d\theta_2$, and $\zeta(\theta_2) = \int \cos^2 2\theta_2 p(\theta_2)\, d\theta_2$. B, a part of an element of coherency matrix, is defined according to scattering matrix, S (Schuler et al., 2002). B^* is the conjugate of B. Both B^* and B are not used in the computation of ρ_{RRLL}.

The ρ_{RRLL} can be computed as,

$$\rho_{\mathrm{RRLL}} = \frac{T_{22} - T_{33}}{T_{22} + T_{33}} = \frac{2C - (1-\zeta(\theta_2))A}{2C + (1-\zeta(\theta_2))A}. \quad (4.13)$$

$$\rho_{\mathrm{RRLL}} = \frac{4C - \left(1 - e^{-8\sigma_{\theta_2}^2}\right)A}{4C + \left(1 - e^{-8\sigma_{\theta_2}^2}\right)A} \quad (4.14)$$

where $A = |S_{HH} + S_{VV}|^2$, $C = \frac{1}{2}|S_{HH} - S_{VV}|^2$; and $\zeta(\theta_2) = \frac{1}{2}\left(1 + e^{-8\sigma_{\theta_2}^2}\right)$. T_{ij} represents (i, j)th element of the matrix, $\langle T \rangle_{\theta_2}$ given in Eq. (4.12).

Given the above, the ρ_{RRLL} is dependent on the standard deviation of the orientation angle distribution in range, and the dielectric constant of the surface. Thus, it is shown that the new ρ_{RRLL} is exponentially changing with the change in orientation angle in the azimuth direction, but it behaves in a way, given by Eq. (4.14), and is dependent on both surface roughness (standard deviation) and the dielectric constant (scattering matrix) of the surface when roughness in two directions is considered. In our model, when two-dimensional roughness is considered, circular coherence is observed to be sensitive to surface roughness and dielectric constant both, thus making it difficult to differentiate roughness. 2D model being more realistic requires further considerations of separating dielectrics from roughness.

Figure 4.3. Illustration of scattering plane geometry with slight deviations in the orientation angles in azimuth (θ_1) and range directions (θ_2: not shown) respectively as means of two-dimensional surface roughness.

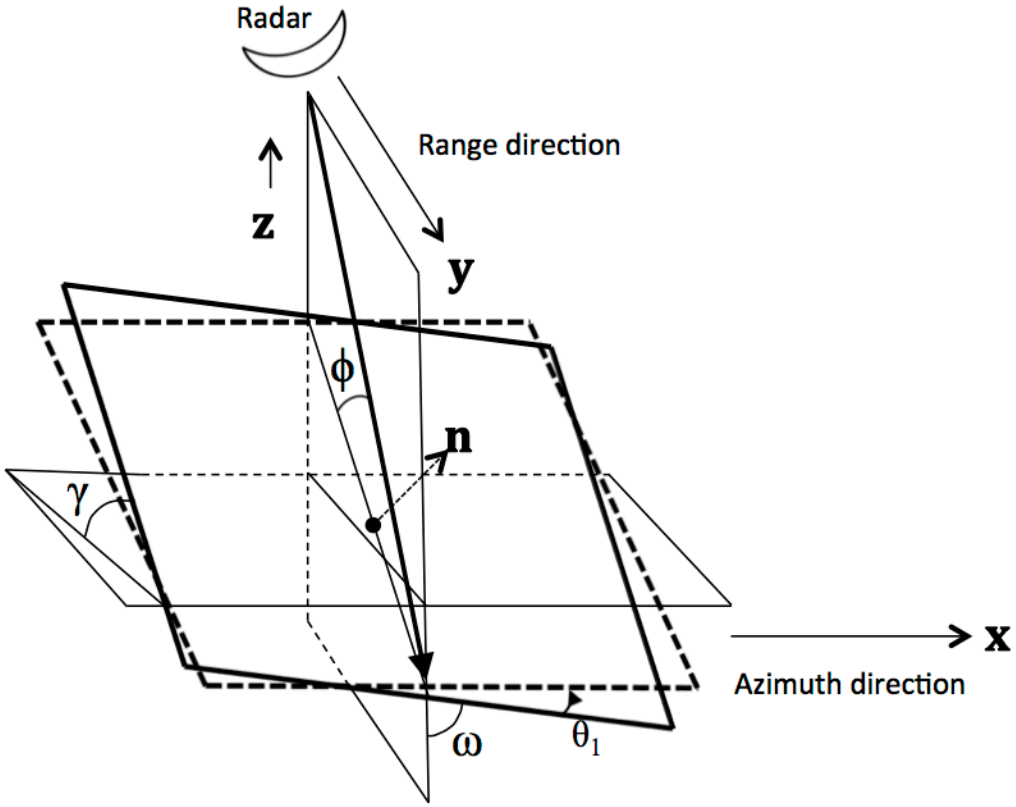

Now, the slope-induced roughness is examined in the range direction only. Lee et al. (2000) gave a relationship between slope in azimuth, slope in ground range, radar look angle (ϕ), and rotation in azimuth. Schuler et al. (2002) expressed this relationship in terms of root mean square (rms) surface height (s) and correlation length (l), assuming that the range slope, and orientation in azimuth, are small perturbations around their means,

$$\rho_{\mathrm{RRLL}} = e^{-16\left(\frac{s^2}{l^2 sin^2\phi}\right)}. \tag{4.15}$$

Figure 4.4 shows the incidence angle dependence of ρ_{RRLL} by varying the $\frac{s^2}{l^2}$ ratio. As the roughness increases, ρ_{RRLL} decreases. For $l >> s$, i.e. the surface is very smooth, the maximum value of ρ_{RRLL} approaches unity. ρ_{RRLL} decreases exponentially from unity to a fixed value of $\frac{s^2}{l^2}$ ratio at a particular incidence angle. A rough surface yields a smaller ρ_{RRLL}, which increases with increasing radar look angle. The range of $\frac{s^2}{l^2}$ for the presented ice classes is expected to lie between 0.001 and 0.1 (Carsey, 1992).

The relationship between slopes in azimuth and range direction is further demonstrated. Corresponding shifts and radar incidence angle is given by (see Appendix-4B),

$$\frac{\tan\omega}{\tan\theta_1} = \sin\theta_2(\tan\gamma.\sin\phi + \cos\phi) + \cos\theta_2(-\tan\gamma.\cos\phi + \sin\phi). \qquad (4.16)$$

where $\tan\omega$ is azimuth slope, $\tan\gamma$ is range slope, θ_1 and θ_2 are the perturbations in orientation in azimuth and range directions respectively, and ϕ is radar look angle. Figure 4.4 represents the case when orientation shift in the range direction is observed. In a sea ice remote sensing context, both surface roughness and the dielectric constant of ice affect ρ_{RRLL} when slope is changed in azimuth direction; whereas only surface roughness affects ρ_{RRLL} when slope is changed in range direction.

4.3. Field Results

4.3.1. Sea Ice Type Discrimination (Coherences and Ratios)

The date and hour of scatterometer data acquisitions corresponding to each sea ice type, as well as coincident meteorological parameters wind speed, air temperature, and relative humidity are provided in Table 4.2. The photographs of the selected ice samples are shown in Figure 4.2. With the exception of wind speed, there is negligible variation in meteorological conditions between ice type scans. As such, it is expected that between-scan, temperature-induced effects on the dielectric properties and backscattering intensities from the different ice types are negligible.

Figure 4.5 shows backscattering coefficients for co- (HH and VV) and cross-polarization (HV) configurations of each ice type. The two frost flower cases (DFF and SCFF) are plotted separately to exemplify differences in backscattering behavior on the basis of their different frost flower concentrations. The DFF and SCFF have a visually measured concentration of approximately > 95% and 20% respectively. While SCFYI is visually separable using, HH, HV, and VV polarizations at all incidence angles (low backscatter), PI and DFYI signatures overlap and are difficult to separate from each other. This may be indicative of PI geometry within the scatterometer footprint, as PI comprises of a series of upturned edges and flat areas of ice (see Figure 4.2). The curvature of upturned PI edges causes a backscatter response similar to that caused by the deformations (upturned ice) in the DFYI. DFF and SCFF are differentiable at HV and VV polarization at mid to far incidence angles.

Figure 4.4. ρ_{RRLL} varying with squared ratio of rms surface height and surface correlation length; ρ_{RRLL} decays exponentially, however, it decays faster at steep incidence angles.

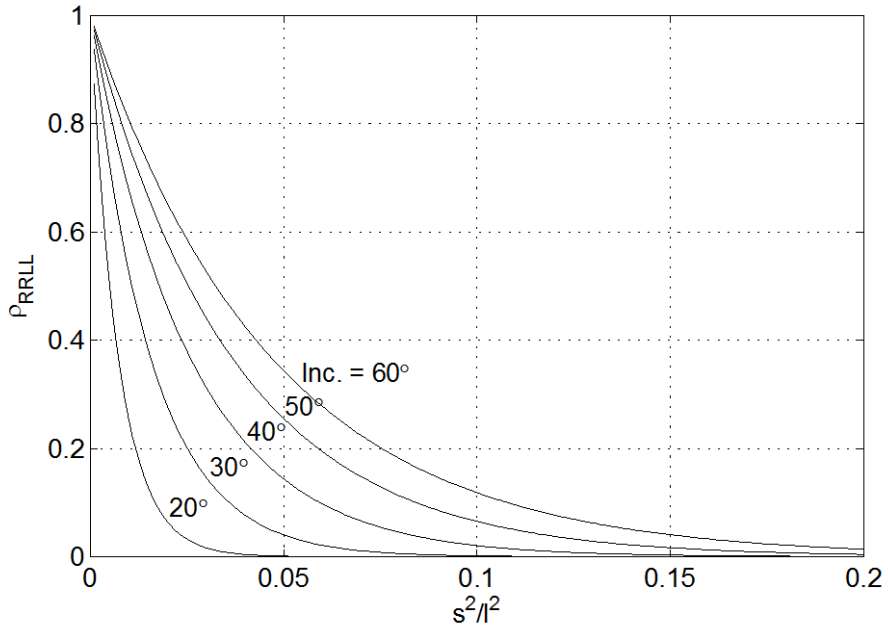

Mean coherences and polarization ratios for each ice type as a function of incidence angle grouping are documented in Table 4.3. All sea ice types show high ρ_{VVHH}, indicating low depolarisation and primarily single (surface) backscattering. The ρ_{HHVH} for DFF is notably higher than from the other ice types, which points to strong depolarisation caused by the frost flower structures. As shown in the previous section, a low value of ρ_{RRLL} indicates a rougher surface. At mid- to far-ranges in Table 4.3, the ρ_{RRLL} for DFYI is the lowest while for SCFYI it is the highest, which is consistent with the roughest and smoothest ice types, respectively.

Table 4.2. Meteorological parameters associated with each ice type on different dates.

	Sea Ice Type	Wind Speed (m/s)	Air Temperature (°C)	Relative Humidity %
Nov. 15, 2007 (Stn. 1117, 1400 hrs)	SCFYI	14.4	–16.0	85
Nov. 19, 2007 (Stn. 1100, 0030 hrs)	DFYI	13.9	–16.2	73
Nov. 20, 2007 (Stn. 1910, 0300 hrs)	PI	2.6	–13.5	79
Nov. 21, 2007 (Stn. 437, 1630 hrs)	SCFF	5.1	–16.2	82
Nov. 25, 2007 (Stn. 1812, 2100 hrs)	DFF	3.6	–16.6	86

Furthermore, for frost flower-covered surfaces, i.e. SCFF and DFF, the lower magnitude of ρ_{RRLL} is consistent with the higher concentration of frost flowers. At near-incidence angle range, the SCFYI shows higher roughness (i.e. lower ρ_{RRLL} = 0.47, Table 4.3) compared to that of PI (0.61). This may be due to the fact that the snow is dry and has low salinity, which allows EM waves to penetrate through the snow. This is likely to provide roughness of snow-ice interface rather than air-snow interface. At mid-incidence angle range, as expected, SCFYI shows lower roughness (i.e. higher ρ_{RRLL} = 0.65, Table 4.3) compared to that of PI (0.61). Mid-incidence angles are well suited for differentiating ice roughness/types using ρ_{RRLL}.

Looking at polarization ratios in Table 4.3, the γ_{co} increases rapidly with incidence angle, and is the highest at the far range for SCFYI. The γ_{co} ratio is also high for DFF,

but it remains fairly constant across all incidence angles. High γ_{co} is also representative of saline ice surface (FYI in this case) or surface scattering. The presence of dry snow (~ 1-2 cm) allows the EM waves to penetrate through snow, which causes reflection from the ice-snow interface. The γ_{co} behavior of SCFYI is consistent with that of a surface, which is very smooth (i.e. a Bragg surface), where the ratio between backscattered H and V is only dependent on incidence angle and dielectric constant (Cloude and Pottier, 1996). On the other hand, the γ_{co} behavior for DFF is consistent with that of a rough surface exhibiting backscatter from features with preferential vertical orientation (Geldsetzer et al., 2007). Including the γ_{cross} ratio in this comparison further supports the distinction in backscattering mechanisms. The near range γ_{cross} ratio is much smaller for SCFYI than DFF, indicating it to be much smoother. The DFYI and DFF show the highest overall γ_{cross}, due to multiple scattering within deformities for DFYI and depolarisation caused by frost flowers for DFF.

Figure 4.6 shows box-plots of coherences and polarization ratios of each ice type. Table 4.4 provides the significance values resulting from statistical tests for independence between each ice type based on a given coherence or ratio. All data in Figure 4.6 and Table 4.4 are based on the aforementioned incidence angle groupings from near to far range and, together, facilitate a conceptual approach to assessing the utility of each parameter for distinguishing ice types within a MIZ. Summarizing Figure 4.6 and Table 4.4, the near range ρ_{HHVH} and γ_{cross} provide the greatest separation between classes, while in the far range ρ_{VVHH} and γ_{co} provide the greatest separation. By combining γ_{co} (far) with either of ρ_{HHVH} or γ_{cross} (near), all ice types are independent from each other. From Figure 4.4 it is known that a lower ρ_{RRLL} is associated with a rougher ice surface.

Figure 4.5. Co- (HH and VV) and cross- (HV) polarization backscatter intensities of snow-covered first-year sea ice (SCFYI), deformed first-year sea ice (DFYI), consolidated pancake ice (PI), snow-covered frost flowers (SCFF), and dense frost flowers (DFF).

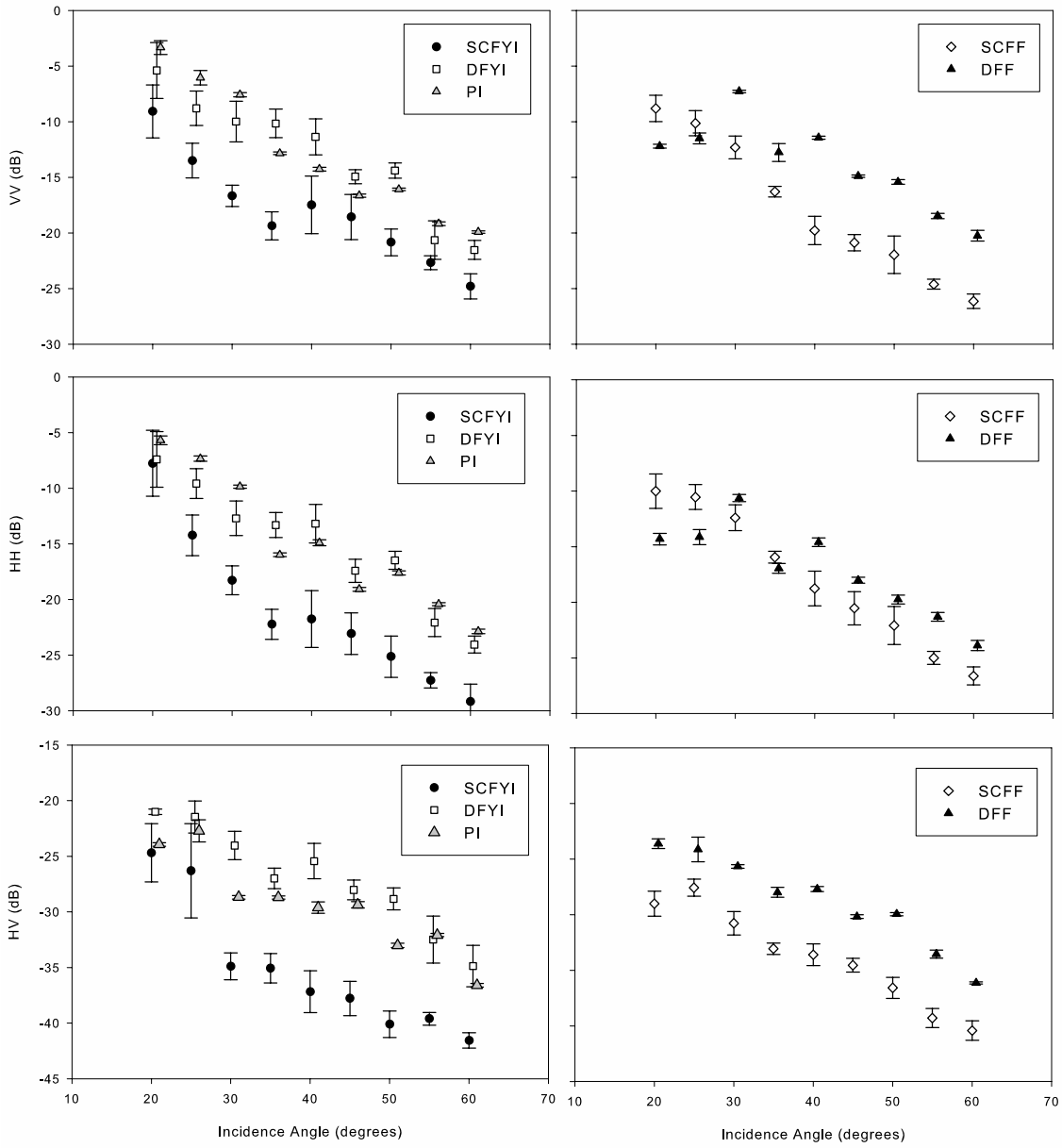

Table 4.3. Mean C-band polarimetric coherences and ratios of selected ice types, for near (N), middle (M) and far (F) range incidence angle groupings (Also shown graphically in Figure 4.6). The number of data samples is: (SCFYI, N = 14; DFYI, N = 8; PI, N = 14; SCFF, N = 18; DFF, N = 10).

		ρ_{VVHH}	ρ_{HHVH}	ρ_{RRLL}	γ_{co} (dB)	γ_{cross} (dB)
SCFYI	N	0.95	0.09	0.47	0.40	–16.44
	M	0.81	0.09	0.65	3.64	–13.72
	F	0.55	0.08	0.81	4.54	–12.25
DFYI	N	0.88	0.10	0.42	1.36	–12.38
	M	0.91	0.08	0.52	2.47	–12.94
	F	0.58	0.05	0.58	1.86	–11.40
PI	N	0.96	0.04	0.61	1.78	–16.89
	M	0.84	0.04	0.61	1.89	–13.73
	F	0.80	0.05	0.59	2.10	–12.70
SCFF	N	0.96	0.07	0.73	0.89	–17.88
	M	0.89	0.07	0.70	–0.59	–15.83
	F	0.66	0.05	0.77	0.46	–14.08
DFF	N	0.84	0.15	0.35	2.41	–09.71
	M	0.91	0.15	0.59	3.65	–12.06
	F	0.79	0.12	0.72	3.23	–12.23

It is demonstrated using theory that lower values of ρ_{RRLL} indicate a rougher ice surface. Referring to Figure 4.4 and Figure 4.6, ρ_{RRLL} is high for increasing incidence angles and for low surface roughness. This is only true for SCFYI and SCFF. In the presence of dry and fresh snow the volume contribution from FYI can be ignored, in which case ρ_{RRLL} dictates surface roughness of the snow-ice interface rather than air-snow interface. The coherence estimates are negligibly affected by the signal-to-noise

ratio (typically > 10 dB) during the processing of scatterometer data. These coherences can also be computed using polarimetric observations from space-based platforms.

4.4. Summary and Conclusions

The one-dimensional backscatter model of Schuler et al. (2002) was modified to two-dimensions of surface roughness by considering deviation in the orientation angles (i.e. the slopes) in azimuth and range direction simultaneously as an improvement in the model. Parameters derived from the fully polarimetric C-band microwave backscatter response from sea ice targets were demonstrated to have utility for small-scale (cm level) sea ice roughness identification. Circular coherence has been investigated for its usefulness in discriminating surface roughness among other polarimetric parameters. Circular coherence is theoretically shown to detect measurement sensitivity to surface roughness. The conclusions with reference to objective 1 are as follows: It was shown theoretically that the ρ_{RRLL} decreases exponentially with increasing surface roughness. However, ρ_{RRLL} responds to both roughness (standard deviation) and dielectric constant (scattering matrix) of the surface in the case when the orientations of the ice target in azimuth direction are changed. It remains challenging to separate roughness effects from the dielectric effects using C-band backscatter measurements.

ρ_{RRLL} independently does not provide a robust sea ice roughness discrimination scheme. However, ρ_{RRLL} provides an improved insight of sea ice surface roughness combined with other polarimetric coherences and channel ratios in the chosen samples. The experimental data also show that rougher ice surface exhibit lower mean value of ρ_{RRLL} (Table 4.3, Figure 4.4), though a complete validation of the effect of changing

orientations of ice floe on ρ_{RRLL} is required. This would require polarimetric backscattering data and surface roughness information to be acquired at different lines of sight (i.e. orientation of ice floes). Unfortunately, difficulties associated with extreme weather conditions and limitations to navigation in the Arctic restrict such detailed data acquisition; however, a tank experiment could be a useful alternative.

The utility of C-band polarimetric coherences and ratios is addressed in the light of objective-2 as follows: for coherences, ρ_{VVHH} is smaller at far range incidence angles for all ice types. ρ_{HHVH} is less sensitive to roughness and is not a good discriminator of roughness. Regarding channel ratios, based on Kruskal-Wallis test, γ_{co} is more sensitive to increasing surface roughness compared to γ_{cross}, and demonstrates utility for separating ice types compared to the other observed parameters.

The knowledge obtained through surface-based polarimetric coherences and ratios can readily be extended to discriminate sea ice roughness on small-scales using C-band microwave satellites (currently in orbit RADARSAT-2, RISAT-1). Future work will be to develop an algorithm combining all polarimetric coherences and ratios to discriminate individual ice type in a MIZ. These observations may become particularly useful for satellite measurements once planned SAR constellations (Sentinel series) systems are available; as currently planned with National Aeronautics and Space Administration and European Space Agency.

Table 4.4. Matrix of significance values from non-parametric Kruskal-Wallis tests for independence between ice types based on polarimetric parameters and near (N), middle (M), and far (F) range groupings. The number of data samples is: (SCFYI, N = 14; DFYI, N = 8; PI, N = 14; SCFF, N = 18; DFF, N = 10).

		Near Range					*Middle Range*					*Far Range*				
		SCFYI	DFYI	PI	SCFF	DFF	SCFYI	DFYI	PI	SCFF	DFF	SCFYI	DFYI	PI	SCFF	DFF
ρ_{VVHH}	SCFYI															
	DFYI	.285					.015					.094				
	PI	.028	.094				.509	**.000**				**.000**	**.001**			
	SCFF	.463	.119	**.002**			.011	.322	**.001**			.014	.199	**.000**		
	DFF	.004	.013	.028	**.000**		**.005**	.483	**.000**	**.000**		**.000**	**.004**	.420	**.000**	
ρ_{HHVH}	SCFYI															
	DFYI	.201					.201					.035				
	PI	**.006**	**.000**				**.005**	**.005**				.018	.221			
	SCFF	.429	**.008**	**.000**			.125	.156	.001			.046	.184	.277		
	DFF	**.002**	**.002**	**.000**	**.000**		**.001**	**.000**	**.000**	**.000**		**.001**	**.000**	**.000**	**.000**	
ρ_{RRLL}	SCFYI															
	DFYI	.308					.048					.030				
	PI	.164	.106				.082	.513				**.000**	.357			
	SCFF	**.006**	**.001**	.039			.418	**.005**	**.002**			.015	.023	**.000**		
	DFF	.023	.197	**.000**	**.000**		.069	.483	.170	**.003**		**.000**	.042	.117	**.002**	
γ_{co}	SCFYI															
	DFYI	.285					.018					**.001**				
	PI	.028	.094				**.001**	.183				**.000**	.308			
	SCFF	.463	.119	**.002**			**.000**	**.000**	**.000**			**.000**	**.001**	**.000**		
	DFF	**.004**	.013	.028	**.000**		.466	.017	**.001**	**.000**		**.000**	**.003**	**.005**	**.000**	
γ_{cross}	SCFYI															
	DFYI	**.005**					.149					.041				
	PI	.437	**.001**				.214	.357				.164	.041			
	SCFF	.118	**.000**	.179			**.006**	**.005**	**.001**			**.000**	.013	**.001**		
	DFF	**.000**	.010	**.000**	**.000**		**.004**	.204	**.006**	**.000**		.420	.042	.354	**.000**[#]	

[#] Bold numbers indicate important significant values.

Figure 4.6. Box-plots of coherences and polarization ratios of ice types based on near, middle, and far range incidence angle groupings. Significance values are provided in Table 4.4.

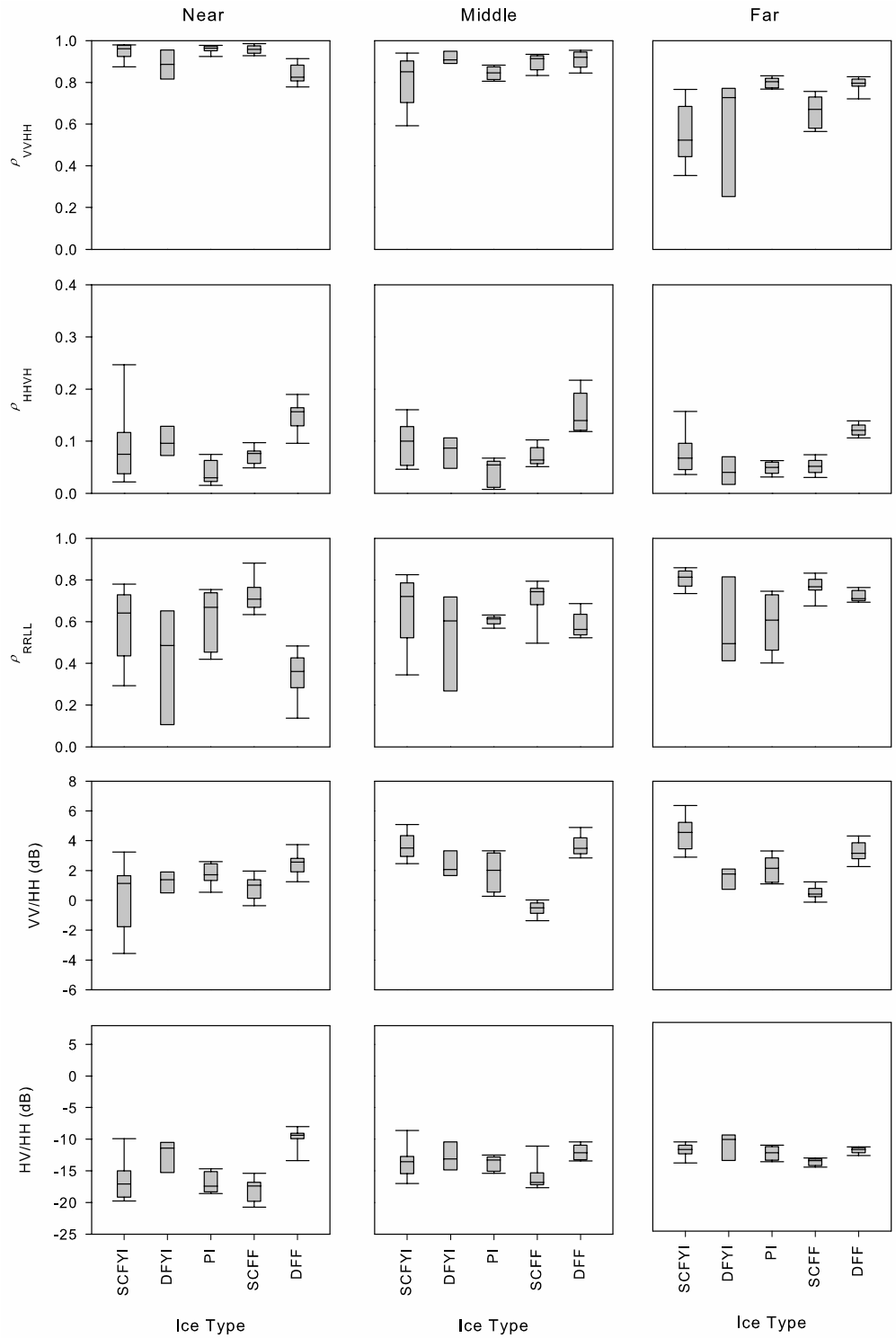

Appendix–4A: Derivation of Circular Coherence

To understand how to extract best information from the scattering matrix $\boldsymbol{S}$, it is represented by the vector, $\boldsymbol{V}$, built as follows:

$$\boldsymbol{S} = \begin{bmatrix} HH & HV \\ VH & VV \end{bmatrix};\ \boldsymbol{k} = \boldsymbol{V}(\boldsymbol{S}) = \frac{1}{2} Tr([\boldsymbol{S}]\boldsymbol{\psi}) \tag{4.A1}$$

$$\boldsymbol{k} = (k_0\ \ k_1\ \ k_2\ \ k_3)^T$$

$\boldsymbol{\psi}$ is a basis matrix, which is constructed as an orthonormal set under the Hermitian inner product. The polarimetric coherency matrix is based on linear combinations arising from Pauli matrices (Cloude and Pottier, 1996) given as,

$$\boldsymbol{\psi} \equiv \sqrt{2}\begin{bmatrix} 1 & 0 \\ 0 & 1 \end{bmatrix} \sqrt{2}\begin{bmatrix} 1 & 0 \\ 0 & -1 \end{bmatrix} \sqrt{2}\begin{bmatrix} 0 & 1 \\ 1 & 0 \end{bmatrix} \sqrt{2}\begin{bmatrix} 0 & -i \\ i & 0 \end{bmatrix} \tag{4.A2}$$

The factor of $\sqrt{2}$ arises from the requirement to keep $Tr([\boldsymbol{S}])$, the total power scattered, an invariant. The target vector in above base is constructed as,

$$\boldsymbol{k} = \frac{1}{\sqrt{2}}[(S_{HH} + S_{VV})\ \ (S_{HH} - S_{VV})\ \ (S_{HV} + S_{VH})\ \ i(S_{HV} - S_{VH})]^T \tag{4.A3}$$

From the vector form of scattering matrix, Pauli coherency matrix is generated from the outer product of the vector with its conjugate transpose as,

$$\boldsymbol{T}_4 = \langle \boldsymbol{k}.\boldsymbol{k}^{*\boldsymbol{T}} \rangle \tag{4.A4}$$

For reciprocal target matrix (as in monostatic backscattering), $S_{HV} = S_{VH}$, the four-dimensional polarimetric coherency matrix reduces to three-dimensional polarimetric coherency matrix is obtained as,

$$\boldsymbol{T}_3 = \begin{bmatrix} \langle |S_{HH} + S_{VV}|^2 \rangle & \langle (S_{HH} + S_{VV})\,(S_{HH} - S_{VV})^* \rangle & 2\langle (S_{HH} + S_{VV}) S_{HV}^* \rangle \\ \langle (S_{HH} - S_{VV})(S_{HH} + S_{VV})^* \rangle & \langle |S_{HH} - S_{VV}|^2 \rangle & 2\langle (S_{HH} - S_{VV}) S_{HV}^* \rangle \\ 2\langle S_{HV}(S_{HH} + S_{VV})^* \rangle & 2\langle S_{HV}(S_{HH} - S_{VV})^* \rangle & 4\langle |S_{HV}|^2 \rangle \end{bmatrix} \tag{4.A5}$$

The ρ_{RRLL} is computed as (Cloude and Pottier, 1996; Lee et al., 2002),

$$\rho_{\mathrm{RRLL}} = \frac{T_{22} - T_{33}}{T_{22} + T_{33}} = \frac{\langle |S_{HH} - S_{VV}|^2 \rangle - 4\langle |S_{HV}|^2 \rangle}{\langle |S_{HH} - S_{VV}|^2 \rangle + 4\langle |S_{HV}|^2 \rangle} \tag{4.A6}$$

T_{ij} represents the (i, j) element of the matrix, T_3 given in Eq. (4.A5). For the one-dimensional polarimetric scattering model described elsewhere (Hajnsek et al., 2003; Schuler et al., 2002), ρ_{RRLL} is expressed as independent of dielectrics, thus depending only on surface roughness. Fore more detailed, step by step derivation of ρ_{RRLL}, the reader is directed to (Cloude and Pottier, 1996; Hajnsek et al., 2003; Lee et al., 2002).

Appendix–4B: Relationship Between Slope and Various Angles

Here, the relationship between slope in azimuth and ground range, radar look angle, shift in azimuth, and shift in ground range is derived. The slope equation given by Lee et al. (2000) does not include shift in range direction. Figure 4.3 shows the geometry of backscattering plane. Suppose that the backscattering plane is shifted in azimuth direction by angle θ_1 and in range direction by angle θ_2. $\hat{\mathbf{n}}$ represents the surface normal on the backscattering plane before rotating.

$$\hat{\mathbf{n}} = n_1\hat{\mathbf{x}} + n_2\hat{\mathbf{y}} + n_3\hat{\mathbf{z}}. \tag{4.B1}$$

$$\hat{\mathbf{N}} = \begin{bmatrix} 0 & -\sin\phi & \cos\phi \\ 1 & 0 & 0 \\ 0 & \cos\phi & \sin\phi \end{bmatrix} \begin{bmatrix} n_1 \\ n_2 \\ n_3 \end{bmatrix}$$

$$= \begin{bmatrix} -n_2\sin\phi + n_3\cos\phi \\ n_1 \\ n_2\cos\phi + n_3\sin\phi \end{bmatrix}. \tag{4.B2}$$

The surface normal changes after a shift in azimuth and range directions in introduced. The transformed normal is

$$\hat{\mathbf{n}}(\theta_1, \theta_2) = \begin{bmatrix} 1 & 0 & 0 \\ 0 & \cos\theta_1 & \sin\theta_1 \\ 0 & -\sin\theta_1 & \cos\theta_1 \end{bmatrix} \begin{bmatrix} \cos\theta_2 & 0 & -\sin\theta_2 \\ 0 & 1 & 0 \\ \sin\theta_2 & 0 & \cos\theta_2 \end{bmatrix} \hat{\mathbf{N}}. \tag{4.B3}$$

If $\cos\theta_1 = c_1$ and $\sin\theta_2 = s_2$, and substitute $\hat{\mathbf{N}}$ from (4.B2), then (4.B3) is,

$$= \begin{bmatrix} -c_2(n_2 \sin\phi + n_3 \cos\phi) - s_2(n_2 \cos\phi + n_3 \sin\phi) \\ s_1 s_2(-n_2 \sin\phi + n_3 \cos\phi) + n_1 c_1 + s_1 c_2(n_2 \cos\phi + n_3 \sin\phi) \\ c_1 s_2(-n_2 \sin\phi + n_3 \cos\phi) - n_1 s_1 + c_1 c_2(n_2 \cos\phi + n_3 \sin\phi) \end{bmatrix}. \quad (4.B4)$$

After the rotation the surface normal is in new plane where the second component must be zero.

$$s_1 s_2(-n_2 \sin\phi + n_3 \cos\phi) + n_1 c_1 + s_1 c_2(n_2 \cos\phi + n_3 \sin\phi) = 0 \quad (4.B5)$$

With range slope, $\tan\gamma = -(n_2/n_3)$ and azimuth slope $\tan\omega = -(n_1/n_3)$,

$$\frac{\tan\omega}{\tan\theta_1} = \sin\theta_2(\tan\gamma.\sin\phi + \cos\phi) + \cos\theta_2(-\tan\gamma.\cos\phi + \sin\phi). \quad (4.B6)$$

In (4.B6), if the perturbation in orientation in range direction is zero, i.e. $\theta_2 = 0$, it reduces to equation given by Lee et al. (2000).

Chapter 5

Microwave Emission and Scattering from Ocean Surface Waves in the Southern Beaufort Sea

Mukesh Gupta[1*], Randall K. Scharien[1, 2], and David G. Barber[1]

International Journal of Oceanography, vol. 2014, Article ID 872342, 1–12,

doi:10.1155/2014/872342

[1]Centre for Earth Observation Science, Department of Environment and Geography, Clayton H. Riddell Faculty of Environment, Earth and Resources, University of Manitoba, 463, Wallace Building, Winnipeg R3T 2N2, Manitoba, Canada

[2]Now at: Department of Geography, University of Victoria, Victoria V8W 2Y2, British Columbia, Canada

[*]Corresponding Author

Abstract

Estimates of the relationships between geophysical variables and microwave backscatter/emission are important for the evaluation of atmosphere-ocean interaction, as well as energy and mass transfer across this interface. Ship-based passive microwave brightness temperatures (T_b) at 37 and 89 GHz, and polarimetric active backscatter at 5.5 GHz (C-band), in relation to buoy-derived ocean wave parameters for distinct wave regimes in the Beaufort Sea, are evaluated. Microwave emission and backscatter are shown to be more sensitive to the ocean surface physical roughness as defined by the significant wave height (H_{m0}), compared to wind speed. The T_b is significantly correlated with H_{m0}, with the strongest correlation for the H-polarization channel at 37 and 89 GHz. Active co- (γ_{co}) and cross- (γ_{cross}) polarization ratios at 40° incidence angle are associated with H_{m0}, with the γ_{co} increase proportional to H_{m0}. The polarimetric coherence parameter ρ_{VVHH} at 20° also shows an inverse relationship with H_{m0} due to an expected decorrelation of complex returns with greater surface roughness.

5.1. Introduction

Southern Beaufort Sea experiences dynamic seasonal ocean-sea ice-atmosphere interaction (Barber and Hanesiak, 2004; Lukovich and Barber, 2005), and the seasonal formation of flaw leads and polynyas (Carmack and Macdonald, 2002; Smith and Barber, 2007). Microwave remote sensing has played a key role in investigations, with the passive and active microwave signatures from the ocean surface having been studied for several decades. Numerous geophysical parameters are now estimated with sufficient accuracy using microwave remote sensing data collected using satellite sensors. However, relationships between surface waves and radiative transfer across the atmosphere-ocean (AO) interface are, as yet, not fully realized in the literature.

Ocean surface waves modify AO interaction and concurrently affect observed passive microwave brightness temperatures (T_b) and radar returns (hereinafter backscatter). Enhanced surface roughness from wind-generated surface waves significantly affects the formation and evolution of the oceanic boundary layer (He and Chen, 2011), which in turn augments frictional drag at the surface thereby heightening the potential for forced convection (Esau, 2007). Thus, surface roughness and boundary layer turbulence create a feedback mechanism, which transfer heat and momentum across AO interface. Though the transfer of wind energy to ocean surface waves (aerodynamic roughness) is well understood, the microwave behavior of related geophysical variables such as significant wave height (H_{m0}) (hereinafter 'wave height'), power spectral density (PSD), ocean surface temperature, and near-surface water vapor are the subject of further study. The backscatter and T_b observations of open water represent composite signals that contain contributions from the full suite of these variables. In accordance, the application of

electromagnetic (EM) signatures towards geophysical inversion algorithms first demands consideration of the full suite of variables.

Previous research into AO surface roughness from both passive and active microwave remote sensing identifies considerable gaps in understanding the EM response to roughness elements (e.g., whitecaps, sea spray, and wave RMS (root-mean-square) height and correlation length). Polarimetric passive microwave signatures of the ocean surface at frequencies 10.7, 19.35, and 37 GHz are well-modeled by a two-scale polarimetric emission model (Germain et al., 2002; Yueh, 1997), however, the assimilation of effects of wind direction, wind-generated waves, atmospheric stability, and sea foam into polarimetric emission models of ocean surface are topics requiring further research. Observed, frequency-dependent, T_b is significantly affected by the undulations of the ocean surface and is dependent on the wind-induced wave structure, i.e. the sea state, and foam coverage (Hollinger, 1971; Ulaby, 1986). Kravtsov and Churyumov (2000) mathematically described the effect of steep irregularities and wave slope on the T_b. Inclusion of additional parameters of whitecaps and foam was suggested in the retrieval algorithms using satellite remote sensing (Monahan and O'Muircheartaigh, 1986). Wave height can also be linked to T_b as a close function of surface wind speed (Strong, 1971). Nordberg et al. (1971) provided the measurements of microwave emission at 19 GHz from a foam-covered and wind-driven sea. In all above-mentioned surface conditions, the T_b is observed to be increasing with an increase in foam coverage and whitecaps.

Microwave C-band (5.5 GHz, 5.6 cm wavelength) backscatter is more reliable for studying surface waves than shorter wavelength Ku-, Ka-, and X-bands that are strongly influenced by capillarity and molecular viscosity (water temperature) (Phillips, 1988;

Vandermark et al., 2004). There are numerous studies readily found on relationships between C-band co-polarization backscatter (HH and VV) and wind speed and direction, with geophysical model transfer functions (e.g., CMOD) widely used to retrieve wind information from backscatter (Stoffelen and Anderson, 1997; Hersbach et al., 2007; Hersbach, 2010; Komarov et al., 2014). A power law relationship holds for backscatter and friction velocity (Jones and Schroeder, 1978), and also between backscatter and wind speed (Keller et al., 1989). Keller et al. (1989) also observed backscatter increasing with decreasing AO temperature difference. Thompson et al. (1998) found that the observed co-polarization ratio is larger than predicted by backscatter models, as these models inadequately address the non-linearity of the long-wave portion of a rough ocean surface. Thompson et al. (1998) provided an incidence angle dependent polarization ratio model that was extended by Mouche et al. (2005) to include wind speed, wind direction, sea state, and swell effects. The results of Mouche et al. (2005) show that the co-polarization ratio (γ_{co}) is dependent more on wave steepness than on wave height and wind speed.

At C-band, the waves under rough conditions are typically 3–10 times larger than the incident radar wavelength (Kudryavtsev et al., 2003a, 2003b). Kudryavtsev et al. (2003a) suggested a composite backscatter model for describing backscatter (at moderate incidence angles 20°–60°) from ocean surface waves, which included non-Bragg scattering components caused by breaking waves (wavelength from few millimeters to few meters) based on wave breaking statistics proposed by Phillips (1985). The γ_{co} can be used to study the discrepancy between the Bragg model and observations and it can explain non-Bragg component of scattering (Kudryavtsev et al., 2003a). Valenzuela (1978) provided a review of the theories addressing EM wave interaction with small

gravity-capillary waves, citing Bragg (resonant) scattering as the most important mechanism of ocean surface–EM interaction. Energy dissipation over different length scales and breaking wave mechanisms are largely linked to non-Bragg scattering, though their effects on backscatter are less understood. The H_{m0} and wave PSD measured from a buoy are investigated here, which contain contributions from the non-Bragg scattering elements, using the cross-polarization channel ratio (γ_{cross}) and polarimetric coherence parameters, in addition to γ_{co}.

This paper addresses open ocean surface waves (physical roughness) during the ice-free season, with the overarching objective to further our understanding of the role of T_b and backscatter in estimating ocean surface waves and, by proxy, AO exchanges. We examine near surface (ship-based) passive microwave T_b (37 and 89 GHz) and polarimetric C-band backscatter, as these relate to buoy measurements of H_{m0} and PSD. This comparison is rarely available in the literature. The utility of γ_{co}, and γ_{cross}, as well as polarimetric coherences from the ocean surface, is investigated to contribute to the realization of polarimetric synthetic aperture radar (Pol-SAR) for deriving ocean surface wave information.

5.2. Materials and Methods

5.2.1. Study Area

The study area was located in Amundsen Gulf in the southern Beaufort Sea (Figure 5.1). The Cape Bathurst Polynya forms in the area and hosts a number of flaw leads throughout the winter (Barber and Hanesiak, 2004) and the region becomes relatively ice-

free in the summer. Field data were acquired between 1 and 28 July 2008 as part of the Circumpolar Flaw Lead (CFL) System Study, an International Polar Year (IPY) project that took place between October 2007 and August 2008 aboard the Canadian Research Icebreaker *Amundsen* (Barber et al., 2010).

Figure 5.1. Study area showing DWR-G4 buoy and EM sampling locations.

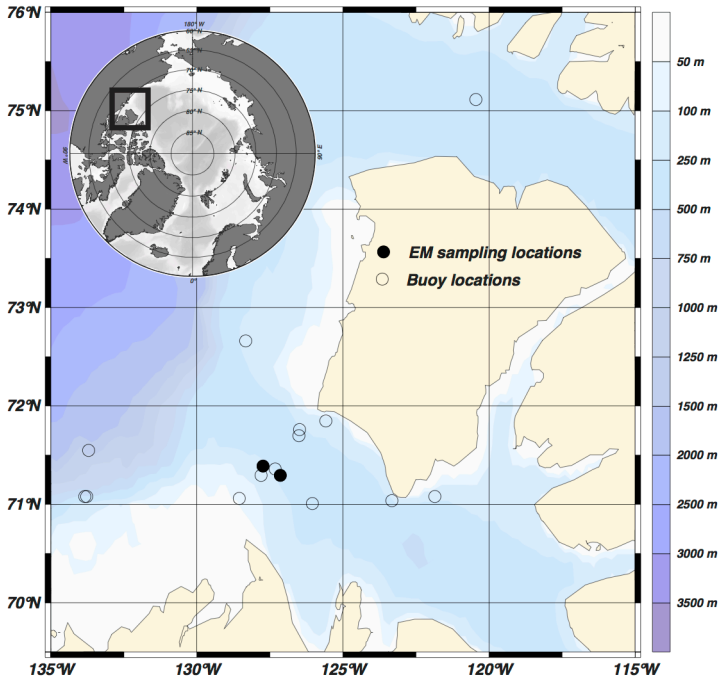

5.2.2. Instruments' Description and Data Collection

Ocean wave height, wave steepness, wave period, and wave phase speed were acquired using a meteorological ocean (Datawell®, Haarlem, The Netherlands) Mini Directional Waverider G4 (DWR-G4) buoy. The buoy has a hull diameter of 0.4 m and weight in air of 17 kg. The buoy is capable of measuring wave height and direction for periods of 1.6–100 s and covers the expected range of wave periods observed in the Arctic (~60 s, see, e.g., Hunkins, 1962). Wave height accuracy is 1 cm in all directions while freely

floating. H_{m0} was computed from the zeroth moment of the wave spectrum. The PSD is computed from the Fourier spectra of the vertical displacements. The PSD shows what wave amplitudes occur at what frequencies. The accuracy of wave PSD, wavelength, and other derived wave parameters rely on wave height accuracy. In order to avoid interference by the *Amundsen*, the buoy was deployed by small boat at a minimum distance of 200 m from the ship. Wave data were logged at 30 minutes intervals from a stabilized accelerometer. Continuous meteorological data were collected at one-minute interval from a tower mounted on the bow of the *Amundsen*. Wind speed (U) data at 14 m above sea level (ASL) were collected using an RM-Young model 5103 Wind Monitor at an accuracy of ±0.3 m/s or 1% of the reading. Water temperature at the sea surface was acquired from the *Amundsen's* AXYS Automated Voluntary Observing Ship (AVOS) sensors with a resolution of 0.1ºC and an accuracy of ±0.3ºC.

Ship-based dual-polarized (H and V) passive microwave (Radiometrics®, Boulder, CO, USA) radiometers operating at 37 and 89 GHz frequencies were used to acquire emissions from the ocean surface at a fixed incidence angle of 53°, the same incidence angle as the spaceborne SSM/I (Special Sensor Microwave/Imager) sensor and within 2° of the spaceborne AMSR-E (Advanced Microwave Scanning Radiometer – Earth Observing System) sensor. The system was installed on the rail mount on the port side of the *Amundsen* at approximately 12 m ASL. Recorded voltages were converted to T_b by the calibration method described by Farmer et al. (1990). The T_b data were acquired for 24-hour full cycle for all days and were averaged for every 30 minutes for the specified dates during the month of July 2008 at the locations shown in Figure 5.1. T_b data were matched with buoy data over 2–7 hours duration for comparison in this study. The

relationships of H_{m0} and PSD, and ship-based T_b at meter scales (footprint at 89 GHz at 55°: 6.36 m^2; at 37 GHz: 6.62 m^2) at 0.81 cm (37 GHz) and 0.34 cm (89 GHz) wavelengths are presented in this paper.

Table 5.1. Technical properties and specifications of C-band scatterometer used.

System Parameter	Value
RF output	5.25–5.75 GHz
Antenna diameter	0.61 m
Transmit bandwidth	5–500 MHz, user adjustable
Range resolution	0.3–30.0 meters, user adjustable
Antenna beamwidth	H-pol: 5.2° azimuth, 5.5° elevation V-pol: 5.6° azimuth, 5.3° elevation
Antenna gain	28 dB, nominal
Cross-polarization isolation	> 30 dB, measured at the peak of the beam
Transmit/receive polarizations	Linear, Vertical and Horizontal
Sensitivity, minimum NRCS at 15 m range	–40 dB m^2/m^2
Chirp length	Variable, 0.1–15.0 ms

Note: NRCS: Normalized Radar Cross-Section; RF: Radio Frequency

A C-band fully polarimetric scatterometer (ProSensing Inc., Amherst, MA, USA) (Table 5.1) installed on the port side of the *Amundsen* at a height of 7.6 m ASL was used to collect backscatter signatures coincident to ocean buoy data over relatively short (< 0.5 hour) periods on 1, 9, and 26 July. Backscatter and phase data at all four linear transmit/receive polarization combinations (HH, HV, VH, and VV) were collected over

the 20°–60° incidence angle range at 10° spacing, and across a 60° azimuth centered perpendicular to the *Amundsen*. At 7.6 m height, and with the scatterometer positioned at a fixed azimuth and 45° incidence angle, its footprint was estimated to be 1.1 m^2. By extending the azimuth to a 60° range, a single scan comprised several footprints over several meters, resulting in multiple statistically independent samples of the sea surface at each incidence angle. The use of a wide azimuth also increased the number of radar looks and reduced fading, though the resulting experimental dataset does not consider the wave direction relative to the scanning scatterometer. Instrument calibration, noise levels, set up, and data limitations are described elsewhere (Geldsetzer et al., 2007; Isleifson et al., 2010).

For analysis of scatterometer data a limit of 3 dB of signal-to-noise ratio was placed on backscatter, resulting in an upper incidence angle limit of 40° for scans taken during relatively calm conditions. This limit was extended to all samples to enable the inter-comparison of all backscatter regardless of sea state. Scan data were represented by the average covariance matrix, from which HH, HV, and VV backscatter, as well as γ_{co} and γ_{cross}, were derived from backscatter amplitudes. The following polarimetric coherence parameters: the co-polarized correlation coefficient (ρ_{VVHH}); the cross-polarized correlation coefficient (ρ_{HHVH}) ; and the coherence of right and left circular transmit/receive polarizations (ρ_{RRLL}) were obtained using the formulae in Eq. (5.1)–(5.3) following (Gupta et al., 2013; Lee et al., 2000; Schuler et al., 2002),

$$\rho_{\mathrm{VVHH}} = \frac{\langle |S_{\mathrm{VV}} S_{\mathrm{HH}}^{*}| \rangle}{\sqrt{\langle |S_{\mathrm{VV}}|^2 \rangle \langle |S_{\mathrm{HH}}|^2 \rangle}}, \tag{5.1}$$

$$\rho_{\mathrm{HHVH}} = \frac{\langle |S_{\mathrm{HH}} S_{\mathrm{VH}}^{*}| \rangle}{\sqrt{\langle |S_{\mathrm{HH}}|^2 \rangle \langle |S_{\mathrm{VH}}|^2 \rangle}}, \tag{5.2}$$

$$\rho_{\mathrm{RRLL}} = \frac{\langle |S_{\mathrm{HH}} - S_{\mathrm{VV}}|^2 \rangle - 4\langle |S_{\mathrm{HV}}|^2 \rangle}{\langle |S_{\mathrm{HH}} - S_{\mathrm{VV}}|^2 \rangle + 4\langle |S_{\mathrm{HV}}|^2 \rangle}, \tag{5.3}$$

$$\gamma_{\mathrm{co}} = \frac{S_{\mathrm{VV}}}{S_{\mathrm{HH}}}, \tag{5.4}$$

$$\gamma_{\mathrm{cross}} = \frac{S_{\mathrm{HV}}}{S_{\mathrm{HH}}}. \tag{5.5}$$

where S is the complex scattering matrix; and an asterisk (*) represents the complex conjugate. The brackets $\langle . \rangle$ represent ensemble averages of the observed data. Polarimetric coherences and polarization ratios have demonstrated utility in reducing the ambiguities caused by the non-linearity between system response and target properties (Eom and Boerner, 1991). Further details on the derivation of ρ_{RRLL}, a parameter shown to be sensitive to surface roughness, are found in (Hajnsek et al., 2003; Mattia et al., 1997).

5.3. Results and Discussion

5.3.1. Ocean Surface Wave Conditions

The data primarily represent wave breaking and energy dissipation due to waves depending on the prevailing wind conditions. From the measured buoy data H_{m0} ranged between 12–214 cm (sea state on Beaufort scale 0–5) compared to those by Hwang et al. (2008) who reported a range 120–270 cm in the Atlantic Ocean (Figure 5.2). Observed

wave numbers ranged between 0.083–0.729 rad/m, and wind speeds ranged between 0.5–10.5 m/s compared to wind speed range of 7.0–14.5 m/s given by Hwang et al. (2008). In this study, the wave steepness ranged between 0.011–0.050, which corresponded with ocean surface wavelength ranging between 8.61–75.56 m. The wave periods of wind-generated waves addressed in this paper lie between 2.4–7.0 s.

Figure 5.2. (a) Significant wave height (H_{m0}) observed from 1–28 July 2008 (total number of samples = 103). Multiple measurements on a day fall on the same vertical line. (b) H_{m0} is plotted versus wind speed and compared with data (total number of samples = 29) from Hwang et al. (2008).

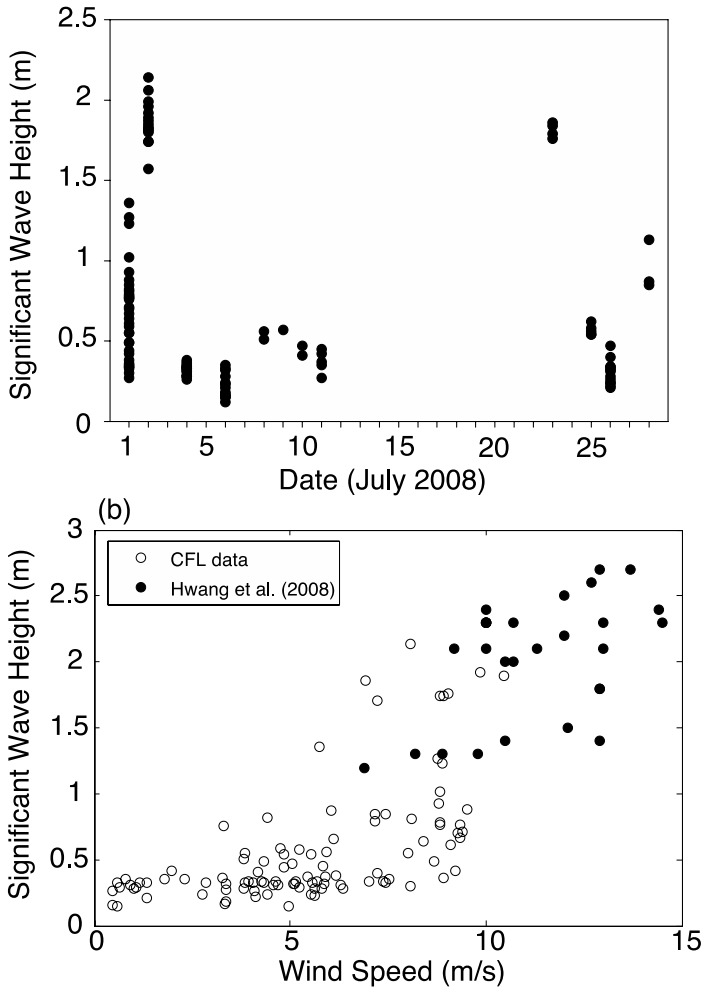

Swells [wave period > 10 s (Wells, 2012)] were not observed during the field program. Wind-generated wave growth in the data is well supported by the observed relationship between the non-dimensional form of energy, $\frac{g^2 \mathrm{H_{m0}}}{\mathrm{U^4}}$ (where g is gravitational acceleration), and wave age, $\frac{\mathrm{U}}{c_p}$ (where c_p is wave phase speed) as initially proposed by Kitaigorodskii (1962) and further developed by Donelan et al. (1992) (Figure 5.3). The RMS error in the fitted curve is 0.024; the coefficient of determination, $\mathrm{R^2} = 0.97$; and sum of residual errors, SSE = 0.052. The observed empirical relationship is:

$$\frac{g^2 \mathrm{H_{m0}}}{\mathrm{U^4}} = 0.00817 \left(\frac{\mathrm{U}}{c_p}\right)^{-3.132}. \tag{5.6}$$

Figure 5.3. Wind-generated wave condition in the experiment is shown here. Nonlinear model $y = \mathrm{a}x^b$ between non-dimensional wave energy (y-axis) and wave age (x-axis) indicating wind-induced wave development. SSE is the sum of squared error of the fit.

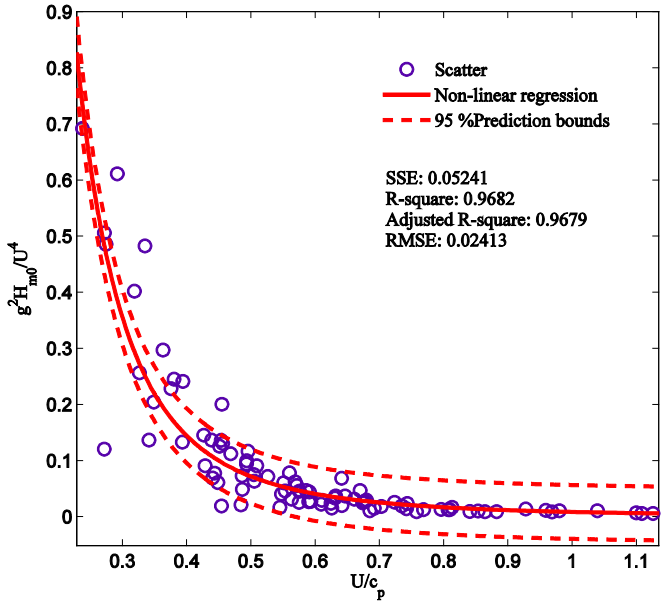

Wave roughness parameters H_{m0} and PSD, coincident to scatterometer acquisitions on 1, 9, and 26 July, are shown along with U in Table 5.2. While the scatterometer took eight minutes to complete one scan, wave height and PSD data were logged at 30 minutes intervals.

Table 5.2. Scatterometer measurement dates and times, sampling durations, near and far range numbers of independent samples (n_{ind}) of the sea surface, with coincident wind speed and wave roughness parameters, significant wave height (H_{m0}) and power spectral density (PSD).

Date (2008)	Time (UTC)	Duration (minutes)	Radar n_{ind} (Near: 20°)	Radar n_{ind} (Far: 40°)	Wind Speed (m/s)	Wave PSD (m^2/Hz)	Wave H_{m0} (cm)
1 July	18:37	14	44	122	7.4	4.3154	136
9 July	16:57	17	44	122	5.8	0.2787	66
26 July	17:49	24	66	198	3.9	0.4617	47

Note: UTC: Universal Time Coordinated

Table 5.2 also provides the number of independent scatterometer samples acquired at 20° (near range) and 40° (far range) incidence angles examined in this study. Wave spectra from the same dates are shown relative to the analytical Pierson-Moskowitz (P-M), Bretschneider, and 3-parameter Gamma wave spectra (Figure 5.4). These wave spectra considered both capillary and gravity wave (wavelength > 1.74 cm) development. The observed spectra are in agreement with the modeled spectra (integration time 3 hours with frequencies 0–0.33 Hz; Moskowitz, 1964) for the H_{m0} case on 9 July, with peak frequencies of ~0.2 Hz. For other high and low H_{m0} cases, the observed spectra agree more closely with the P-M model at wave frequencies greater than 0.2 Hz. The high and

low H_{m0} cases also contain considerably more observed wave energy in the low frequency part of the observed spectra, indicating the presence of longer waves (Figure 5.4a, c).

Figure 5.4. Wave spectra measured coincident to scatterometer on 1 July, 9 July, and 26 July 2008 with comparisons to analytical spectra. *Red*: measured; *Green*: Pierson-Moskowitz; *Blue*: Bretschneider; *Magenta*: 3-parameter Gamma.

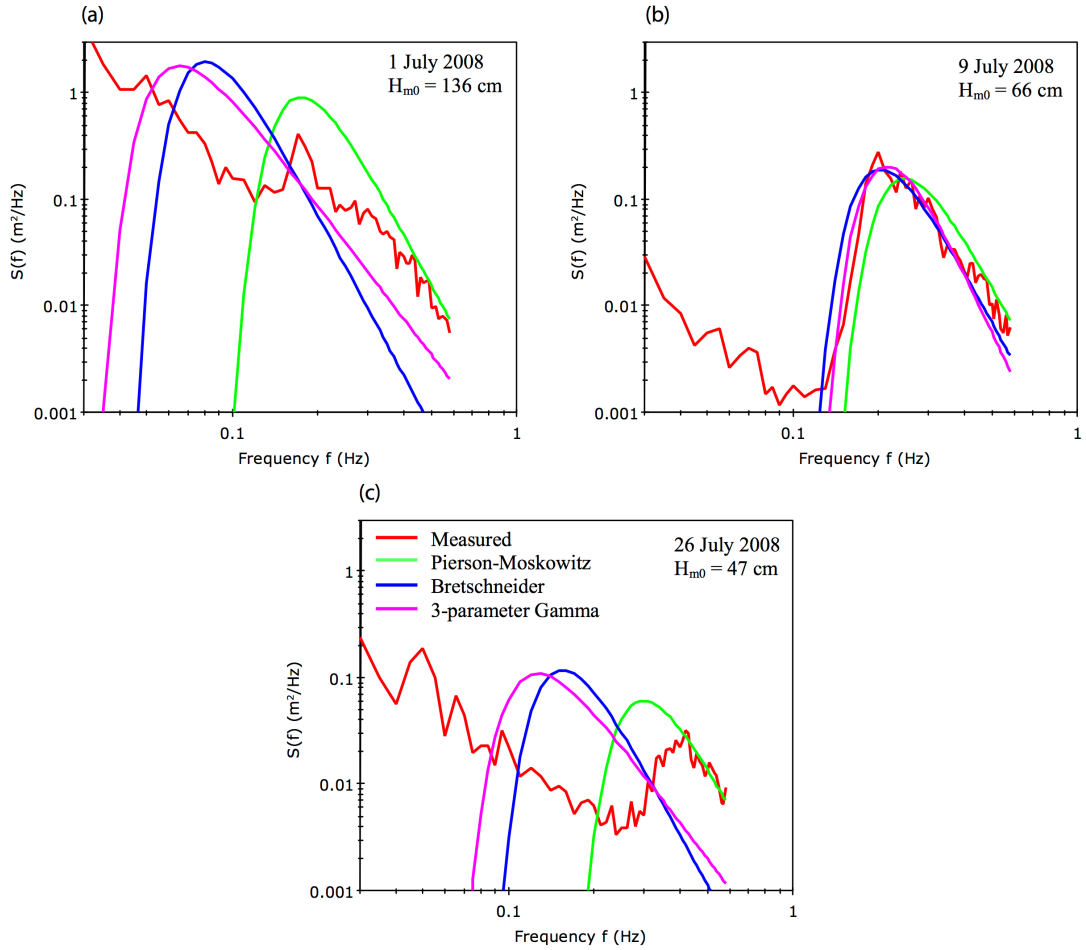

The low frequency part of the spectra is marginally modeled by the wave spectra models, likely due to insufficient number of statistical data points of long wavelength waves available to generate a spectrum that fits the analytical spectrum. Also, the data

lacked swell observations during the field campaign, and did not contain considerable wave frequencies < 0.2 Hz. Therefore, in the present treatment, the wave frequencies 0.2 Hz and above have only been considered. The high H_{m0} at low wind speeds indicates that the wave energy still retained in the ocean even after winds have subsided. This transition from calm to rough sea (and vice versa) depends on the rate of wave energy dissipation in the ocean [Figure 5.2(b) and Figure 5.4]. These observed wave conditions set the background for which microwave signatures of ocean surface will be investigated in the next section.

5.3.2. Comparison to Passive and Active Microwave Signatures

Linear associations between geophysical variables (H_{m0}, PSD, water temperature, and U) and T_b at 37 and 89 GHz are shown as a correlation matrix in Table 5.3. A low probability value, *P*-value ($P < 0.05$) is observed for each combination of bolded variables given in Table 5.3, verifying statistical significance. Regression coefficients for estimating the H_{m0} using T_b are given in Table 5.4 and pertinent regression relationships are shown in Figure 5.5. Wind speed is not correlated with T_b; however, it is observed that T_b at 37 GHz and 89 GHz is significantly correlated with the H_{m0} and the PSD of the waves and the correlation is stronger for H-polarization than V-polarization because horizontally polarized EM waves interact more efficiently with the vertical features than vertically polarized EM waves. Thus, the higher T_b H-polarization implies an indirect contribution of wind energy in inducing wave heights than V-polarization. Linear relationships between water surface temperature and T_b are not observed. In addition to

this, the T_b is also affected by a number of other external factors that alter the passive microwave emission of the ocean surface such as sea spray and foam.

Table 5.3. Correlation matrix (Pearson's *r*) of observed variables. The number of samples of each variable is 111.

	T_b89H	T_b89V	T_b37H	T_b37V	H_{m0}	PSD	T_w	U
T_b89H	1							
T_b89V	**0.93**	1						
T_b37H	**0.97**	**0.88**	1					
T_b37V	**0.85**	**0.91**	**0.87**	1				
H_{m0}	**0.80**	**0.72**	**0.78**	0.55	1			
PSD	**0.71**	**0.64**	**0.70**	0.52	**0.92**	1		
T_w	0.25	0.44	0.16	0.21	0.25	0.20	1	
U	0.06	–0.02	0.09	–0.08	0.24	0.21	0.09	1

Note: T_b89H: Brightness temperature at 89 GHz H-polarization (K).
T_b89V: Brightness temperature at 89 GHz V-polarization (K).
T_b37H: Brightness temperature at 37 GHz H-polarization (K).
T_b37V: Brightness temperature at 37 GHz V-polarization (K).
H_{m0}: Significant wave height (cm).
PSD: Wave power spectral density (m^2/Hz).
T_w: Water temperature (°C).
U: Wind speed (m/s).
Numerals in bold represent statistically significant correlation at the 95% confidence level.

Table 5.4. Regression coefficients for H_{m0} and T_b for various frequencies and polarizations. The fitted line is $T_b = a + bH_{m0}$. Each regression contained 124 samples. For each frequency and polarization, the linear regression is found to be statistically significant, with horizontal polarization of 89 GHz being very well correlated with H_{m0}.

	a	b	*P*-value (95% confidence interval)	Lower, Upper bounds for	Pearson's *r*
89H	173.98	0.15	< 0.001	0.13, 0.18	0.74
89V	240.00	0.04	< 0.001	0.03, 0.05	0.65
37H	120.60	0.10	< 0.001	0.08, 0.12	0.74
37V	201.51	0.03	< 0.001	0.02, 0.03	0.51

The passive microwave frequencies used in the study are sensitive to the individual contributions of small-scale features, e.g., sea spray and whitecaps. Although the T_b depends on several other external factors (see Introduction), an increase in the surface area exposed to the sensor also contributes to a rise in T_b (Figure 5.5). Higher waves have a larger surface area, and the associated rise in T_b is especially detected at H-polarization. T_b increases with wind speed, foam and whitecaps coverage at 8.36 and 19.34 GHz frequencies (Hollinger, 1970, 1971) and between 13.4 and 37 GHz (Stogryn, 1972). However, at the observed Beaufort scale 0–5, sea sprays have been assumed non-significant, thus the contribution of spray in modifying the T_b is assumed negligible. An increase in H-polarization T_b at 37 and 89 GHz frequencies is observed, which is consistent with the H-polarization observed by previous researchers. Other results illustrate a non-significant correlation between T_b and wind speed at V-polarizations of 6.6, 10.69, and 37 GHz frequencies (Pandey and Kakar, 1982). In continuation of above studies, our results further confirm that the T_b at H-polarization is stronger than T_b at V-polarization at 37 and 89 GHz under rougher conditions.

Figure 5.5. Relationship between brightness temperature (T_b) and H_{m0} at 37 and 89 GHz frequencies and horizontal (H) and vertical (V) polarizations.

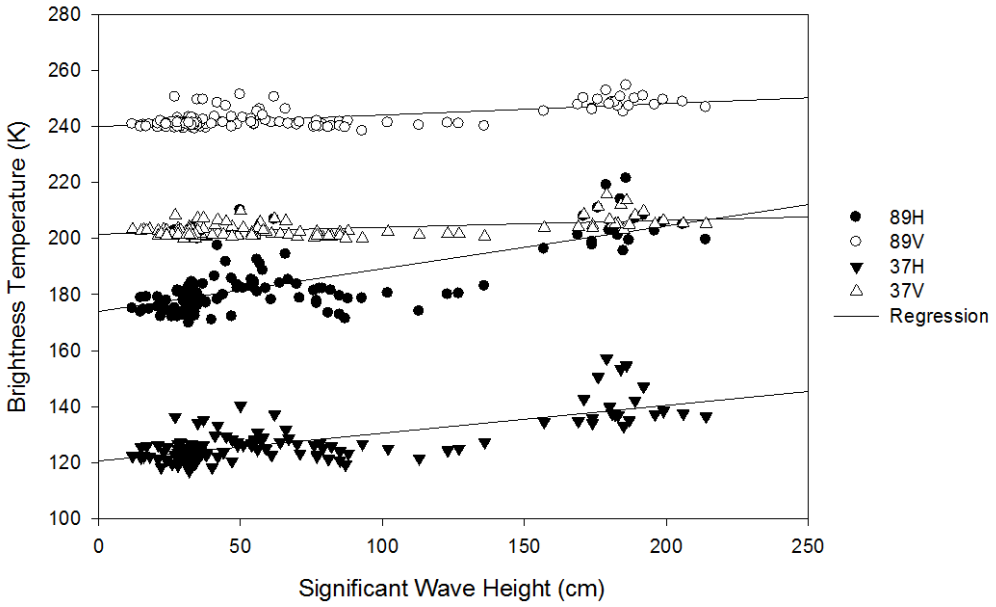

Backscatter is compared to H_{m0} and also considered in the context of surface roughness at the C-band wavelength (5.6 cm) (Figure 5.6). The observed backscatter correspond well with the three cases of observed wave heights. The interaction of incident radar waves with capillary waves (millimeter level), whose restoring force is the surface tension of the water, is not accounted for, as the waves of this size are not detectable by the buoy. A decrease backscatter (HV and VV) with increasing incidence angle is observed, as expected, over the sampled range (Figure 5.6). The highest backscatter corresponds to the highest H_{m0} on 1 July, though the weakest backscatter corresponds to the intermediate H_{m0} on 9 July (Figure 5.6). Stronger HH (not shown), HV, and VV backscatter at all incidence angles for the lowest H_{m0} on 26 July, relative to 9 July, point to the likelihood of a stronger coupling of the radar waves to capillary waves,

implying that higher capillary waves interaction with microwaves results in higher backscatter even at intermediate H_{m0}. Now, we compare the backscatter with the gravity waves, whose restoring force is gravity and are also measured by the buoy. Kudryavtsev (1997) has described the relationship between gravity (demonstrated as wave height) and capillary (demonstrated as Bragg scattering) waves. VV and HV backscatter at incidence angles 20°, 30°, and 40°, for the three radar-H_{m0} cases are shown in Figure 5.6 (a) and 5.6 (b).

Figure 5.6. Incidence angle dependent (a) VV, and (b) HV backscatter from wind-roughened open water on 1 July (H_{m0} = 136 cm), 9 July (H_{m0} = 66 cm), and 26 July (H_{m0} = 47 cm).

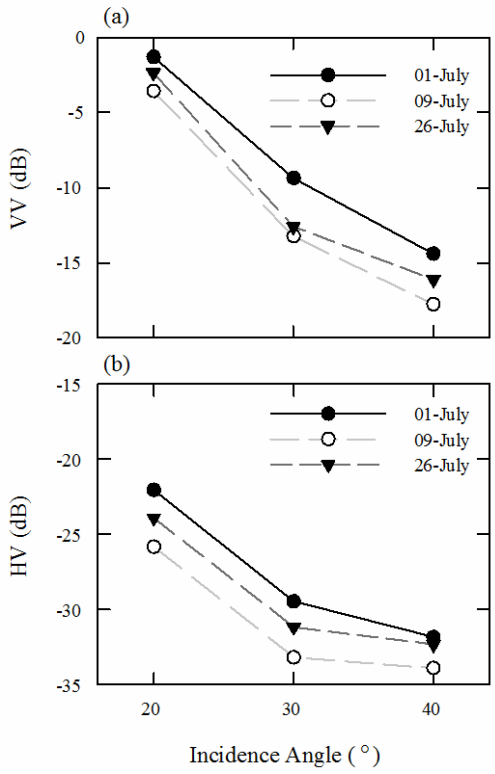

Figure 5.7. Incidence angle dependent ratios, (a) γ_{co} and (b) γ_{cross} from wind-roughened open water on 1 July (H_{m0} = 136 cm), 9 July (H_{m0} = 66 cm), and 26 July (H_{m0} = 47 cm).

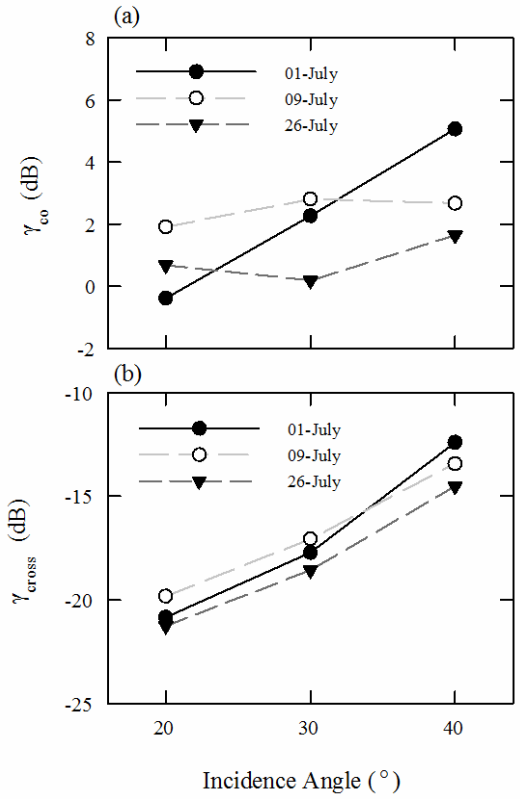

γ_{co} and γ_{cross} for each of the analyzed incidence angles and roughness conditions are shown in Figure 5.7 (a) and 5.7 (b). If we consider the roughness, interpreted using the HV and VV intensities in Figure 5.6, rather than the measured H_{m0}, the γ_{co} at 20° shows similar behavior. The γ_{co} is inversely related to radar-interpreted roughness in a manner described by the Bragg and Integral Equation Model (IEM) surface backscattering models (Fung and Chen, 2010). According to Bragg and IEM theory, the γ_{co} for given incidence angle and dielectric constant, tends to zero (greater HH relative to VV) with increasing surface roughness provided the surface roughness is greater than or equal to the incident wavelength. For smooth surfaces with surface height very small relative to

the incident wavelength, the γ_{co} is independent of surface roughness (Hajnsek et al., 2003). For the roughest H_{m0} case on 1 July, the additional HH backscatter relative to VV is so strong that the ratio at 20° becomes negative. For such a sea state, previous observations show greater HH backscatter sensitivity to the tilt modulation effect caused by larger waves on Bragg waves (Thompson et al., 1998; Trizna and Carlson, 1996), as well as wave breaking (Johnsen et al., 2008).

At 40° incidence angle our observations show correlation between γ_{co} and H_{m0}; which appears to be qualitatively proportionate; i.e. H_{m0} and γ_{co} are much stronger on 1 July while 9 and 26 July are similar. However, the results of Mouche et al. (2005) show that the azimuth angle (direction of waves relative to the radar look angle) must be considered at incidence angles larger than 25°. We have not considered it in the three cases evaluated in this study. In Figure 5.7(b), there is a significant increase in γ_{cross} as a function of incidence angle and a relatively small diversity between sea states.

Figure 5.8. Incidence angle dependent polarimetric coherences, (a) ρ_{HHVH} (b) ρ_{VVHH}, and (c) ρ_{RRLL} from wind-roughened open water on 1 July (H_{m0} = 136 cm), 9 July (H_{m0} = 66 cm), and 26 July (H_{m0} = 47 cm).

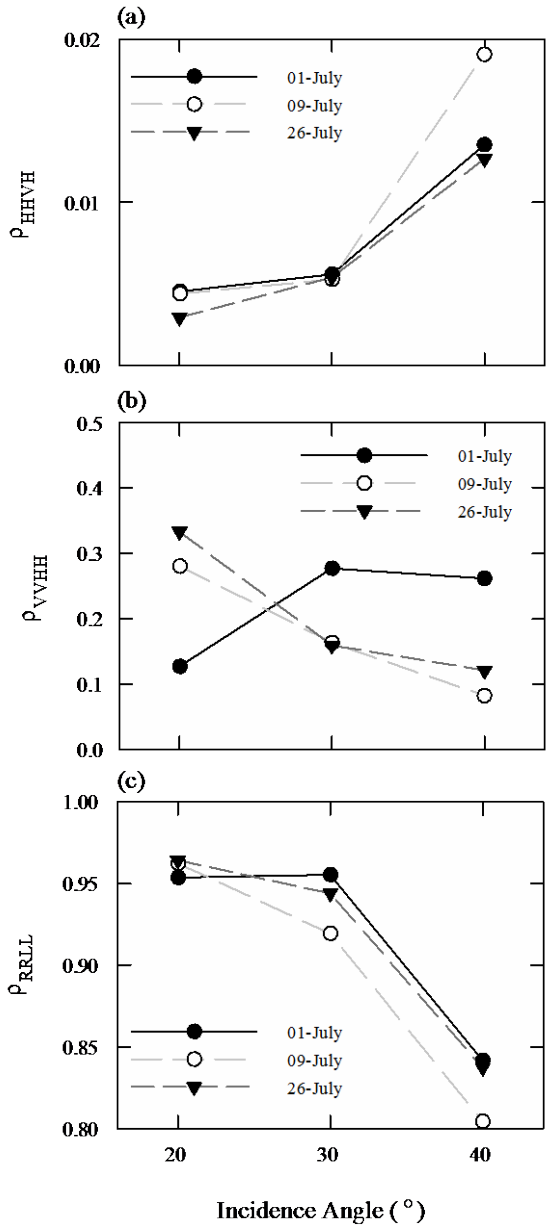

At 40° incidence angle, there is an increase in the ratio of 2 dB between the smooth and rough H_{m0} cases, and the ratio is correlated with the H_{m0}. This effect is most likely attributable to the combined loss of HV backscatter with incidence angle, which is also

evident in Figure 5.6, coupled with an increased sensitivity of VV backscatter to the sea state. In the context of utilizing γ_{cross} from spaceborne SAR, the HV intensity values are very low at incidence angles of 40° and above and must be considered relative to the noise equivalent sigma zero of the utilized sensor at a particular incidence angle.

Figure 5.8 (a)–(c) provide the polarimetric coherence parameters ρ_{HHVH}, ρ_{VVHH}, and ρ_{RRLL} at each of the incidence angles and roughness conditions. Figure 5.8(a) shows the ρ_{HHVH}, a measure of the correlation between complex HH and VH returns. There appears to be no relationship between ρ_{HHVH} and H_{m0} under the constraints imposed in this study. On the other hand, the ρ_{VVHH} in Figure 5.8(b) shows an inverse relationship between the magnitude of the coherence and H_{m0} at 20° incidence angle. This is consistent with an expected greater depolarization of incident polarized radar energy induced by the rougher ocean waves. Beyond 20° there is no discernible relationship between H_{m0} and ρ_{VVHH} that can be deduced on the basis of expected scattering mechanisms. Similar magnitudes of the correlation coefficient are evident for sea states on 9 and 26 July. The rough sea state on 1 July (also seen at 20°) suggests that this parameter has utility for discriminating higher waves. The parameter ρ_{RRLL} in Figure 5.8(c) is expected to be decreasing with increasing surface roughness (Gupta et al., 2013; Hajnsek et al., 2003; Touzi et al., 2004), though this has been developed for terrestrial applications and not well-verified for an ocean surface. At 20° there is only a negligible decrease in ρ_{RRLL} associated with the highest H_{m0} case on 1 July. At incidence angles greater than 20°, the rougher sea state is linked with the highest ρ_{RRLL}, which is contrary to previous results over terrestrial surfaces. An important consideration, however, is the scale of physical roughness, which is much greater for the ocean waves under investigation in this study. Furthermore, in a

study of Jet Propulsion Laboratory (JPL) polarimetric scatterometer observations off the California coast at 13.4 GHz, Lee et al. (2004) found an azimuthal dependency on the ρ_{RRLL}, but did not specify the incidence angle. The study of $\gamma_{\mathrm{co}}$by Keller et al. (1989) (at C-band) mentioned above, shows that the azimuth effect above 25° must be considered for this coherence. The C-band radar observations presented in this study, in particular γ_{co} results in Figure 5.7(b), and the coherence results in Figure 5.8(a)–(c) further support the need to consider ambiguity caused by the azimuth angle when considering the derivation of sea state from polarimetric radar data at incidence angles greater than 25°.

5.4. Conclusions

In this paper, passive microwave emission and polarimetric backscatter measurements were collected coincident to wind and ocean buoy data at spatial and temporal scales relative to airborne and satellite remote sensing studies. A statistical analysis of coincident geophysical variables showed that the T_b is correlated with H_{m0}, but not the wind speed at both H- and V-polarizations, and that it shows a higher correlation with H_{m0} at H-polarization. The PSD and H_{m0} are significantly correlated with the H-polarization of T_b at both of the passive microwave frequencies (better with 37 GHz due to longer wavelength) in this study. An assessment of C-band backscatter points to a dependency of HV and VV intensities on surface roughness; which is resonant to the radar frequency but not captured by the buoy, as shown by greater backscatter intensities for the smoother H_{m0} (47 cm compared to 66 cm) at each of the observed incidence angles. $\gamma_{\mathrm{co}}$and γ_{cross} at 40° are positively associated with H_{m0}, and γ_{co}in particular shows an increase that is proportional to H_{m0} (Figure 5.7).

The polarimetric coherence parameter ρ_{VVHH} at 20° also shows an inverse relationship with H_{m0} that suggests inverse proportionality, due to an expected decorrelation of complex returns with greater surface roughness. The ρ_{VVHH} also holds potential for discriminating rough (H_{m0} = 136 cm) from smooth ($H_{m0} \leq 66$ cm) sea states at 30° and 40°, though this is on the basis of an increase in the magnitude of ρ_{VVHH} with increasing H_{m0} and is contrary to the expected decorrelation for greater surface roughness. Similarly, a decrease in ρ_{RRLL} with increasing roughness, expected for all incidence angles on the basis of previous observations made over terrestrial surfaces, was not observed here. While the results presented here point to the utility of C-band satellite radar for deriving ocean surface physical roughness information without the need for wind speed or azimuth angle information at incidence angles less than approximately 25°, importantly they provide stimulus for further investigations including the azimuth angle for observations above approximately 25°. With an increasing spatial and temporal coverage of open water in the Arctic it will be important to develop robust satellite retrieval algorithms, which examine both gas and energy exchange across the AO interface and into the marginal ice zones of the Arctic.

Chapter 6

Sub-Pixel Evaluation of Sea Ice Roughness Using AMSR-E Data

Mukesh Gupta[1*], and David G. Barber[1]

International Journal of Remote Sensing, (2014), doi:xxxxx (*in review*)

[1]Centre for Earth Observation Science, Department of Environment and Geography, Clayton H. Riddell Faculty of Environment, Earth and Resources, University of Manitoba, 463, Wallace Building, Winnipeg R3T 2N2, Manitoba, Canada

[*]Corresponding Author

Abstract

Rapid reduction of sea ice in the Arctic has necessitated an evaluation of sea ice roughness at smaller scales than those provided by satellites. We evaluate sub-pixel (< 5.4 km) sea ice roughness using AMSR-E brightness temperature (T_b) 89 GHz data and *in situ* physical roughness data acquired using helicopter-based laser system in the southern Beaufort Sea. The analysis shows a statistically significant correlation (regression line slope: −79.92) of T_b at horizontal polarization (H-pol) decreasing with increasing rms heights. The T_b at 89 V-pol also shows an analogous trend with increasing rms height, however, the correlation was not significant. We find that the changing sea ice dielectrics due to melting during April–June prevented an accurate assessment of sea ice roughness using 89 GHz AMSR-E T_b. These results suggest that 89 H-pol is sensitive to changes in physical roughness. The temporal evolution of AMSR-E T_b values at 89 H-pol and 89 V-pol shows a decrease from April through June. The 89 GHz AMSR-E T_b at 5.4 km contained insufficient information to adequately account for changes occurring in the dielectrics and ice roughness at spatial scale of 1–4 km during April–June.

6.1. Introduction

A rapidly changing Arctic environment due to accelerated sea ice reduction in the past few decades has resulted into greater sea ice roughness and enhanced ocean-sea ice-atmosphere interactions (Hutchings and Rigor, 2012; Moore et al., 2014; Nghiem et al., 2007; Pizzolato et al., 2014; Stroeve et al., 2012, 2014). Various oceanic and atmospheric processes acting simultaneously at different spatial and temporal scales in the ice-covered Arctic Ocean produce sea ice roughness both at the surface and at the bottom of sea ice (Gupta et al., 2014). Microwave remote sensing has played a key role in such investigations, with scientists studying the microwave signatures of sea ice for several decades (Comiso, 1986; Gupta et al., 2013; Scharien et al., 2012). Because of a rapidly changing sea ice cover from perennial to seasonal ice, the microwave signatures of the ice cover have changed considerably, and the current satellite-based algorithms do not adequately account for the actual ice conditions (Barber et al., 2009). Passive microwave observations are useful in estimating sea ice concentration (Comiso et al., 1997), surface roughness (Stroeve et al., 2006), and overall sea state of the ocean. In the presence of various ice types and surface roughness of sea ice, however, the passive microwave emissions are further moderated.

Space-based passive microwave studies of the Arctic began in 1972 with the launch of Nimbus-5 Electrically Scanning Microwave Radiometer (ESMR) (Wilheit, 1972); followed by Scanning Multichannel Microwave Radiometer (SMMR) in 1978 (Gloersen et al., 1984); the Defense Meteorological Satellite Program (DMSP) Special Sensor Microwave/Imager (SSM/I) in 1987 (Holllinger et al., 1987); and the Advanced Microwave Scanning Radiometer for EOS (Earth Observation System) Aqua (AMSR-E)

developed by JAXA (Japan Aerospace Exploration Agency) and launched by NASA (National Aeronautics and Space Administration) onboard Aqua satellite in 2002. Several subsequent missions of SSM/I and AMSR-E have been launched in order to provide continuity of Earth observation data. With four decades of experience in passive microwave observations of sea ice in the Arctic, scientists have satisfactorily developed techniques to quantify sea ice concentration, extent, thickness, and volume at specified spatial and temporal scales. However, there are significant gaps in passive microwave interpretation of sea ice roughness at finer spatial and temporal scales. Table 6.1 provides some main specifications of the AMSR-E sensor. The available resampled smallest pixel size in AMSR-E imagery is 5.4 km at 89 GHz. The present paper addresses an evaluation of sea ice surface roughness at a sub-pixel (less than 5.4 km of AMSR-E) level.

Table 6.1. AMSR-E sensor main specifications (Source: NSIDC).

Centre frequency (GHz)	6.925	10.65	18.7	23.8	36.5	89.0
Bandwidth (MHz)	350	100	200	400	1000	3000
Beamwidth (°)	2.2	1.4	0.8	0.9	0.4	0.18
Spatial resolution (km)	56	38	21		12	5.4
[a]IFOV (km)	74 × 43	51 × 29	27 × 16	31 × 18	14 × 8	6 × 4
Sampling interval (km)	10 × 10					5 × 5
Polarization	Horizontal and vertical					
Incidence angle	55°					54.5°
Swath (km)	1445					
Precision	1 K (1σ)					
Quantization	12-bit	10-bit				
Dynamic range (K)	2.7 to 340					

[a]IFOV: Instantaneous field-of-view.

Several mediating factors affect the passive microwave emissions of sea ice; e.g., snow, air temperature, moisture content of snow, all of which go through significant seasonal changes affecting the brightness temperature (T_b) detected by the sensor. Surface roughness significantly affects the T_b of first-year ice (FYI) detected at 6.9 (Hong, 2010), 10.7, 18.7, and 37.0 GHz (Stroeve et al., 2006). The complex dielectric constant of the ice surface encapsulates the effect of changing thermodynamic conditions of the ice. Thus, the variability due to rapidly changing dielectrics can have a significant impact on passive microwave measurements of the geophysical and thermodynamic state of the sea ice (Onstott et al., 1987). Sea ice formation, its breakup, and floe sizes control the surface roughness and hence the passive microwave emission of the sea ice. Lohanick (1990) measured T_b as a function of distance on the ice surface having a non-uniform snow cover and showed that snow could mask the underlying ice roughness, implying that snow (dry or wet) can have potentially significant contribution to T_b. Onstott et al. (1987) calculated values of penetration depths in moist snow at different frequencies. The penetration depth was less than ~5 cm at snow volumetric water content ranging from 0.1–10% at 95 GHz. For a typical snow cover in the range of hundreds of millimeters, dry snow affects the T_b at frequencies above ~30 GHz; and moist snow with water content of merely 1% affects T_b at virtually all microwave frequencies (Carsey, 1992).

The moisture content of snow and snow-ice interface controls the electromagnetic (EM) radiation interaction with the physical roughness of the ice surface. The T_b is very sensitive to the dielectric constant, which is controlled by the type of overlying snow – dry or wet – depending on air temperature and humidity, snow depth and snow density (further dependent on weight of snow layer). Lohanick and Grenfell (1986) found that T_b

did not correlate with snow depth for depths up to 30 cm on cold FYI. The T_b of snow-covered sea ice is also dependent on seasons (Cavalieri et al., 1984; Zwally et al., 1983). Livingstone et al. (1987) suggest that based on microwave signatures, five divisions of sea ice thermodynamic states that are roughly equivalent of seasons may be separable; e.g., winter, initial melt, melt onset, advanced melt, and freeze-up. In this paper, we address evaluation of surface roughness based on passive microwave signatures during winter, initial melt and melt onset (April–June). We intend to investigate how physical roughness at a scale much larger than the EM wavelength (0.34 cm at 89 GHz) relates with the resulting T_b as detected by AMSR-E. The objective of this paper, in view of above background, is to evaluate/establish the sub-pixel level (< 5.4 km) linkages between physical roughness (acquired using helicopter-based laser system) and AMSR-E T_b at 89 GHz during April–June (spring to melt onset).

Figure 6.1. Helicopter-based laser roughness sampling locations and the study site.

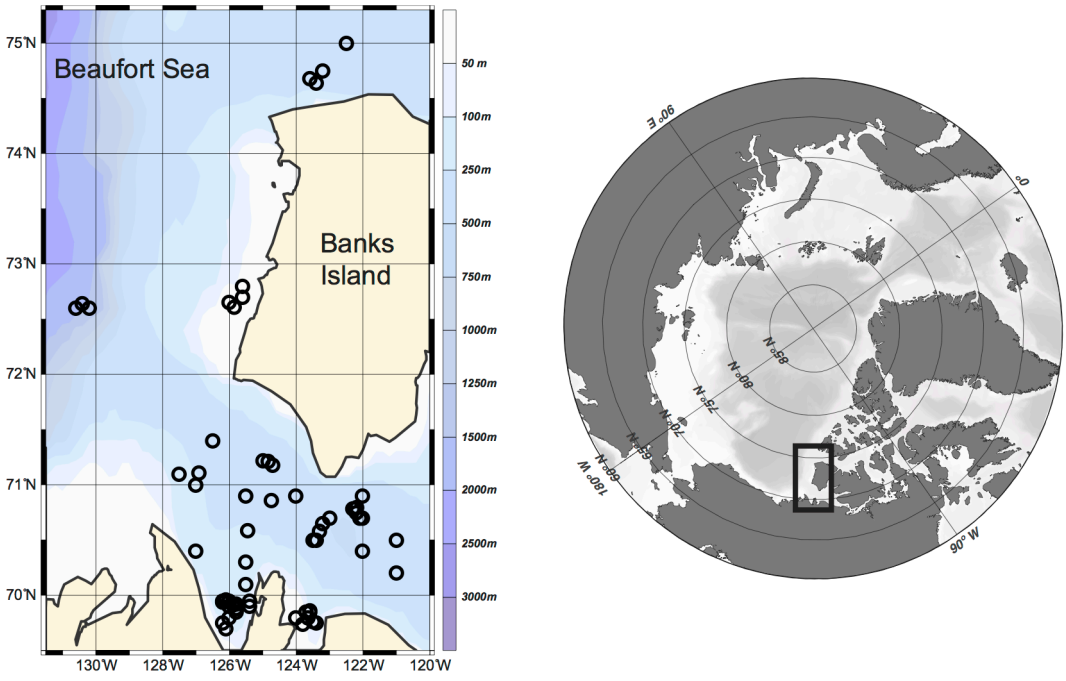

6.2. Materials and Methods

6.2.1. Study Area

The study area lies in Amundsen Gulf in the southern Beaufort Sea (Figure 6.1). The Cape Bathurst Polynya forms in the area and hosts several flaw leads throughout the winter (Barber and Hanesiak, 2004) and the region becomes ice-free in the summer. We acquired field data between April–June 2008 (Legs 7, 8, and 9) as part of the Circumpolar Flaw Lead (CFL) System Study, an International Polar Year (IPY) project that was conducted during October 2007–August 2008 aboard the Canadian Research Icebreaker *Amundsen* [26].

6.2.2. Instrument Description and Data Collection

Sea ice roughness data were acquired using a helicopter-mounted laser system, ADM 3–Alpha Geophysical unit, built by Optech Inc. (Toronto, ON, Canada) with a listed accuracy of 1.5 cm. It generated 905 nm infrared laser beams with a beam divergence of 5 mrad (0.28°). The sampling rate of the ice roughness data is 10 Hz corresponding to a spatial sampling interval of ~4 to 5 m (Nyquist 'horizontal' spatial frequency 0.125 Hz) for the normal helicopter speed of 46.3 m/s (90 knots) from 130 m altitude. The helicopter flights were made during April–June 2008 in horizontal profiles over fully ice-covered Arctic Ocean as the transition from winter to summer occurred. The helicopter flights covered a 1–4 km distance on the ground in each profile. We selected 48 laser profiles pertaining to different dates and locations over the ice. The surface roughness data were processed and calibrated to retain only the ice surface heights. Thus, the sea ice

roughness data contained surface height values from the ice surface only. These profiles were selected, for comparison to AMSR-E T_b, based on the data quality, temporal match between various datasets, and sufficient number of data points within datasets. Each profile contained numerous data samples with 277 and 58,449 discrete height data points. These data samples can be regarded as the realizations of a random process from an anisotropic rough surface representative of the FYI in the southern Beaufort Sea from spring to summer. We used one-dimensional piecewise cubic Hermite interpolation to replace the null and not-a-number (NaN) values in the entire data to obtain root-mean-square (rms) values of height for each data series.

6.2.3. AMSR-E Data

We downloaded Version 3 of calibrated AMSR-E T_b data from the National Snow and Ice Data Center (NSIDC) data pool (Ashcroft and Wentz, 2013). The AMSR-E Level-2A product (AE_L2A) contained T_b at 89.0 GHz and other frequencies (not used in the present analysis). We have used high-resolution 5B-swath ascending data, which covers the southern Beaufort Sea. AMSR-E's 89 GHz channel provides the highest available spatial resolution of 5.4 km preferable for surface roughness studies, and the 89 GHz horizontal polarization (H-pol) channel is sensitive to surface roughness (Svendsen et al., 1983). The atmospheric effects, e.g., water vapor and cloud liquid water considerably influence the 89 GHz channel (Spreen et al., 2008; Svendsen et al., 1983). Version 3(V003) provides improved inter-calibrated data with other microwave radiometers, particularly SSM/I F13 and WindSat; and calibrated with improved Radiative Transfer Model (RTM) with adjustments of the water vapor and oxygen absorptions, particularly

the water vapor continuum absorption (Meissner and Wentz, 2012). Resampled data were spatially consistent, at a resolution that corresponded to the footprint size of the observation, i.e., 5.4 km (Table 6.1). Each swath was packaged with associated geolocation fields.

Data were stored in Hierarchical Data Format–Earth Observing System (HDF-EOS) format. We organized the data with an arbitrary center coordinate at −124°W and 71°N for each image. The plots were created using Stereographic projection with a radius of 5°. Subset images were created for April–June 2008 on various dates for which surface roughness data were acquired using the helicopter-based laser system. The T_b values were picked from the subset image at known locations of the helicopter flight. The stored data value (digital number) was converted into T_b (kelvin) using the scale factor and offset values given in each HDF data file (Eq. 6.1).

$$TB\ (kelvin) = (stored\ data\ value\ \times\ 0.01) + 327.68. \tag{6.1}$$

The mean surface air temperature data have been extracted from NCEP (National Centers for Environmental Prediction) reanalysis surface level products created by NOAA (National Oceanic and Atmospheric Administration)/ ESRL (Earth System Research Laboratory) Physical Research Division.

6.3. Results and Discussion

6.3.1. Linkages Between rms Height and AMSR-E Brightness Temperature

This paragraph gives a foreground of why this dataset were suitable for establishing above-mentioned linkages. The sea ice under consideration is rough and deformed FYI during spring to melt onset (April–June). The entire ice field had a snow cover varying in snow thickness ranging between 5–70 cm, accumulated since freeze-up in October-November. By mid-April, the ice cover had already undergone several significant upheavals in weather; for example, changes in air temperature and humidity. These changes in atmospheric conditions are recorded in the snow and ice layers (Livingstone et al., 1987), manifested in the resulting dielectric constant of the ice, and its microwave signatures. The penetration depth of EM radiation into saline FYI at higher frequencies is considerably small. Higher frequency (89 GHz) for surface roughness investigation is preferable because of two reasons: First, and as previously noted, the EM radiation at higher frequencies does not penetrate much into saline FYI; and secondly, the scattering of higher frequency radiation is greater by the rough ice surface thus facilitating detection of a rough surface. Lower EM frequencies respond to the volume of ice due to greater penetration depth and are therefore not as appropriate for roughness detection.

Figure 6.2 shows the temporal variability in rms height data acquired using the helicopter-based laser system from spring to melt onset. The maximum and minimum rms heights acquired were 0.35 and 0.07 m, respectively. Before evaluating a relationship between T_b and rms height, we checked the statistical distributions of the respective datasets. The statistical probability density distributions and histograms of various

profiles were shown to be approximately Gaussian (Figure 6.3). The vertical polarization (V-pol) distribution appears to be slightly negatively skewed.

Figure 6.2. Plot shows the averaged rms height data acquired during April–June from the helicopter-based laser system (number of samples = 48). Maximum rms height = 0.35 m; minimum rms height = 0.07 m.

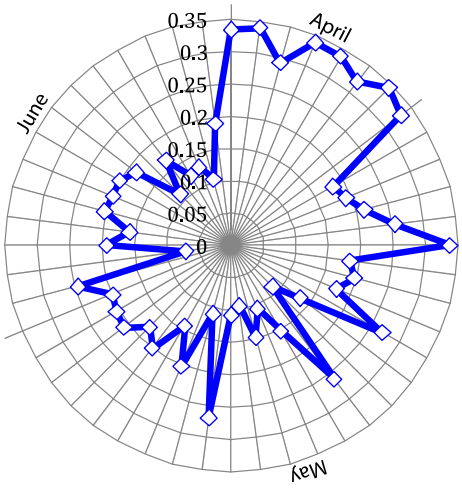

Table 6.2. Coefficient of determination (r^2) and regression statistics between AMSR-E T_b and rms height (h) (number of samples = 48).

Linear Regression	r^2	P-value
$T_bV = -66.7h + 271.68$	0.48	< 0.05
$T_bH = -79.9267h + 261.01$	0.61	< 0.05

Table 6.2 shows linear regressions between rms height and T_b at H-pol and V-pol at 89 GHz. The P-value < 0.05 suggests that the relationship is statistically significant. Table 6.3 summarizes the descriptive statistics of Gaussian distribution of rms height and T_b data at 89 H-pol and 89 V-pol.

Figure 6.3. Probability density distributions of the rms height, and AMSR-E T_b data at 89 H-pol and 89 V-pol. The data is approximately Gaussian as shown by the respective histograms and density curves.

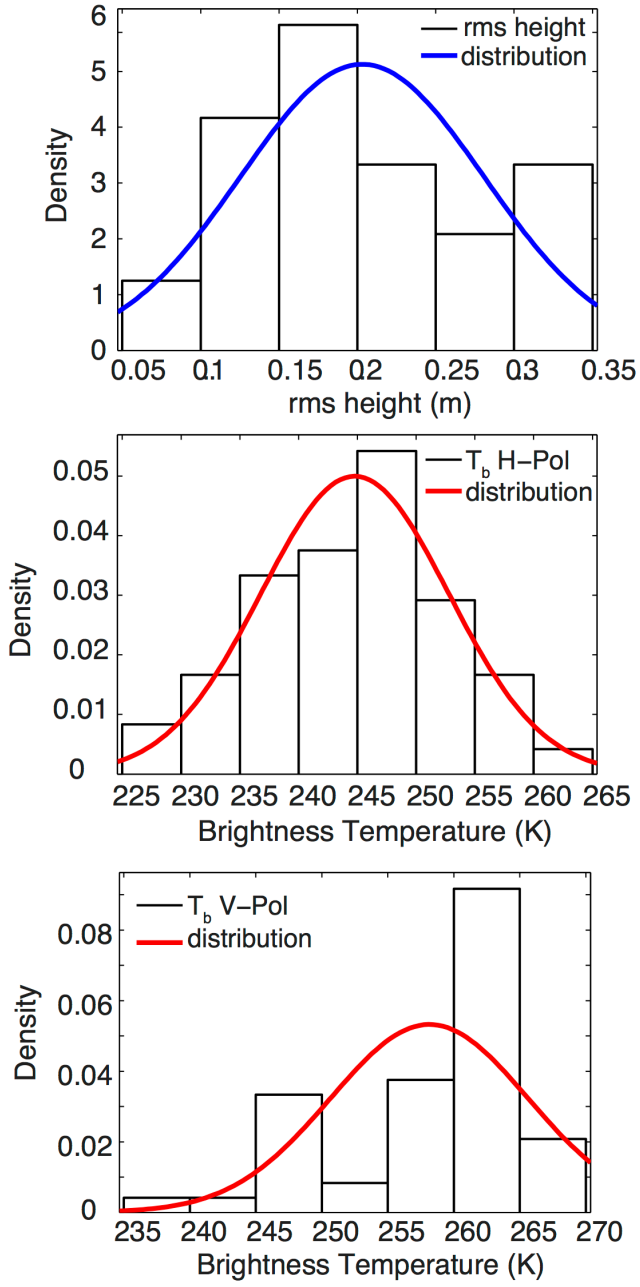

Table 6.3. Normal distribution statistics of various data (number of samples = 48).

Normal distribution parameter		Std. Err.	Estimate
rms height (m)			
	μ	0.0112	0.2031
	σ	0.0081	0.0778
T_b-H (K)			
	μ	1.1527	244.784
	σ	0.8281	7.986
T_b-V (K)			
	μ	1.0817	258.139
	σ	0.7771	7.494

Figure 6.4. Linearity plot (P-P plot) for the regression between T_b 89 H-pol and rms height (number of samples = 48). The plot shows that the two datasets closely agree to each other.

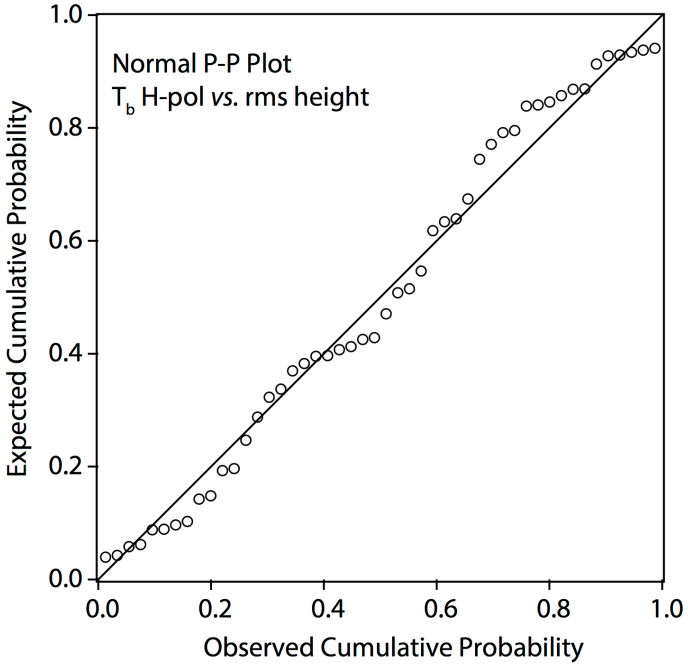

The linearity plot (P-P plot) for the regression between T_b at H-pol and rms height also implies correlations between the two datasets (Figure 6.4). This result is interesting from multiple viewpoints. First, the H-pol T_b shows better correlation with the rms height compared to T_b at V-pol (Table 6.2). Secondly, the T_b at both polarizations tends to decrease with increasing rms height (Figure 6.5). Although the physical roughness goes up to 35 cm, the penetration depth of EM radiation at 89 GHz is ~5 cm. Thus, the contribution to T_b primarily comes from the top 5 cm of the snow or ice surface. This indicates that the roughness interface dictated by the penetration depth of EM waves at 89 GHz does not match well with the actual physical roughness interface measured by the helicopter-based laser system. This finding is consistent with the findings of Lohanick (1990) who demonstrated the effect of snow layer over rough multiyear ice on the T_b. This result also shows that despite increasing physical roughness, the T_b decreases likely due to a rapidly changing dielectric constant caused by thermodynamic evolution of the surface layer of ice during April–June. Wet snow permittivity is 1.4 for 0% water content (dry in April) to 3.3 for 12% water content (wet in June) at snow density 0.25 g cm^{-3} (Ulaby et al., 1986, Figure E.38); permittivity of first year ice is 3.3 at −10°C (Ulaby et al., 1986, Figure E.24).

Figure 6.5. Linear regression between AMSR-E T_b at 89 H-pol (*blue*) and 89 V-pol (*red*) and rms height for roughness data collected between April–June 2008 (number of samples = 48). Table 6.2 shows the regression equations and the statistics.

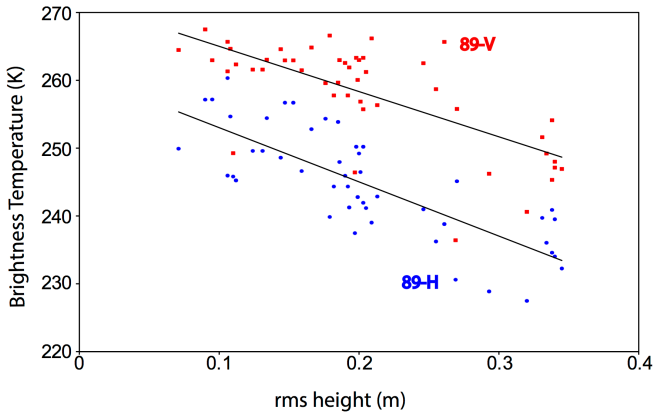

6.3.2. Temporal Evolution of Brightness Temperature During April–June

Figure 6.6 shows the temporal evolution of T_b during April–June at select locations where helicopter-based laser roughness measurements were made. We do not observe any significant trend in the T_b values at the select locations; however, there is a drop in T_b values around the first week of June (Julian Day 149–155).

Figure 6.6. The changes in AMSR-E T_b, 89 H-pol (*blue*) and 89 V-pol (*red*), observed at the locations of roughness measurements, between April–June of 2008.

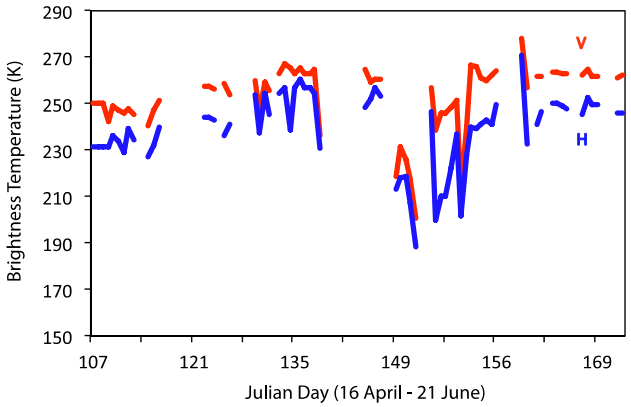

Figure 6.7 shows the NCEP reanalysis monthly mean surface air temperatures from April to June. It shows a dramatic change in surface temperature from −19.5°C in April to 8°C in June. It gives an idea of the atmospheric conditions that can have a significant effect on the electrical properties (dielectric constant) of snow and underlying sea ice, the dielectric constant being extremely sensitive to the temperature. Figure 6.8 shows the T_b at 89 GHz H-pol, which depicts a decrease in the T_b values from April through June. As indicated previously in our results, 89 H-pol shows better correlation with the rms height and decreases with increasing roughness.

Figure 6.7. Monthly mean surface air temperature during April–June 2008 around the study area. The data are NCEP reanalysis surface level products from NOAA/ESRL Physical Sciences Division. It shows a change in monthly mean temperature from −19.5°C in April to 8°C in June.

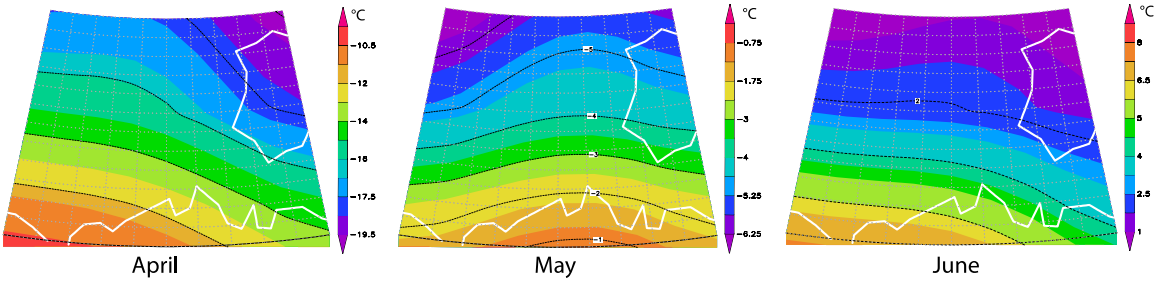

A scatter plot of 89 H-pol versus 89 V-pol shows linear alignment of points most of which cluster toward higher T_b values indicating FYI signatures (Carsey, 1992) (Figure 6.8). The minimum T_b value in the data is 227.48 K (89 H-pol); which is much higher than typical T_b from melt water/seawater that have low T_b values. A change in atmospheric conditions is normally observed in the southern Beaufort Sea beginning of June when air temperature rises and the initial melt of sea ice occurs (Scharien et al., 2012). Diverting our focus from select locations of helicopter roughness data sampling to

a larger scale covering the entire southern Beaufort Sea and Amundsen Gulf, the temporal evolution in T_b has been plotted using AMSR-E data (not-resampled) during April–June.

Figure 6.8. AMSR-E T_b plot (89 GHz V-pol versus 89 GHz H-pol) for snow-covered FYI in southern Beaufort Sea during April–June 2008 for stations where physical roughness measurements are taken (number of samples = 48).

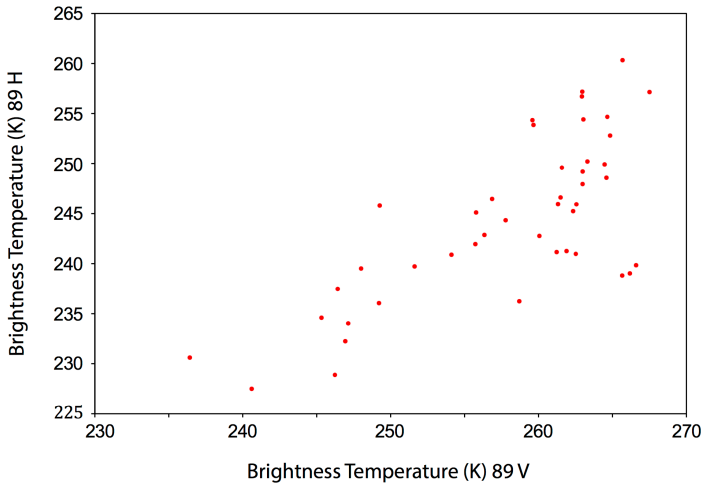

The increasing snow water content of the ice surface causes greater dielectric loss in the ice, therefore reducing the T_b as detected by AMSR-E. The snow-ice interface, at this time of year, gets wetter because of collapsing snow layer with drainage to the ice surface as the pendular regime turns into funicular regime (Barber, 1995). A flaw lead opened up in the eastern shore of Amundsen Gulf, as discernible through AMSR-E T_b image of 11 May, exposing open water to the sensor (Figure 6.9). T_b values as low as 180 K can be seen in the Gulf from 11 May onwards until 21 June. A similar flaw lead is discernible west of Banks Island from 11 May onwards. An analogous T_b pattern is observable in the V-pol suite of images provided in Figure 6.10. This also shows that H-pol is more

sensitive to changes in the dielectric behavior and surface roughness of ice than V-pol. The T_b at 89 V-pol remains above 220 K even for the open water areas. When we compared T_b at select locations of helicopter roughness measurements, V-pol showed marginal correlation with the rms heights. Now, considering the entire southern Beaufort Sea, an analogous behavior of a decrease in T_b is observed.

The extraction of surface roughness signatures from the satellite-based T_b of natural sea ice conditions encountered during April–June (late spring to melt onset), is challenging because of the rapidly changing dielectric properties caused by thermodynamic changes in the overlying snow cover, snow-ice interface, and underlying sea ice (even after AMSR-E data are atmospherically corrected accounting for atmospheric moisture and clouds). Lower frequencies are not preferable due to their greater sensitivity to the changing dielectrics and larger penetration depth capability. The use of 89 GHz has been considered as the most reasonable choice for studying the surface roughness signatures from the T_b. Secondly, the composite brightness signal collected at the AMSR-E sensor from within 6 km × 4 km (IFOV- Instantaneous Field-of-View, see Table 6.1) of surface area poses difficulty in correlating it with the *in situ* helicopter-based laser roughness data at much smaller scales. The electrical and geometrical changes in the sea ice surface occur faster and at smaller scales than those detected at temporal and spatial scales provided by AMSR-E. The AMSR-E T_b values contain insufficient information to adequately account for changes occurring in sea ice dielectrics and surface roughness at sub-pixel level. Further work is required to understand the impacts of thermodynamics on the passive microwave emissions and how they relate to the roughness of the marginal ice zone. This work will benefit from the application of a

microwave emission model to separate out geophysical and dielectric complexities of the seasonally evolving marginal ice zone roughness.

Figure 6.9. Sequential (April–June 2008) images of AMSR-E T_b at 89 H-pol in the southern Beaufort Sea and Amundsen Gulf. The T_b at 89 GHz H-pol shows decreasing values in the Amundsen Gulf from April through June 2008.

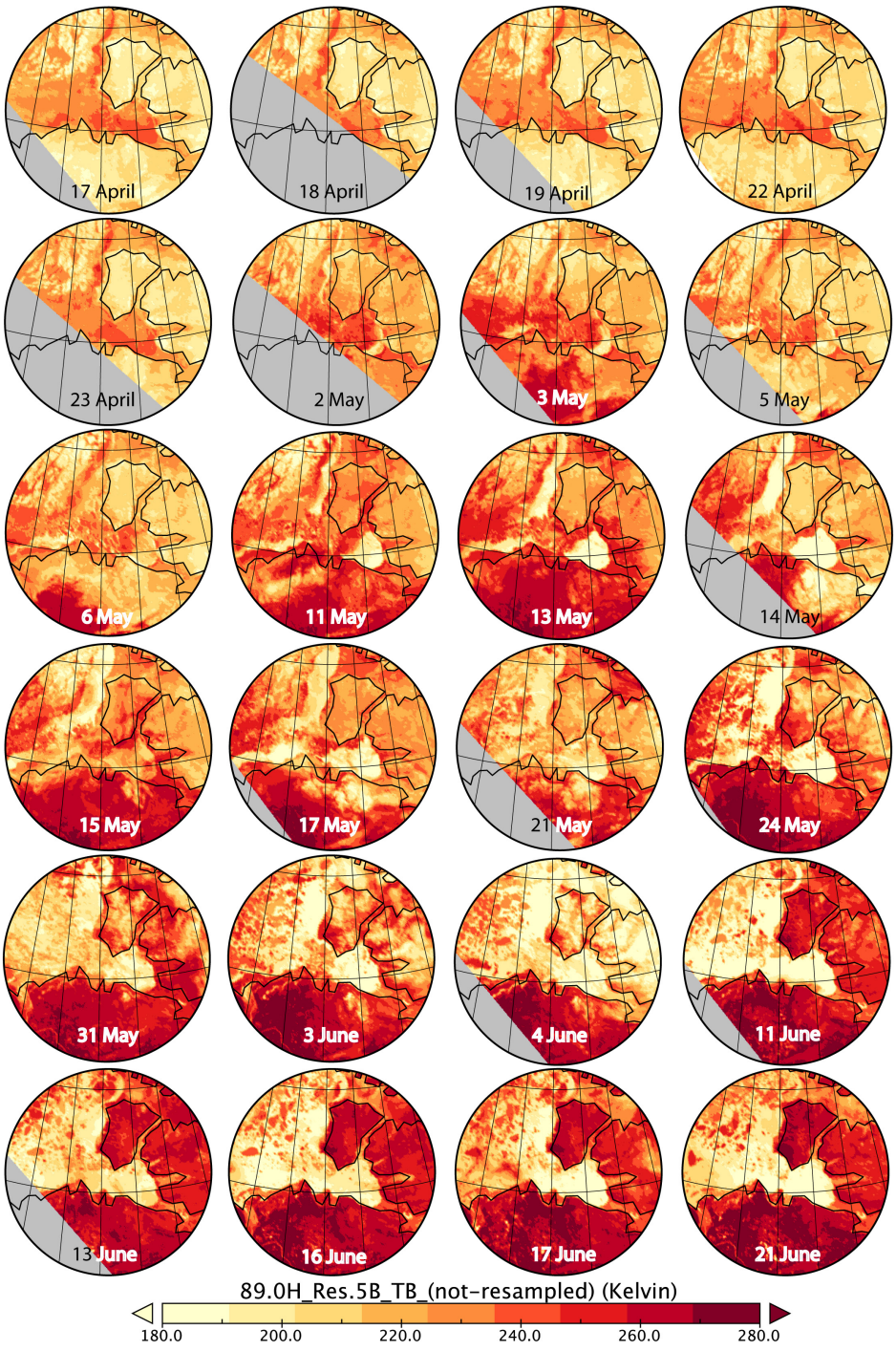

Figure 6.10. Sequential (April–June 2008) images of AMSR-E T_b at 89 V-pol in the southern Beaufort Sea and Amundsen Gulf. The T_b at 89 GHz V-pol shows decreasing values in the Amundsen Gulf from April through June 2008.

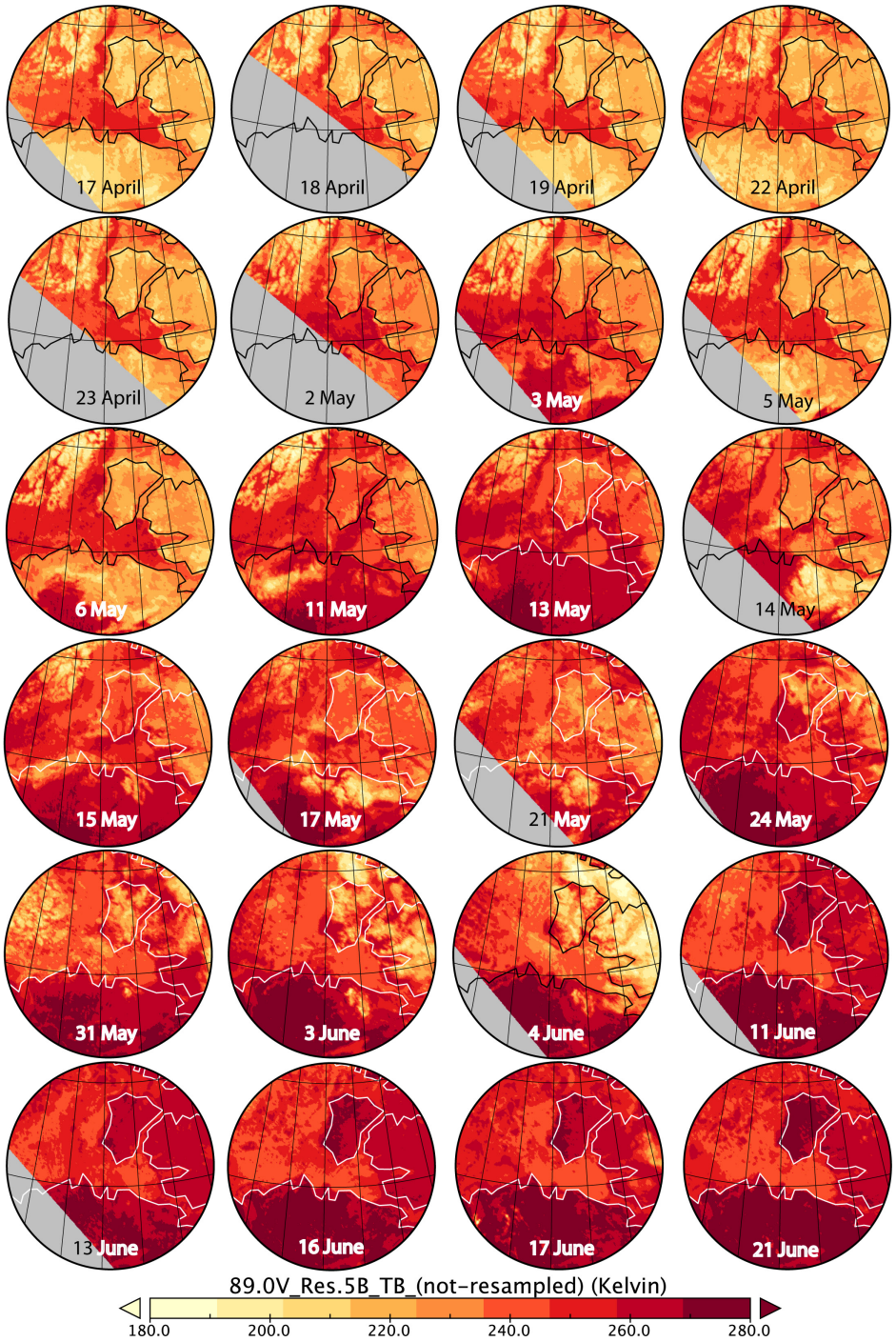

6.4. Conclusions

We presented, in this paper, an evaluation of sub-pixel (< 5.4 km) sea ice roughness using AMSR-E T_b data and *in situ* rms height data acquired using a helicopter-based laser system. The rms height data were acquired from helicopter flights made inside the pixel size, i.e. 5.4 km. The rms heights, obtained from horizontal roughness profiles varying over ground distances of 1–4 km, were correlated with corresponding T_b values found in the associated pixel in the AMSR-E image. The analysis shows a statistically significant correlation (regression line slope: −79.92) of T_b at horizontal polarization (H-pol) decreasing with increasing rms heights. This can be explained by the rapidly changing electrical properties (dielectric constant) caused by thermodynamic evolution of overlying snow cover, snow-ice interface, and underlying FYI during April–June. The dielectric loss increased with increasing snow water content, thus reducing the T_b as detected by AMSR-E despite increase in physical roughness of ice surface. The T_b at 89 V-pol also showed an analogous trend with increasing rms height; however, the correlation was not significant. However, these results suggest that 89 H-pol is more sensitive (than 89 V-pol) to changes in physical roughness in agreement with Svendsen et al. (Svendsen et al., 1983, 1987). We conclude that rapidly changing dielectrics due to thermodynamic evolution during spring to summer hinder a reasonable and substantive assessment of sea ice roughness from AMSR-E T_b for spatial scales less than 5.4 km.

We also investigated the temporal evolution of T_b signatures from late spring (mid-April) to melt onset (mid-June) in view of the *in situ* physical roughness measurements. The decreasing T_b values in the entire study area were clearly discernible from April through June. The T_b values at 89 H-pol at pixel size of 5.4 km decreased from April

through June, caused by the flaw leads that opened (identified in sequential AMSR-E images of 11 May and onwards) in the eastern shore of Amundsen Gulf and west of Banks Island. An analogous decrease in T_b at 89 V-pol is also observed during April–June. The magnitude of T_b values of 180 K at 89 H-pol suggested open water (because of lead openings and expanding open water areas in June) signatures.

It is challenging to separate out physical roughness from the seasonally variable dielectric contribution to the T_b at 5.4 km spatial resolution of AMSR-E. The sub-pixel evaluation of T_b, at present, only relies on the *in situ* radiometer observations in conjunction with simultaneous consideration of several other variables responsible for moderating electrical and geometrical properties of snow-covered FYI. The results from this analysis highlight the need for a numerical microwave emission model that includes mediating factors, e.g., air temperature, snow-ice interface water content, brine, physical roughness, and humidity to downscale the T_b at 5.4 km to a spatial and temporal scale where changes in dielectrics and surface roughness actually occur. We will investigate the potential for the Microwave Emission Model of Layered Snowpacks (MEMLS) as such a candidate model (Wiesmann and Mätzler, 1999) in our next contribution on this topic.

Chapter 7

Summary and Conclusions

The research work presented in this thesis was an attempt to understand physical roughness of the MIZ. Four different sub-objectives were: the technique development for detection and classification of physical roughness for various sea ice types in a MIZ; utilization of active microwave polarimetric coherences and ratios for sea ice roughness discrimination; open water roughness estimation using *in situ* active and passive microwave signatures; and an evaluation of the temporal evolution in passive microwave signatures of sea ice roughness at a sub-pixel level (< 5.4 km) using AMSR-E data.

In the Section 7.1, I present a brief summary of results associated with each objective followed by, in the Section 7.2, conclusions and linkages between four objectives addressing the overarching objective.

7.1. Summary of Results

Chapter-3 detailed the extensive statistical analysis for the detection and classification of separable sea ice classes in the southern Beaufort Sea MIZ through a range of spatial and temporal scales. The discrimination of surface roughness was investigated using analysis of variance (ANOVA) of the helicopter-based and ship-based laser roughness data, ship-based active and passive microwave data, to achieve statistically significant classes of sea ice types.

Merely the visual observations of sea ice types and surface roughness are insufficient to account for the variability and diversity of sea ice surface. The ANOVA of laser roughness was performed to examine if the classes were statistically different from one another. Analogously, the ANOVA of HH, VH, and VV polarization *in situ* backscattering coefficient data and brightness temperatures at 37 and 89 GHz at H and V polarizations were performed at 0–30 m scale. No statistically different groups were formed in the laser data due to similarity of means. Passive microwave brightness temperature data produced only one sea ice group. The ANOVA of backscattering coefficient of different polarization combinations (HH, VH, and VV) created statistically different sea ice classes. Thus, active microwave polarimetric data of sea ice have potential utility in separating different sea ice surface types with further aid of polarimetric coherences and ratios (see Chapter-4).

Chapter-4 evaluated the utility of C-band polarimetric backscatter, coherences and ratios as a discriminator of sea ice surface roughness. Circular, co-, and cross-polarized coherences and polarization ratios were computed for different sea ice surfaces to examine sensitivity to surface roughness. An existing one-dimensional backscatter model was modified to consider two-dimensions of surface roughness by incorporating deviation in the orientation angles (i.e. the slopes) in azimuth and range directions simultaneously as an improvement in the model for surface roughness.

Backscattering coefficients at HH, VH, and VV polarization and polarimetric coherences of two frost flower cases, snow-covered first-year ice, pancake ice, and deformed first-year ice were examined. The observed circular coherence, for the improved two-dimensional model of surface roughness, showed a strong dependence on

both the dielectrics and surface roughness. The co-polarization ratio is more sensitive to surface roughness compared to cross-polarization ratio confirming previous work on sea ice. Cross-polarization coherence was observed to be less sensitive to roughness, thus coherence and ratios can be used together to discriminate rough ice.

Chapter-5 addressed thesis objective-3 and estimated open water roughness in the southern Beaufort Sea. I investigated the relationships between geophysical variables associated with open water roughness (wave height, spectral density) and ship-based microwave backscatter/emission. Active co- and cross-polarization ratios and polarimetric coherences were used to interpret open water roughness.

Wave height data, ranging between 12–214 cm, were used to establish a relationship between the non-dimensional form of energy and the wave age, to assess wave scenarios in the ice-free southern Beaufort Sea. Results from this analysis match very well with the theory of wind-generated wave growth. Three different cases of wave heights (low to high) were matched with theoretical wave spectra. The passive microwave brightness temperature at 89 GHz H-polarization from waves (within ~10 km from ice edge) was found to increase with increasing significant wave heights. The wave power spectral density and the wave height were well correlated with the observed brightness temperature at 37 and 89 GHz. Polarimetric coherences were found to be less sensitive in the detection of open water roughness near the ice edge. Co-polarized coherence was observed to decrease with increasing significant wave height.

Chapter-6 addressed thesis objective-4 and evaluated sea ice roughness at sub-pixel scales (< 5.4 km) using AMSR-E data at 89 GHz. This paper used helicopter-based laser roughness measurements in the southern Beaufort Sea to investigate how roughness data

from within 1–4 km relates to the passive microwave data from 5.4 km (pixel size). The temporal evolution in passive microwave signatures from spring to summer melt (April–June) was also investigated.

Linkages between helicopter-based rms height and AMSR-E brightness temperature were established for snow-covered first-year ice during April–June in the southern Beaufort Sea. A significant correlation was found between brightness temperature at 89 GHz H-polarization and rms height. Brightness temperature was observed to decrease with increasing physical roughness. An analogous relationship, although statistically non-significant, was also observed between the brightness temperature at 89 GHz V-polarization and physical roughness. Both physical roughness data and brightness temperature data were normally distributed.

7.2. Conclusions

The overarching goal of this research was to investigate the physical roughness of the southern Beaufort Sea using microwave remote sensing methods, which included ship-based observations, helicopter-based laser roughness measurements, and satellite-based passive microwave emissions of the MIZ. To achieve this goal, four interrelated sub-objectives of this research were addressed. The conclusions with inter-links between the sub-objectives are as follows:

- The use of state-of-the-art tools; for example, polarimetric microwave observations and its extensive statistical analysis provide useful insight into the detection and classification of sea ice roughness. The ANOVA of laser roughness and passive microwave brightness temperature yield only one statistically separable class, which

implies that the sea ice classes, despite being different, are grouped as statistically similar except for the cases where snow cover was significant. The investigation of purely statistical nature of brightness temperatures over different sea ice surfaces requires further research. This leads me to conclude that the directional dependence of brightness temperature could be of utmost importance for meaningful extraction of surface roughness from the brightness temperature.

- For microwave polarimetric analysis of surface roughness, two dimensions should be considered to effectively address the signatures from rough sea ice. This change from an existing one-dimensional model of surface roughness to two dimensions provides better insight into surface roughness by considering orientation angles in azimuth and range direction simultaneously. The circular coherence in the one-dimensional model is considered to be a discriminator of roughness and theoretically independent of dielectric contributions from ice. However, in the improved two-dimensional model, the circular coherence is found to be dependent on both surface roughness and the dielectric constant of ice. Thus, it is concluded that circular coherence currently does not provide robust ice roughness discrimination, as previously shown in the literature (Mattia et al., 1997).

Other polarimetric coherences also provide a vague interpretation of surface roughness limited only for certain incidence angles. Co-polarized coherence is smaller for far range incidence angles for all ice types. Cross-polarized coherence is less sensitive to roughness, thus is not a good discriminator of ice roughness. The co-polarized ratio is more sensitive to roughness compared to the cross-polarized ratio.

- The statistical analysis of wave parameters and passive microwave emissions reveals that the two are well correlated with each other; however, the wind speed is not

directly correlated with microwave emission. This leads me to conclude that it takes some time for wind energy to cause growth of waves (surface roughness) after the energy is imparted to the ocean, to be able to be detected by microwave sensors. Because of this time lag, no correlation is found between wind speed and microwave emission, but wave heights and spectral density are well correlated with the microwave emission. Polarimetric coherences hold potential for discriminating roughness from smooth sea surfaces, but require more detailed experiments for open water. The co-polarized ratio shows an increase with increasing wave height.

- Horizontally polarized brightness temperature of snow-covered first-year ice is well correlated with rms height in an inverse manner. The inverse relationship between the two may be the outcome of two major possibilities: 1) the brightness temperature decreases from spring to melt onset (April–June), and 2) the spatial resolution of the two measurements are not in agreement with each other. AMSR-E spatial resolution (5.4 km at 89 GHz) and roughness measurements (1–4 km) pose challenges in analysis. A downscaling of AMSR-E data or roughness measurements at the same scale is likely to provide a better correlation between brightness temperature and roughness. The rough surface as seen by AMSR-E (dependent on penetration depth) is significantly different from the rough surface detected by the helicopter-based laser system. This may lead to misinterpretation and misclassification of rough ice as seen in AMSR-E products.

Temporal evolution of sea ice is clearly captured in the AMSR-E brightness temperature images from April to June. The decrease in brightness temperature from April to June at both 89 GHz H- and V-polarization is due to smaller emissivity of water than ice as sea ice progresses toward melt onset in June. The magnitude of brightness

temperature values of 180 K indicates expansion in open water areas in the eastern shore of Amundsen Gulf and west of Banks Island. To evaluate sea ice roughness at sub-pixel scales (< 5.4 km), a two-dimensional model taking all mediating factors (snow density, air temperature, humidity to name a few) that affect microwave signatures of sea ice, needs to be considered, because the temporally changes in brightness temperature occur faster than those detected by the sensors.

The first objective was to examine the capability of advanced statistical methods to extract information from laser roughness and microwave data, which is not discernible through only visual investigations. It is possible to detect and classify sea ice classes from active microwave data using advanced statistical methods. Further analysis (polarimetric) of active microwave backscattering data shows that various combinations of polarimetric coherences and ratios provide useful insight in discriminating sea ice types. It is addressed in the second objective that one-dimensional model of sea ice roughness is invalid in correctly explaining the ice in MIZ. In addition to the advanced statistical analysis, two-dimensional ice roughness model using polarimetric data provided detailed insights in understanding sea ice roughness dynamics in MIZ. Moving from ice toward the open sea, in the vicinity of MIZ, the influence of wave height and its brightness temperature data further adds another useful dimension in understanding the MIZ. The third objective essentially looked into the wind-waves relationship in the vicinity of MIZ using advanced active polarimetric and brightness temperature. Here too, the polarimetric active microwave techniques and passive microwave brightness temperature at dual-polarization proved to be immensely useful. In the fourth objective, I tried to conjoin the knowledge acquired from above three papers to investigate seasonal sea ice evolution

(spring through melt onset) more closely using passive microwave emissions as detected by AMSR-E assisted with airborne roughness data. It was the objective to see whether it is possible to interpret sea ice evolution and microwave signatures of roughness from space in the same manner, as they are observed *in situ*. However, spatial and temporal inconsistencies as well as inadequate representation of sea ice microwave properties in models prevented such investigations.

Original Research Contributions:

This thesis has demonstrated that a multitude of state-of-the-art methods, various types of multi-dimensional data at varying spatial and temporal scales are needed to adequately address the complex behavior of sea ice in a MIZ.

- This research work suggests that advanced models of sea ice should consider statistical discrimination and classification techniques. Especially, the ANOVA of active polarimetric data from sea ice clearly discriminates sea ice classes.
- Adding to the statistical utility of polarimetric microwave data, various polarimetric coherences and ratios were found to be useful in identifying sea ice types. This study showed that one-dimensional sea ice roughness geometry does not fully account for the correct polarimetric response of ice roughness; a two-dimensional model provides further details, but is complex to interpret.
- The observed circular coherence, for the improved two-dimensional model of surface roughness, showed a strong dependence on both the dielectrics and surface roughness.

- No correlation is found between wind speed and microwave brightness temperature, but wave heights and spectral density are well correlated with the brightness temperature.
- The investigations of seasonal sea ice evolution using satellite data at sub-pixel scale suggest that temporal changes in sea ice occur faster than those detected by the satellite thus making it difficult to interpret the satellite data at scales < 5.4 km.
- For wind speeds 0-10 m/s, the formula is derived: $\frac{g^2 \mathrm{H_{m0}}}{\mathrm{U}^4} = 0.00817 \left(\frac{\mathrm{U}}{c_p}\right)^{-3.132}$.

(see Chapter-5 for symbols)

- A new 2D relationship between slope in azimuth and ground range, radar look angle, shift in azimuth, and shift in ground range is derived: $\frac{\tan\omega}{\tan\theta_1} = \sin\theta_2(\tan\gamma.\sin\phi + \cos\phi) + \cos\theta_2(-\tan\gamma.\cos\phi + \sin\phi)$. (see Chapter-4 for symbols)

7.3. Future Research

The statistical discrimination of sea ice surface found in a MIZ using microwave methods (active and passive) can be further explored using satellite remote sensing and can pave the way for remote discrimination of surface roughness. I did not consider the effect of surface roughness anisotropy on backscatter (i.e., the dependence of backscattering on the direction of measurement to account for ice slope, orientation, and surface geometry). This can be achieved by two-dimensional high-resolution roughness measurements at the same spatial and temporal scales at which changes in microwave signatures of sea ice occur. The problem of sea ice discrimination using microwave methods mainly revolves around spatial and temporal consistencies in physical roughness and microwave

measurements irrespective of the measurement platform, because of the fast changes that occur in the microwave properties of sea ice at different scales.

Polarimetric microwave investigations of sea ice hold the clue to discriminating various ice types and surfaces with greater confidence at desired spatial and temporal scales. The requirement for this, as realized from this research work, is a very well designed polarimetric microwave data acquisition at meaningfully acceptable spatial and temporal scales, synchronized with other instruments. These *in situ* observations can be particularly useful for interpretation of satellite measurements once planned SAR constellations (Sentinel series, Radar Constellation Mission) are available as planned with European Space Agency and Canadian Space Agency.

It would be interesting to explore the ocean surface roughness using polarimetric microwave observations incorporating the azimuth angle in addition to incidence angle for observations above 25°. This thesis (Chapter-5) showed the potential utility of C-band satellite SAR for deriving ocean wave roughness without the need for wind speed at incidence angles less than 25°. The finding that H-polarization brightness temperature at 37 and 89 GHz correlate well with significant wave height and wave power spectral density, suggests that more detailed research at other microwave frequencies and polarimetric passive emissions that build on the present framework, can be desirable.

We know that the spatial changes in microwave signatures of ice occur faster than those detected by the satellite sensor. There is a need for a layered two-dimensional surface roughness model of snow-covered sea ice that considers all mediating factors (e.g., air temperature, snow salinity, snow density, humidity, surface temperature, snow-ice interface water content, to name a few) responsible for passive microwave emission

detected by the satellite sensor. Sub-pixel (< 5.4 km) evaluation of sea ice roughness using AMSR-E (or any passive microwave satellite) is marred by spatial and temporal inconsistencies in various datasets meant to account for sea ice microwave signatures and its physical attributes. The development of such a model would enable unprecedented predictions of sea ice roughness conditions from a spaceborne platform, providing regional spatial coverage, ideal for understanding MIZ behavior of the Arctic.

Future challenges in estimating MIZ roughness could be the following:

- Sub-pixel (< 5.4 km for passive) interpretation of passive microwave emission of MIZ
- Integrating active and passive microwave response of annual changes in ice surface roughness in the MIZ in a thermodynamic model
- Identification and classification of ice types at high spatial (sub-meter) and temporal resolutions using combined active and passive satellite data
- Acquisition of required synchronized high resolution 2D laser and SAR data from the same ice/surface type for various surface types
- Quantifying the relationship between changing surface properties and bottom ice roughness
- Parameterizing ice motion and underwater current contributions to surface roughness
- The development of a reliable remote sensing-based wind retrieval technique over sea ice is also an open area of research as wind is the dominant factor related to roughness

- I did not consider the effect of surface roughness anisotropy on backscatter/emission (i.e. dependence of backscatter/emission on the direction of measurement)
- There is a need for 2D high-resolution measurements of surface roughness at the same spatial and temporal scales at which microwave signatures of MIZ occur
- A well-designed fully polarimetric microwave data acquisition considering dependence of measurement direction on backscatter at various spatial and temporal scales, synchronized with other measurements, is required

The understanding of the MIZ physical mechanisms will considerably improve once these issues are addressed.

Appendix–A: Contributions of Authors to Journal Papers

Chapter-3

In this journal paper, I extensively collected ship-based laser data using University of Miami's laser system, with help from Dustin Isleifson and Randall Scharien in deployment and recuperation of instrument. CFL team collected helicopter-based laser data. I collected ship-based passive microwave data at 37 and 89 GHz. I formulated the key scientific objectives of the paper; the ideas for plots, graphs, tables, and presentation style were my own. Dustin Isleifson provided backscattering coefficients data for November 2007 from University of Manitoba's scatterometer. Randall Scharien provided backscattering coefficients data for June–July 2008 from University of Calgary's scatterometer. I performed the statistical data analyses of active and passive microwave and laser data (ship- and helicopter-based). I developed a suite of MATLAB® codes for filtering, cleaning, and presenting the ship- and helicopter-based laser data. I created all the figures using Ocean Data View, SigmaPlot®, and JMP®. David Barber provided expertise, logistical and financial support for the fieldwork, and useful comments on the manuscript. I wrote the manuscript, and handled it as the corresponding author until the final publication. Dustin Isleifson and Randall Scharian also provided useful comments on the manuscript.

Chapter-4

In this paper, I formulated the key concepts and scientific objectives. I conceptualized and developed the two-dimensional model, and derived mathematical formula for circular coherence. CFL team collected the backscattering data for November 2007 using University of Manitoba's scatterometer and took field photographs of various ice types. Randall Scharien provided Figure 4.5 and Figure 4.6; and Table 4.3 and Table 4.4. I created most figures and tables using Ocean Data View, and MATLAB®. David Barber provided expertise, logistical and financial support for the fieldwork, and useful comments on the manuscript. I wrote the manuscript, and handled it as the corresponding author until the final publication. Randall Scharien wrote a section on scatterometer methodology, helped with the analysis and presentation of the data, and provided useful comments on the manuscript.

Chapter-5

In this paper, I conceptualized the scientific objectives. I extensively collected the buoy data with helps from CFL project team and Canadian Coast Guard personnel in deployment and recuperation of the buoy. I collected ship-based passive microwave data at 37 and 89 GHz channels and scatterometer data for July 2008 using University of Manitoba's scatterometer. I analyzed and processed all wave data and created most figures using Ocean Data View, SigmaPlot®, MATLAB®, and W@ves21. The statistical data analysis, processing, and interpretation of all passive microwave data were my own. Randall Scharien provided Figure 5.6, Figure 5.7, and Figure 5.8 and a part of Table 5.2; helped with discussion, processing, and interpretation of polarimetric data; and wrote a

section on scatterometer methodology. I wrote the manuscript, and handled it as the corresponding author until the final publication. David Barber provided expertise, logistical and financial support for the fieldwork, and valuable comments on the manuscript.

Chapter-6

In this paper, I formulated the key concepts and the scientific objectives. CFL team collected the helicopter-based roughness data. I acquired the AMSR-E data from NSIDC. The processing and analysis of all laser data and AMSR-E data are my own. I developed the MATLAB® codes for helicopter-based laser data filtering and analysis. I created all the figures using Ocean Data View, MATLAB®, SPSS®, and Panoply. David Barber provided expertise, discussions, logistical and financial support for the fieldwork, and valuable comments on the manuscript. I wrote the manuscript, and handled it as the corresponding author until the final publication.

Appendix–B: Additional Contributions to the Scientific Literature

In addition to the four peer-reviewed journal papers embodied in this thesis, I have contributed to several other peer-reviewed journal papers, data reports, and a book chapter during the course of my Ph.D. work. This work is closely related to my thesis, but is considered more as a contribution to the collaborative research at CEOS resulting from my collaboration in multidisciplinary teamwork during CFL project and ArcticNet field programs in the Arctic.

Journal Papers:

1. Scharien, R. K., Yackel, J. J., Barber, D. G., Asplin, M., **Gupta, M.**, and Isleifson, D. (2012). Geophysical controls on C band polarimetric backscatter from melt pond covered Arctic first-year sea ice: Assessment using high-resolution scatterometry. *Journal of Geophysical Research*, 117(C00G18), doi:10.1029/2011JC007353.

2. Barber, D. G., Galley, R., Asplin, M. G., De Abreu, R., Warner, K. -A., Pućko, M., **Gupta, M.**, Prinsenberg, S., and Julien, S. (2009). Perennial pack ice in the southern Beaufort Sea was not as it appeared in the summer of 2009. *Geophysical Research Letters*, 36(24), doi:10.1029/2009GL041434.

Book Chapter:

3. Barber, D. G., Asplin, M. G., Lukovich, J., Galley, R., Scharien, R., Isleifson, D., Candlish, L., Raddatz, R., Prinsenberg, S., Iacozza, J., **Gupta, M.**, Hochheim, K., and Mundy, C. J., Section 3.2: Ocean-Sea Ice-Atmosphere Interactions. In: Barber, D. G., Tjaden, T., Leitch, D., Barber, L., and Chan, W. (Eds.) (2012), In: *On the*

edge: From knowledge to action during the fourth International Polar Year Circumpolar Flaw Lead System Study (2007-2008). ©2012 University of Manitoba, 248 p., ISBN 978-0-9813265-1-1. [pdf]

Data Reports:

4. **Gupta, M.** (2013). Sections: Passive Microwave Measurement; MOB sampling. In: *ArcticNet 2013 Expedition of the CCGS Amundsen: Data Report*, Warner, K. (Ed.), pp. 112–113, 117–118.

5. **Gupta, M.** (2012). Section 3.3 Ocean Surface Roughness; Section 5.7 On-ice Micromet Tower. In: *ArcticNet 2011 Expedition of the CCGS Amundsen: Data Report*, Asplin, M, and Scharien, R. (Eds.), CEOS-TEC-2012-01-25, pp. 36–38, 132–136.

6. **Gupta, M.** (2009). Section 3.3 Ocean Surface Roughness; Section 4.3 Surface-Based Radiometer (SBR) Passive Microwave Measurements. In: *CCGS Amundsen 2009 Field Program: ArcticNet / IOL Partnership Met/Ocean Data Report, 2009*, Asplin, M, and Candlish, L. (Eds.), CEOS-TEC-2009-12-05, pp. 62–64, 92–95.

References

Alam, A., and Curry, J. A. (1997). Determination of surface turbulent fluxes over leads in Arctic sea ice. *Journal of Geophysical Research*, 102 (C2), 3331–3343, doi:10.1029/96JC03606.

Alpers, W. R., Ross, D. B., and Rufenach, C. L. (1981). On the detectability of ocean surface waves by real and synthetic aperture radar. *Journal of Geophysical Research*, 86, 6481–6498, doi:10.1029/JC086iC07p06481.

Anderson, R. J. (1993). A study of wind stress and heat flux over the open ocean by the inertial-dissipation method. *Journal of Physical Oceanography*, 23, 2153–2161, doi:10.1175/1520-0485(1993)023<2153:ASOWSA>2.0.CO;2.

Andreas, E. L. (1987). A theory for the scalar roughness and the scalar transfer coefficients over snow and sea ice. *Boundary-Layer Meteorology*, 38, 159–184, doi:10.1007/BF00121562.

Andreas, E. L. (1992). Sea spray and the turbulent air-sea heat fluxes. *Journal of Geophysical Research*, 97 (C7), 11 429–11 441, doi:10.1029/92JC00876.

Andreas, E. L., and Claffey, K. J. (1995). Air–ice drag coefficients in the western Weddell Sea: 1. Values deduced from profile measurements. *Journal of Geophysical Research*, 100(C3), 4821–4831, doi:10.1029/94JC02015.

Andreas, E. L., Horst, T. W., Grachev, A. A., Persson, P. O. G., Fairall, C. W., Guest, P. S., and Jordan, R. E. (2010). Parameterizing turbulent exchange over summer sea ice and the marginal ice zone. *Quarterly Journal of the Royal Meteorological Society*, 136, 927–943, doi: 10.1002/qj.618.

Arai, K. (2011). Comparative study of polarimetric SAR classification methods including proposed method with maximum curvature of trajectory of back scattering cross section in ellipticity and orientation angle space. *International Journal of Research and Reviews in Computer Science*, 2(4), 1005–1009. [pdf]

Arya, S. P. S. (1973). Contribution of form drag on pressure ridges to the air stress on Arctic ice. *Journal of Geophysical Research*, 78(30), 7092–7099, doi:10.1029/JC078i030p07092.

Arya, S. P. S. (1975). A drag partition theory for determining the large-scale roughness parameter and wind stress on the Arctic pack ice. *Journal of Geophysical Research*, 80(24), 3447–3454, doi:10.1029/JC080i024p03447.

Ashcroft, P., and Wentz, F. J. (2013). Updated daily. AMSR-E/Aqua L2A Global Swath Spatially-Resampled Brightness Temperatures. Version 3. Boulder, Colorado USA: NASA DAAC at the National Snow and Ice Data Center. doi:10.5067/AMSR-E/AE_L2A.003.

Asplin, M. G., Galley, R., Barber, D. G., and Prinsenberg, S. (2012). Fracture of summer perennial sea ice by ocean swell as a result of Arctic storms. *Journal of Geophysical Research*, 117, C06025, doi:10.1029/2011JC007221.

Barber, D. G. (2005). Microwave remote sensing, sea ice and arctic climate. *Physics in Canada* 61: 105–111. [pdf]

Barber, D. G., Asplin, M. G., Gratton, Y., Lukovich, J. V., Galley, R. J., Raddatz, R. L., and Leitch, D. (2010). The international polar year (IPY) circumpolar flaw lead (CFL) system study: Overview and the physical system. *Atmosphere-Ocean,* 48(4), 225–243, doi:10.3137/OC317.2010.

Barber, D. G., Fung, A. K., Grenfell, T. C., Nghiem, S. V., Onstott, R. G., Lytle, V. I., Perovich, D. K., Gow, A. J. (1998). The role of snow on microwave emission and scattering over first-year sea ice. *IEEE Transactions on Geoscience and Remote Sensing*, 36, 1750–1763, doi:10.1109/36.718643.

Barber, D. G., Galley, R., Asplin, M. G., DeAbreu, R., Warner, K. -A., Pućko, M., **Gupta, M.**, Prinsenberg, S., and Julien, S. (2009). Perennial pack ice in the southern Beaufort Sea was not as it appeared in the summer of 2009. *Geophysical Research Letters*, 36, L24501, doi:10.1029/2009GL041434.

Barber, D. G., and Hanesiak, J. M. (2004). Meteorological forcing of sea ice concentrations in the southern Beaufort Sea over the period 1979 to 2000. *Journal of Geophysical Research*, 109(C06014), doi:10.1029/2003JC002027.

Barber, D. G., and LeDrew, E. F. (1991). SAR sea ice discrimination using texture statistics: a multivariate approach. *Photogrammetric Engineering and Remote Sensing*, 57, 385–395. [pdf]

Barber, D. G., and Nghiem, S. V. (1999). The role of snow on the thermal dependence of microwave backscatter over sea ice. *Journal of Geophysical Research*, 104(C11), 25,789–25,803, doi:10.1029/1999JC900181.

Birnbaum, G., and Lupkes, C. (2002). A new parameterization of surface drag in the marginal sea ice zone. *Tellus*, 54(1), 107–123, doi:10.1034/j.1600-0870.2002.00243.x.

Brase, C. H., and Brase, C. P. (2009). *Understandable statistics- concepts and methods*. Houghton Mifflin Company: New York; 705 p. [pdf]

Campbell, W. J., Gloersen, P., Josberger, E. G., Johannessen, O. M., Guest, P. S., Mognard, N., Shuchman, R., Burns, B. A., Lannelongue, N., and Davidson, K. L. (1987). Variations of mesoscale and large-scale sea ice morphology in the 1984

marginal ice zone experiment as observed by microwave remote sensing. *Journal of Geophysical Research*, 92(C7), 6805–6824, doi:10.1029/JC092iC07p06805.

Carmack, E. C., and Macdonald, R. W. (2002). Oceanography of the Canadian shelf of the Beaufort Sea: A setting for marine life. *Arctic*, 55(1), 29–45. [pdf]

Carsey, F. D. (Ed). (1992). *Microwave Remote Sensing of Sea Ice*. American Geophysical Union, Washington, DC, USA. [pdf]

Cavalieri, D., Gloersen, P., and Campbell, W. J. (1984). Determination of sea ice parameters with the Nimbus 7 SMMR. *Journal of Geophysical Research*, 89(D4), 5355–5369, doi:10.1029/JD089iD04p05355.

Claussen, M. (1991). Local advection processes in the surface layer of the marginal ice zone. *Boundary-Layer Meteorology*, 54(1-2), 1–27, doi:10.1007/BF00119409.

Cloude, S. R., and Papathanassiou, K. P. (1999). Surface roughness and polarimetric entropy. *Geoscience and Remote Sensing Symposium IGARSS '99*. Proc. IEEE 1999 International : 2443–2445, doi:10.1109/IGARSS.1999.771537.

Cloude, S. R., and Pottier, E. (1996). A review of target decomposition theorems in radar polarimetry. *IEEE Transactions on Geoscience and Remote Sensing*, 34(2), 498–518, doi:10.1109/36.485127.

Comiso, J. C. (1986). Characteristics of Arctic winter sea ice from satellite multispectral microwave observations. *Journal of Geophysical Research: Oceans (1978–2012)*, 91(C1), 975–994, doi:10.1029/JC091iC01p00975.

Comiso, J. C. (1990). Arctic multiyear ice classification and summer ice cover using passive microwave satellite data. *Journal of Geophysical Research*, 95(C8), 13,411–14,422, doi:10.1029/JC095iC08p13411.

Comiso, J. C., Cavalieri, D. J., Markus, T. (2003). Sea ice concentration, ice temperature, and snow depth using AMSR-E data. *IEEE Transactions on Geoscience and Remote Sensing*, 41, 243–252, doi:10.1109/TGRS.2002.808317.

Comiso, J. C., Cavalieri, D. J., Parkinson, C. L., and Gloersen, P. (1997). Passive microwave algorithms for sea ice concentration: A comparison of two techniques. *Remote Sensing of Environment*, 60(3), 357–384, doi:10.1016/S0034-4257(96)00220-9.

Cox, C., and Munk, W. (1954). Measurement of the roughness of the sea surface from photographs of the Sun's glitter. *Journal of the Optical Society of America*, 44, 838–850, doi:10.1364/JOSA.44.000838.

Dammert, P. B. G., Lepparanta, M., and Askne, J. (1998). SAR interferometry over Baltic Sea ice. *International Journal of Remote Sensing*, 19, 3019–3037, doi:10.1080/014311698214163.

DeCosmo, J., Katsaros, K. B., Smith, S. D., Anderson, R. J., Oost, W. A., Bumke, K., Chadwick, H. (1996). Air-sea exchange of water vapor and sensible heat: The Humidity Exchange Over the Sea (HEXOS) results. *Journal of Geophysical Research*, 101, 12,001–12016, doi:10.1029/95JC03796.

Doble, M. J., and Bidlot, J. R. (2013). Wave buoy measurements at the Antarctic sea ice edge compared with an enhanced ECMWF WAM: Progress towards global waves-in-ice modelling. *Ocean Modelling*, 70, 166–173, doi:10.1016/j.ocemod.2013.05.012.

Donelan, M., Skafel, M., Graber, H., Liu, P., Schwab, D., and Venkatesh, S. (1992). On the growth rate of wind-generated waves. *Atmosphere-Ocean*, 30(3), 457–478, doi:10.1080/07055900.1992.9649449.

Drue, C., and Heinemann, G. (2002). Turbulence structures over the marginal ice zone under flow parallel to the ice edge: Measurements and parameterizations. *Boundary-Layer Meteorology*, 102(1), 83–116, doi:10.1023/A:1012776719250.

Edson, J. B., Fairall, C. W., Mestayer, P. G., and Larsen, S. E. (1991). A study of the inertial-dissipation method for computing air-sea fluxes. *Journal of Geophysical Research*, 96(C6), 10,689–10,711, doi:10.1029/91JC00886.

Eom, H. J., and Boerner, W. -M. (1991). Statistical properties of the phase difference between two orthogonally polarized SAR signals. *IEEE Transactions on Geoscience and Remote Sensing*, 29(1), 182–184, doi:10.1109/36.103312.

Esau, I. N. (2007). Amplification of turbulent exchange over wide Arctic leads: Large-eddy simulation study. *Journal of Geophysical Research*, 112(D08109), doi:10.1029/2006JD007225.

Farmer, L. D., Eppler, D. T., and Lohanick, A. W. (1990). Converting digital passive microwave radiances to Kelvin units of brightness temperatures. NORDA Technical Note 427, Naval Ocean Research and Development Activity, Stennis Space Center, Mississippi, 19 p. [pdf]

Fer, I., and Sundfjord, A. (2007). Observations of upper ocean boundary layer dynamics in the marginal ice zone. *Journal of Geophysical Research*, 112(C04012), doi:10.1029/2005JC003428.

Fissel, D. B., Marko, J. R., and Melling, H. (2008). Advances in upward looking sonar technology for studying the processes of change in Arctic Ocean ice climate. *Journal of Operational Oceanography*, 1, 9–18. [pdf]

Fortier, L., Pascal, S., Josee, M., and Barber, D. (2006). Survival of Arctic cod larvae (Boreogadus saida) in relation to sea ice and temperature in the Northeast Water

Polynya (Greenland Sea). *Canadian Journal of Fisheries and Aquatic Sciences*, 63(7), 1608–1616, doi:10.1139/F0.

Fujisaki, A., Yamaguchi, H., Toyota, T., Futatsudera, A., and Miyanaga, M. (2009). Measurements of air-ice drag coefficient over the ice-covered Sea of Okhotsk. *Journal of Oceanography*, 65, 487–498, doi:10.1007/s10872-009-0042-8.

Fung, A. K., and Chen, K. S. (2010). *Microwave Scattering and Emission Models for Users*, Artech House, Inc., Norwood, MA, USA, 430 p. [pdf]

Galley, R. J., Key, E., Barber, D. G., Hwang, B. J., and Ehn, J. K. (2008). Spatial and temporal variability of sea ice in the southern Beaufort Sea and Amundsen Gulf: 1980-2004. *Journal of Geophysical Research*, 113(C05S95), doi:10.1029/2007JC004553.

Garratt, J. R. (1992). The atmospheric boundary layer. Cambridge University Press, Cambridge, UK. 316 p. [pdf]

Geernaert, G. L. (Ed.) (1999). Air-sea exchange: Physics, chemistry and dynamics. Kluwer Academic Publishers, Dordrecht, The Netherlands, 578 p. [pdf]

Geldsetzer, T., Mead, J. B., Yackel, J. J., Scharien, R. K., and Howell, S. E. L. (2007). Surface-based polarimetric C-band scatterometer for field measurements of sea ice. *IEEE Transactions on Geoscience and Remote Sensing*, 45(11), 3405–3416, doi:10.1109/TGRS.2007.907043.

Geldsetzer, T., and Yackel, J. J. (2009). Sea ice type and open water discrimination using dual co-polarized C-band SAR. *Canadian Journal of Remote Sensing*, 35, 73–84, doi:10.5589/m08-075.

Gerling, W. T. (1986). Structure of the surface wind field from the Seasat SAR. *Journal of Geophysical Research*, 91, 2308–2320, doi:10.1029/JC091iC02p02308.

Germain, K. St., Poe, G. A., and Gaiser, P. W. (2002). Polarimetric emission model of the sea at microwave frequencies and comparison with measurements. *Progress In Electromagnetics Research*, 37, 1–30, [pdf]

Gloersen, P., Cavalieri, D. J., Chang, A. T. C., Wilheit, T. T., Campbell, W. J., Johannessen, O. M., Katsaros, K. B., Kunzi, K. F., Ross, D. B., Staelin, D., Windsor, E. P. L., Barath, F. T., Gudmundsen, P., and Ramseier, R. O. (1984). A summary of results from the first Nimbus-7 SMMR observations. *Journal of Geophysical Research*, 89(D4), 5335–5344, doi:10.1029/JD089iD04p05335.

Goebell, S. (2011). Comparison of coincident snow-freeboard and sea ice thickness profiles derived from helicopter-borne laser altimetry and electromagnetic induction sounding. *Journal of Geophysical Research*, 116(C08018), doi:10.1029/2009JC006055.

Grenfell, T. C. (1992). Surface-based passive microwave studies of multiyear sea ice. *Journal of Geophysical Research*, 97, 3485–3501, doi:10.1029/91JC02651.

Grenfell, T. C., Barber, D. G., Fung, A. K., Gow, A. J., Jezek, K. C., Knapp, E. J., Nghiem, S. V., Onstott, R. G., Perovich, D. K., Roesler, C. S., Swift, C. T., and Tanis, F. (1998). Evolution of electromagnetic signatures of sea ice from initial formation to the establishment of thick first-year ice. *IEEE Transactions on Geoscience and Remote Sensing*, 36(5), 1642–1654, doi:10.1109/36.718636.

Grenfell, T. C., and Lohanick, A. W. (1985). Temporal variations of the microwave signatures of sea ice during the late spring and early summer near Mould Bay, Northwest Territories. *Journal of Geophysical Research*, 90, 5063–5074, doi:10.1029/JC090iC03p05063.

Grody, N. (2008). Relationship between snow parameters and microwave satellite measurements: Theory compared with Advanced Microwave Sounding Unit observations from 23 to 150 GHz. *Journal of Geophysical Research*, 113, D22108, doi:10.1029/2007JD009685.

Gupta, M. (2013). Ph.D. Candidacy Examination, University of Manitoba.

Gupta, M., and Barber, D. G. (2014). Sub-pixel evaluation of sea ice roughness using AMSR-E data. *International Journal of Remote Sensing*, Manuscript# TRES-PAP-2014-0395 (*in review*)

Gupta, M., Barber, D. G., Scharien, R. K., and Isleifson, D. (2014). Detection and classification of surface roughness in an Arctic marginal sea ice zone. *Hydrological Processes*, 28, 599–609, doi:10.1002/hyp.9593.

Gupta, M., Scharien, R. K., and Barber, D. G. (2013). C-band polarimetric coherences and ratios for discriminating sea ice roughness. *International Journal of Oceanography*, 2013, Article ID 567182, 1–13, doi:10.1155/2013/567182.

Gupta, M., Scharien, R. K., and Barber, D. G. (2014). Microwave emission and scattering from ocean surface waves in the southern Beaufort Sea. *International Journal of Oceanography*, 2014, Article ID 872342, 1–12, doi:10.1155/2014/872342.

Haas, C., Lobach, J., Hendricks, S., Rabenstein, L., and Pfaffling, A. (2009). Helicopter-borne measurements of sea ice thickness, using a small and lightweight, digital EM system. *Journal of Applied Geophysics*, 67, 234–241, doi:10.1016/j.jappgeo.2008.05.005.

Hajnsek, I., Pottier, E., and Cloude, S. R. (2003). Inversion of surface parameters from polarimetric SAR. *IEEE Transactions on Geoscience and Remote Sensing*, 41(4), 727–744, doi:10.1109/TGRS.2003.810702.

Hall, R. T., and Rothrock, D. A. (1987). Photogrammetric observations of the lateral melt of sea ice floes. *Journal of Geophysical Research*, 92, 7045–7048, doi:10.1029/JC092iC07p07045.

Hallikainen, M., and Winebrenner, D. P. (1992). The physical basis for sea ice remote sensing. In *Microwave Remote Sensing of Sea Ice*, Carsey FD (ed). American Geophysical Union, Washington DC; 29–46. [pdf]

Hasselmann, K., and Hasselmann, S. (1991). On the nonlinear mapping of an ocean wave spectrum into a syhtetic aperture radar image spectrum and its inversion. *Journal of Geophysical Research*, 96 (C6), 10,713–10,729, doi:10.1029/91JC00302.

He, H., and Chen, D. (2011). Effects of surface wave breaking on the oceanic boundary layer. *Geophysical Research Letters*, 38(L07604), doi:10.1029/2011GL046665.

Hersbach, H. (2010). Comparison of C-band scatterometer CMOD5.N equivalent neutral winds with ECMWF. *Journal of Atmospheric and Oceanic Technology*, 27, 721–736, doi:10.1175/2009JTECHO698.1.

Hersbach, H., Stoffelen, A., and de Haan, S. (2007). An improved C-band scatterometer ocean geophysical model function: CMOD5. *Journal of Geophysical Research*, 112, C03006, doi:10.1029/2006JC003743.

Hibler, W. D. III. (1972). Removal of aircraft altitude variation from laser profiles of the Arctic ice pack. *Journal of Geophysical Research*, 77(36), 7190–7195, doi:10.1029/JC077i036p07190.

Hibler, W. D. III. (1975). Characterization of cold-regions terrain using airborne laser profilometry. *Journal of Glaciology*, 15(73), 329–347. [pdf]

Hibler, W. D. III. (1979). A dynamic thermodynamic sea ice model. *Journal of Physical Oceanography*, 9, 815–846, doi:10.1175/1520-0485(1979)009%3C0815:ADTSIM%3E2.0.CO;2.

Hibler, W. D. III (1989). Arctic ice-ocean dynamics. In: The Arctic Seas. Climatology, Oceanography, Geology, and Biology (Y. Herman, ed.). Van Nostrand Reiohold, New York, 47–91. 888 p. [pdf]

Hollinger, J. P. (1970). Passive microwave measurements of the sea surface. *Journal of Geophysical Research*, 75(27), 5209–5213, doi:10.1029/JC075i027p05209.

Hollinger, J. P. (1971). Passive microwave measurements of sea surface roughness. *IEEE Transactions on Geoscience Electronics*, GE-9, 165–169, doi:10.1109/TGE.1971.271489.

Hollinger, J. P., Lo, R., Poe, G., Savage, R., and Pierce, J. (1987). *Special Sensor Microwave/Imager User's Guide*. Naval Research Laboratory, Washington, DC.

Holmes, Q. A., Nüesch, D. R., and Shuchman, R. A. (1984). Textural analysis and real-time classification of sea-ice types using digital SAR data. *IEEE Transactions on Geoscience and Remote Sensing*, GE-22, 113–120, doi:10.1109/TGRS.1984.350602.

Holmes, J. F., Peacock, J. S., and Draper, D. C. (1994). Optical remote sensing of surface roughness through the turbulent atmosphere. *Applied Optics*, 33, 7770–7776, doi:10.1364/AO.33.007770.

Holthuijsen, L. H. (2007). Waves in oceanic and coastal waters. Cambridge University Press, Cambridge, UK. 387 p. [pdf]

Hong, S. (2010). Detection of small-scale roughness and refractive index of sea ice in passive satellite microwave remote sensing. *Remote Sensing of Environment*, 114, 1136–1140, doi:10.1016/j.rse.2009.12.015.

Hunkins, K. (1962). Waves on the Arctic Ocean. *Journal of Geophysical Research*, 67(6), 2477–2489, doi:10.1029/JZ067i006p02477.

Hutchings, J. K., and Rigor, I. G. (2012). Role of ice dynamics in anomalous ice conditions in the Beaufort Sea during 2006 and 2007. *Journal of Geophysical Research*, 117(C00E04), doi:10.1029/2011JC007182.

Hwang, P. A., Sletten, M. A., and Toporkov, J. V. (2008). Analysis of radar sea return for breaking wave investigation. *Journal of Geophysical Research*, 113(C02003), doi:10.1029/2007JC004319.

Isleifson, D., Hwang, B., Barber, D. G., Scharien, R. K., and Shafai, L. (2010). C-band polarimetric backscattering signatures of newly formed sea ice during fall-freeze up. *IEEE Transactions on Geoscience and Remote Sensing*, 48(8), 3256–3267, doi:10.1109/TGRS.2010.2043954.

Ivanov, B. V., Gerland, S., Winther, J. -G., and Goodwin, H. (2003). Energy exchange processes in the marginal ice zone of the Barents Sea, Arctic Ocean, during spring 1999. *Journal of Glaciology*, 49(166), 415–419, doi:10.3189/172756503781830557.

Janssen, P. A. E. M. (1989). Wave-induced stress and the drag of air flow over sea waves. *Journal of Physical Oceanography*, 19,745–754, doi:10.1175/1520-0485(1989)019%3C0745:WISATD%3E2.0.CO;2.

Johnsen, H., Engen, G., and Guitton, G. (2008). Sea-surface polarization ratio from Envisat ASAR AP data. *IEEE Transactions on Geoscience and Remote Sensing*, 46(11), 3637–3646, doi:10.1109/TGRS.2008.2001061.

Jones, W. L., and Schroeder, L. C. (1978). Radar backscatter from the ocean: dependence on surface friction velocity. *Boundary-Layer Meteorology*, 13, 133–149, doi:10.1007/BF00913867.

Karaev, V. Y., Kanevsky, M. B., and Meshkov, E. M. (2011). Measuring the parameters of sea-surface roughness by underwater acoustic systems: Discussion of the device concept. *Radiophysics and Quantum Electronics*, 53, 569–579, doi:10.1007/s11141-011-9251-2.

Keller, W. C., Plant, W. J., and Weissman, D. E. (1985). The dependence of X band microwave sea return on atmospheric stability and sea state. *Journal of Geophysical Research*, 90(C1), 1019–1029, doi:10.1029/JC090iC01p01019.

Keller, W. C., Wismann, V., and Alpers, W. (1989). Tower-based measurements of the ocean C band radar backscattering cross section. *Journal of Geophysical Research*, 94, 924–930, doi:10.1029/JC094iC01p00924.

Ketchum, R. D. Jr. (1971). Airborne laser profiling of the arctic pack ice. *Remote Sensing of Environment*, 2, 41–52, doi:10.1016/0034-4257(71)90076-9.

Kim, J. -W., Kim, D. -J., and Hwang, B. J. (2012). Characterization of Arctic sea ice thickness using high-resolution spaceborne polarimetric SAR data. *IEEE Transactions on Geoscience and Remote Sensing*, 50(1), 13–22, doi:10.1109/TGRS.2011.2160070.

Kitaigorodskii, S. A. (1962). Applications of the theory of similarity to the analysis of wind-generated wave motion as a stochastic process. *Bulletin Academy of Sciences, USSR Geophysics Series*, 1, 105–117. [pdf]

Komarov, A. S., Zabeline, V., and Barber, D. G. (2014). Ocean surface wind speed retrieval from C-band SAR images without input of wind direction. *IEEE*

Transactions on Geoscience and Remote Sensing, 52(2), 980–990, doi:10.1109/TGRS.2013.2246171.

Kong, J. A., Shin, R., Shiue, J. C., Tsang, L. (1979). Theory and experiment for passive microwave remote sensing of snowpacks. *Journal of Geophysical Research*, 84, 5669–5673, doi:10.1029/JB084iB10p05669.

Kravtsov, Y. A., and Churyumov, A. N. (2000). Contribution of steep irregularities to the radio-brightness temperature of the ocean. *Radiophysics and Quantum Electronics*, 43, 196–201, doi:10.1007/BF02677183.

Kudryavtsev, V. N. (1997). Physical model of the spectrum of capillary-gravity waves. *Physical Oceanography*, 8(2), 69–80, doi:10.1007/BF02523059.

Kudryavtsev, V., Hauser, D., Caudal, G., and Chapron, B. (2003a). A semiempirical model of the normalized radar cross-section of the sea surface 1. Background model. *Journal of Geophysical Research*, 108 (C3), FET 2-1–FET 2-24, doi:10.1029/2001JC001003.

Kudryavtsev, V., Hauser, D., Caudal, G., and Chapron, B. (2003b). A semiempirical model of the normalized radar cross-section of the sea surface 2. Radar modulation transfer function. *Journal of Geophysical Research*, 108 (C3), FET 3-1–FET 3-16, doi:10.1029/2001JC001004.

Kudryavtsev, V. N., Makin, V. K., Chapron, B. (1999). Coupled sea surface-atmosphere model. 2. Spectrum of short wind waves. *Journal of Geophysical Research*, 104 (C4), 7625–7639, doi:10.1029/1999JC900005.

Kwok, R., and Cunningham, G. F. (2010). Contribution of melt in the Beaufort Sea to the decline in Arctic multiyear sea ice coverage: 1993-2009. *Geophysical Research Letters*, 37(L20501), doi:10.1029/2010GL044678.

Kwok, R., Cunningham, G. F., Zwally, H. J., and Yi, D. (2007). Ice, cloud, and land elevation satellite (ICESat) over Arctic sea ice: Retrieval of freeboard. *Journal of Geophysical Research*, 112, C12013, doi:10.1029/2006JC003978.

Kwok, R., Rignot, E., Holt, B., and Onstott, R. (1992). Identification of sea ice types in spaceborne synthetic aperture radar data. *Journal of Geophysical Research*, 97, 2391–2402, doi:10.1029/91JC02652.

Kwok, R., and Rothrock, D. A. (2009). Decline in Arctic sea ice thickness from submarine and ICESat records: 1958–2008. *Geophysical Research Letters*, 36(L15501), doi:10.1029/2009GL039035.

Lavoie, D., Macdonald, R. W., and Denman, K. L. (2009). Primary productivity and export fluxes on the Canadian shelf of the Beaufort Sea: A modelling study. *Journal of Marine Systems*, 75(1-2), 17–32, doi:10.1016/j.jmarsys.2008.07.007.

Leavitt, E. (1980). Surface-based air stress measurements made during AIDJEX, in Sea–Ice Processes and Models, edited by R. S. Pritchard, 419–429, Univ. of Wash. Press, Seattle. [pdf]

Lee, J. -S., Schuler, D. L., and Ainsworth, T. L. (2000). Polarimetric SAR data compensation for terrain azimuth slope variation. *IEEE Transactions on Geoscience and Remote Sensing*, 38, 2153–2163, doi:10.1109/36.868874.

Lee, J. -S., Schuler, D. L., Ainsworth, T. L., Krogager, E., Kasilingam, D., and Boerner, W. -M. (2002). On the estimation of radar polarization orientation shifts induced by terrain slopes. *IEEE Transactions on Geoscience and Remote Sensing*, 40(1), 30–41, doi:10.1109/36.981347.

Lee, J. -S., Yeuh, S. H., and Schuler, D. L. (2004). Polarimetric analysis of scatterometer data for ocean surface wind measurement. In *Geoscience and Remote Sensing Symposium Proceedings*, IGARSS '04, 20–24, Anchorage, AK, USA, doi:10.1109/IGARSS.2004.1368996.

Leppäranta, M. (2005). The Drift of Sea Ice, Springer, Berlin, 266 p. [pdf]

Livingstone, C. E., Gray, A. L., and Singh, K. P. (1987). Seasonal and regional variations of active/passive microwave signatures of sea ice. *IEEE Transactions on Geoscience and Remote Sensing*, GE-25, 159–173, doi:10.1109/TGRS.1987.289815.

Lohanick, A. W. (1990). Some observations of established snow cover on saline ice and their relevance to microwave remote sensing. In: Sea Ice Properties and Processes, edited by S. F. Ackley and W. W. Weeks, CRREL Monograph 90-1, Cold Regions Research and Engineering Laboratory, Hanover, New Hampshire, 61–67.

Lohanick, A. W., and Grenfell, T. C. (1986). Variations in brightness temperature over cold first-year sea ice near Tuktoyaktuk, Northwest Territories. *Journal of Geophysical Research*, 91(C4), 5133–5144, doi:10.1029/JC091iC04p05133.

Longuet-Higgins, M. S. (1957). The statistical analysis of a random, moving surface. *Philosophical Transactions of the Royal Society of London, Series A, Mathematical and Physical Sciences*, 249, 321–387. [pdf]

Lu, P., and Li, Z. (2010). A method of obtaining ice concentration and floe size from shipboard oblique sea ice images. *IEEE Transactions on Geoscience and Remote Sensing*, 48, 2771–2780, doi:10.1109/TGRS.2010.2042962.

Lu, P., Li, Z. J., Zhang, Z. H., and Dong, X. L. (2008). Aerial observations of floe size distribution in the marginal ice zone of summer Prydz Bay. *Journal of Geophysical Research*, 113(C02011), doi:10.1029/2006JC003965.

Lukovich, J. V., and Barber, D. G. (2005). On sea ice concentration anomaly coherence in the southern Beaufort Sea. Geophysical Research Letters, 32(L10705), doi:10.1029/2005GL022737.

Makin, V. K., and Kudryavtsev, V. N. (1999). Coupled sea surface-atmosphere model 1. Wind over waves coupling. *Journal of Geophysical Research*, 104 (C4), 7613–7623, doi:10.1029/1999JC900006.

Makin, V. K., and Mastenbroek, C. (1996). Impact of wave on air-sea exchange of sensible heat and momentum. *Boundary-Layer Meteorology*, 79, 279–300, doi:10.1007/BF00119442.

Manes, C., Guala, M., Lowe, H., Bartlett, S., Egli, L., and Lehning, M. (2008). Statistical properties of fresh snow roughness. *Water Resources Research*, 44, W11407, doi:10.1029/2007WR006689.

Manninen, A. T. (1997). Surface roughness of Baltic sea ice. *Journal of Geophysical Research*, 102(C1), 1119–1139, doi:10.1029/96JC02991.

Martin, S., and Kauffman, P. (1981). A field and laboratory study of wave damping by grease ice. *Journal of Glaciology*, 27(96), 283–313. [pdf]

Martin, T., Steele, M., and Zhang, J. (2014), Seasonality and long-term trend of Arctic Ocean surface stress in a model, *Journal of Geophysical Research-Oceans*, 119, doi:10.1002/2013JC009425.

Mattia, F., Toan, T. L., Souyris, J. -C., Carolis, C. D., Floury, N., Posa, F., and Pasquariello, N. G. (1997). The effect of surface roughness on multifrequency polarimetric SAR data. *IEEE Transactions on Geoscience and Remote Sensing*, 35(4), 954–966, doi:10.1109/36.602537.

Maykut, G. A. (1978). Energy exchange over young sea ice in the central Arctic. *Journal of Geophysical Research*, 83(C7), 3646–3658, doi:10.1029/JC083iC07p03646.

Maykut, G. A. (1986). The surface heat and mass balance. In: The Geophysics of Sea Ice (ed. N. Untersteiner), Plenum, New York, 395–464. [pdf]

McPhee, M. G. (2002). Turbulent stress at the ice/ocean interface and bottom surface hydraulic roughness during the SHEBA drift. *Journal of Geophysical Research*, 107(C10), 8037, doi:10.1029/2000JC000633.

McPhee, M. G., Morison, J. H., and Nilsen, F. (2008). Revisiting heat and salt exchange at the ice-ocean interface: Ocean flux and modeling considerations. *Journal of Geophysical Research*, 113(C06014), doi:10:1029/2007JC004383.

Meissner, T., and Wentz, F. J. (2012). The emissivity of the ocean surface between 6–90 GHz over a large range of wind speeds and earth incidence angles. *IEEE Transactions on Geoscience and Remote Sensing*, 50(8), 3004–3026, doi:10.1109/TGRS.2011.2179662.

Melling, H. (1998). Detection of features in first-year pack ice by synthetic aperture radar (SAR). *International Journal of Remote Sensing*, 19, 1223–1249, doi:10.1080/014311698215702.

Miles, J. W. (1957). On the generation of surface waves by shear flow. *Journal of Fluid Mechanics*, 3, 185–204, doi:10.1017/S0022112057000567.

Monahan, E. C., and O'Muircheartaigh, I. G. (1986). Whitecaps and the passive remote sensing of the ocean surface. *International Journal of Remote Sensing*, 7, 627–642, doi:10.1080/01431168608954716.

Moore, C. W., Obrist, D., Steffen, A., Staebler, R. M., Douglas, T. A., Richter, A., and Nghiem, S. V. (2014). Convective forcing of mercury and ozone in the Arctic boundary layer induced by leads in sea ice. *Nature*, 506(7486), 81–84, doi:10.1038/nature12924.

Moskowitz, L. (1964). Estimates of the power spectrums for fully developed seas for wind speeds of 20 to 40 knots. *Journal of Geophysical Research*, 69(24), 5161–5179, doi:10.1029/JZ069i024p05161.

Mouche, A. A., Hauser, D., Daloze, J. -F., and Guerin, C. (2005). Dual-polarization measurements at C-band over the ocean: results from airborne radar observations and comparison with ENVSAT ASAR data. *IEEE Transactions on Geoscience and Remote Sensing*, 43, 753–769, doi:10.1109/TGRS.2005.843951.

Mushkin, A., and Gillespie, A. R. (2005). Estimating sub-pixel surface roughness using remotely sensed stereoscopic data. *Remote Sensing Environment*, 99, 75–83, doi:10.1016/j.rse.2005.02.018.

Nakamura, K., Wakabayashi, H., Naoki, K., Nishio, F., Moriyama, T., and Uratsuka, S. (2005). Observation of sea-ice thickness in the sea of Okhotsk by using dual-frequency and fully polarimetric airborne SAR (Pi-SAR) data. *IEEE Transactions on Geoscience and Remote Sensing*, 43, 2460–2469, doi:10.1109/TGRS.2005.853928.

Nghiem, S. V., and Bertoia, C. (2001). Study of multi-polarization C-band backscatter signatures for Arctic sea ice mapping with future satellite SAR: Ice and icebergs. *Canadian Journal Remote Sensing*, 27, 387–402. [pdf]

Nghiem, S. V., Kwok, R., Yueh, S. H., and Drinkwater, M. R. (1995). Polarimetric signatures of sea ice 2. Experimental observations. *Journal of Geophysical Research*, 100(C7), 13681–13698, doi:10.1029/95JC00938.

Nghiem, S. V., Rigor, I. G., Perovich, D. K., Clemente-Colón, P., Weatherly, J. W., and Neumann, G. (2007). Rapid reduction of Arctic perennial sea ice. *Geophysical Research Letters*, 34(L19504), doi:10.1029/2007GL031138.

Nghiem, S. V., Yueh, S. H., Kwok, R., and Li, F. K. (1992). Symmetry properties in polarimetric remote sensing. *Radio Science*, 27(5), 693–711, doi:10.1029/92RS01230.

Nolin, A. W., Fetterer, F. M., and Scambos, T. A. (2002). Surface roughness characterizations of sea ice and ice sheets: Case studies with MISR data. *IEEE Transactions on Geoscience and Remote Sensing*, 40, 1605–1615, doi:10.1109/TGRS.2002.801581.

Nordberg, W., Conaway, J., Ross, D. B., and Wilheit, T. (1971). Measurements of microwave emission from a foam-covered, wind-driven sea. *Journal of the Atmospheric Sciences*, 28, 429–435, doi:10.1175/1520-0469(1971)028%3C0429:MOMEFA%3E2.0.CO;2.

Ogilvy, J. A. (1991). Theory of Wave Scattering from Random Rough Surfaces. Adam Hilger. 277 p. [pdf]

Ogilvy, J. A., and Foster, J. R. (1989). Rough surfaces: Gaussian or exponential statistics? *Journal of Physics D: Applied Physics*, 22, 1243–1251, doi:10.1088/0022-3727/22/9/001.

Onstott, R. G., Grenfell, T. C., Matzler, C., Luther, C. A., and Svendsen, E. A. (1987). Evolution of microwave sea ice signatures during early summer and midsummer in the marginal ice zone. *Journal of Geophysical Research*, 92(C7), 6825–6835, doi:10.1029/JC092iC07p06825.

Overeem, I., Anderson, R. S., Wobus, C. W., Clow, G. D., Urban, F. E., and Matell, N. (2011). Sea ice loss enhances wave action at the Arctic coast. *Geophysical Research Letters*, 38, L17503, doi:10.1029/2011GL048681.

Pandey, P. C., and Kakar, R. K. (1982). An empirical microwave emissivity model for a foam-covered sea. *IEEE Journal of Oceanic Engineering*, OE-7(3), 135–140, doi:10.1109/JOE.1982.1145527.

Parkinson, C. L., Comiso, J. C., Zwally, H. J., Cavalieri, D. J., Gloersen, P., and Campbell, W. J. (1987). Arctic Sea Ice, 1973–1976: Satellite passive-microwave observations, NASA SP-489, National Aeronautics and Space Administration, Washington, DC.

Perovich, D. K., Longacre, J., Barber, D. G., Maffione, R. A., Cota, G. F., Mobley, C. D., Gow, A. J., Onstott, R. G., Grenfell, T. C., Pegau, W. S., Landry, M., and Roesler, C. S. (1998). Field observations of the electromagnetic properties of first-year sea ice. *IEEE Transactions on Geoscience and Remote Sensing*, 36(5), 1705–1715, doi:10.1109/36.718639.

Perovich, D. K., Tucker, W. B. III, Krishfield, R. A. (1989). Oceanic heat flux in the Fram Strait measured by a drifting buoy. *Geophysical Research Letters*, 16, 995–998, doi:10.1029/GL016i009p00995.

Perrie, W., and Hu, Y. (1996). Air-ice ocean momentum exchange. Part I: Energy transfer between waves and ice floes. *Journal of Physical Oceanography*, 26(9), 1705–1720, doi:10.1175/1520-0485(1996)026%3C1705:AMEPTB%3E2.0.CO;2.

Phillips, O. M. (1985). Spectral and statistical properties of the equilibrium range in the wind-generated gravity waves. *Journal of Fluid Mechanics*, 156, 505–531, doi:10.1017/S0022112085002221.

Phillips, O. M. (1988). Radar returns from the sea surface- Bragg scattering and breaking waves. *Journal of Physical Oceanography*, 18, 1065–1074, doi:10.1175/1520-0485(1988)018%3C1065:RRFTSS%3E2.0.CO;2.

Pizzolato, L., Howell, S. E. L., Derksen, C., Dawson, J., and Copland, L. (2014). Changing sea ice conditions and marine transportation activity in Canadian Arctic waters between 1990 and 2012. *Climatic Change*, 1–13, doi:10.1007/s10584-013-1038-3.

Plant, W. J. (1990). Bragg scattering of electromagnetic waves from the air/sea interface. In: Surface Waves and Fluxes: Current Theory and Remote Sensing, G.L. Geernaert and W.J. Plant (Eds.), Kluwer Academic Publishers, 2, 41–108. [pdf]

Prinsenberg, S. J., Baaren, A. V. D., and Peterson, I. K. (2006). Ice ridging and ice drift in sourthern Gulf of St Lawrence, Canada, during winter storms. *Annals of Glaciology*, 44, 411–417, doi:10.3189/172756406781811439.

Rignot, E., and Drinkwater, M. R. (1994). Winter sea-ice mapping from multi-parameter synthetic-aperture radar data. *Journal of Glaciology*, 40, 31–45. [pdf]

Rivas, M. B., Maslanik, J. A., Sonntag, J. G., and Axelrad, P. (2006). Sea ice roughness from airborne LIDAR profiles. *IEEE Transactions on Geoscience and Remote Sensing*, 44 (11), 3032–3037, doi:10.1109/TGRS.2006.875775.

Rufenach, C. L., and Alpers, W. R. (1978). Measurements of ocean wave heights using the Geos 3 altimeter. *Journal of Geophysical Research*, 83(C10), 5011–5018, doi:10.1029/JC083iC10p05011.

Scharien, R. K., Yackel, J. J., Barber, D. G., Asplin, M., **Gupta, M.**, and Isleifson, D. (2012). Geophysical controls on C band polarimetric backscatter from melt pond

covered Arctic first-year sea ice: Assessment using high-resolution scatterometry. *Journal of Geophysical Research*, 117(C00G18), doi:10.1029/2011JC007353.

Schuler, D. L., Lee, J. -S., Kasilingam, D., and Nesti, G. (2002). Surface roughness and slope measurements using polarimetric SAR data. *IEEE Transactions on Geoscience and Remote Sensing*, 40, 687–698, doi:10.1109/TGRS.2002.1000328.

Shen, H. H., Hibler, W. D. III, and Lepparanta, M. (1987). The role of ice floe collisions in sea ice rheology. *Journal of Geophysical Research*, 92(C7), 7085–7096, doi:10.1029/JC092iC07p07085.

Shifrin, K. S. (2001). An algorithm for determining the radiance reflected from the rough sea surface using MODIS-N satellite radiometer data. *IEEE Transactions on Geoscience and Remote Sensing*, 39, 677–681, doi:10.1109/36.911124.

Shirasawa, K., and Ingram, R. G. (1997). Currents and turbulent fluxes under the first - year sea ice in Resolute Passage, Northwest Territories, Canada, *Journal of Marine Systems*, 11, 21–32, doi:10.1016/S0924-7963(96)00024-3.

Smith, W. O. Jr., and Barber, D. G., Eds. (2007). *Polynyas: Windows to the World*, Elsevier, Amsterdam, The Netherlands, 474 p. [pdf]

Spreen, G., Kaleschke, L., and Heygster, G. (2008). Sea ice remote sensing using AMSR- E 89- GHz channels. *Journal of Geophysical Research: Oceans (1978–2012)*, 113(C02S03), doi:10.1029/2005JC003384.

Squire, V. A., Dugan, J. P., Wadhams, P., Rottier, P. J., Liu, A. K. (1995). Of ocean waves and sea ice. *Annual Review of Fluid Mechanics*, 27, 115–168, doi:10.1146/annurev.fl.27.010195.000555.

Squire, V. A., and Moore, S. C. (1980). Direct measurement of the attenuation of ocean waves by pack ice. *Nature*, 253, 365–368, doi:10.1038/283365a0.

Squire, V. A., Vaughan, G. L., and Bennetts, L. G. (2009). Ocean surface wave evolvement in the Arctic Basin. *Geophysical Research Letters*, 36, L22502, doi:10.1029/2009GL040676.

Steiner, N., Harder, M., and Lemke, P. (1999). Sea-ice roughness and drag coefficients in a dynamic-thermodynamic sea-ice model for the Arctic. *Tellus*, 51A, 964–978, doi:10.1034/j.1600-0870.1999.00029.x.

Stewart, R. H. (2009). Introduction to physical oceanography. University Press of Florida, 353 p. [pdf]

Stirling, I., Lunn, N. J., Iacozza, J., Elliott, C., and Obbard, M. (2004). Polar bear distribution and abundance on the Southwestern Hudson Bay coast during open water season, in relation to population trends and annual ice patterns. *Arctic,* 57(1), 15–26, [pdf].

Stoffelen, A., and Anderson, D. (1997). Scatterometer data interpretation: measurement space and inversion. *Journal of Atmospheric and Oceanic Technology*, 14, 1298–1313, doi:10.1175/1520-0426(1997)014%3C1298:SDIMSA%3E2.0.CO;2.

Stogryn, A. (1972). The emissivity of sea foam at microwave frequencies. *Journal of Geophysical Research*, 77(9), 1658–1666, doi:10.1029/JC077i009p01658.

Stroeve, J. C., Markus, T., Boisvert, L., Miller, J., and Barrett, A. (2014). Changes in Arctic melt season and implications for sea ice loss. *Geophysical Research Letters*, 41, doi:10.1002/2013GL058951.

Stroeve, J. C., Markus, T., Maslanik, J. A., Cavalieri, D. J., Gasiewski, A. J., Heinrichs, J. F., Holmgren, J., Perovich, D. K., Sturm, M. (2006). Impact of surface roughness on AMSR-E sea ice products. *IEEE Transactions on Geoscience and Remote Sensing*, 44, 3103–3117, doi:10.1109/TGRS.2006.880619.

Stroeve, J. C., Serreze, M. C., Holland, M. M., Kay, J. E., Maslanik, J., and Barrett, A. P. (2012). The Arctic's rapidly shrinking sea ice cover: a research synthesis. *Climatic Change*, 110(3–4), 1005–1027, doi:10.1007/s10584-011-0101-1.

Strong, A. E. (1971). Mapping sea-surface roughness using microwave radiometry. *Journal of Geophysical Research*, 76, 8641–8648, doi:10.1029/JC076i036p08641.

Svendsen, E., Kloster, K., Farrelly, B., Johannessen, O. M., Johannessen, J. A., Campbell, W. J., Gloersen, P., Cavalieri, D., and Mätzler, C. (1983). Norwegian remote sensing experiment: Evaluation of the Nimbus 7 scanning multichannel microwave radiometer for sea ice research. *Journal of Geophysical Research: Oceans (1978–2012)*, 88(C5), 2781–2791, doi:10.1029/JC088iC05p02781.

Svendsen, E., Matzler, C., and Grenfell, T. C. (1987). A model for retrieving total sea ice concentration from a spaceborne dual-polarized passive microwave instrument operating near 90 GHz. *International Journal of Remote Sensing*, 8(10), 1479–1487, doi:10.1080/01431168708954790.

Thompson, D. R., Elfouhaily, T. M., and Chapron, B. (1998). Polarization ratio for microwave backscattering from the ocean surface at low to moderate incidence angles. *IEEE International Geoscience and Remote Sensing Symposium*, IGARSS '98, 3, 1671–1673, doi:10.1109/IGARSS.1998.692411.

Thorndike, A. S., Rothrock, D. A., Maykut, G. A., and Colony, R. (1975). The thickness distribution of sea ice. *Journal of Geophysical Research*, 80(33), 4501–4513, doi:10.1029/JC080i033p04501.

Thorpe, S. A. (2007). An Introduction to Ocean Turbulence. Cambridge University Press, Cambridge, UK. 240 p. [pdf]

Ting, C. -H., Babanin, A. V., Chalikov, D., and Hsu, T. -W. (2012). Dependence of drag coefficient on the directional spreading of ocean waves. *Journal of Geophysical Research*, 117, C00J14, doi:10.1029/2012JC007920.

Toffoli, A., Loffredo, L., LeRoy, P., Lefèvre, J. -M., and Babanin, A. V. (2012). On the variability of sea drag in finite water depth. *Journal of Geophysical Research*, 117, C00J25, doi:10.1029/2011JC007857.

Tonboe, R., and Toudal, L. (2005). Classification of new-ice in the Greenland Sea using satellite SSM/I radiometer and SeaWinds scatterometer data and comparison with ice model. *Remote Sensing of Environment*, 97(3), 277–287, doi:10.1016/j.rse.2005.05.012.

Touzi, R., Boerner, W. M., Lee, J. -S., and Lueneburg, E. (2004). A review of polarimetry in the context of synthetic aperture radar: concepts and information extraction. *Canadian Journal of Remote Sensing*, 30(3), 380–407, doi:10.5589/m04-013.

Trizna, D. B., and Carlson, D. J. (1996). Studies of dual polarized low grazing angle radar sea scatter in nearshore regions. *IEEE Transactions on Geoscience and Remote Sensing*, 34(3), 747–757, doi:10.1109/36.499754.

Trujillo, A. P., and Thurman, H. V. (2011). Essentials of oceanography, 10th edition, Pearson Prentice Hall, New Jersey, USA, 551 p. [pdf]

Ulaby, F. T., Moore, R. K., and Fung, A. K. (1986). Microwave remote sensing– Active and passive, Vol. III: From theory to applications, Artech House, Dedham, Massachusetts, 1120 p. [pdf]

Untersteiner, N. (1986). The Geophysics of Sea Ice. NATO ASI Series, Series B: Physics Vol. 146, Plenum Press, New York, 1196 p. [pdf]

Valenzuela, G. R. (1978). Theories for the interaction of electromagnetic and oceanic waves- A review. *Boundary-Layer Meteorology*, 13, 61–85, doi:10.1007/BF00913863.

Vandermark, D., Chapron, B., Sun, J., Crescenti, G. H., and Graber, H. C. (2004). Ocean wave slope observations using radar backscatter and laser altimeters. *Journal of Physical Oceanography*, 34(12), 2825–2842, doi:10.1175/JPO2663.1.

Wadhams, P. (1983). A mechanism for the formation of ice edge bands. *Journal of Geophysical Research*, 88 (C5), 2813-2818, doi:10.1029/JC088iC05p02813.

Wadhams, P. (1988). The underside of Arctic sea ice imaged by sidescan sonar. *Nature*, 333, 161–164, doi:10.1038/333161a0.

Wadhams, P., Squire, V. A., Goodman, D. J., Cowan, A. M., and Moore, S. C. (1988). The attenuation rates of ocean waves in the marginal ice zone. *Journal of Geophysical Research*, 93(C6), 6799–6818, doi:10.1029/JC093iC06p06799.

Wakabayashi, H., Matsuoka, T., Nakamura, K., and Nishio, F. (2004). Polarimetric characteristics of sea ice in the sea of Okhotsk by airborne L-band SAR. *IEEE Transactions on Geoscience and Remote Sensing*, 42, 2412–2425, doi:10.1109/TGRS.2004.836259.

Wang, H., Zhu, J., Yang, J., and Shi, C. (2012). A semiempirical algorithm for SAR wave height retrieval and its validation using Envisat ASAR wave mode data. *Acta Oceanologica Sinica*, 31, 59–66. doi:10.1007/s13131-012-0206-z.

Weeks, W. F. (2010). *On sea ice*. University of Alaska Press, Fairbanks, AK; 664 p. [pdf]

Wells, N. C. (2011). *The Atmosphere and Ocean: A Physical Introduction*, John Wiley and Sons Ltd., Oxford, UK, 448 p. [pdf]

Wiesmann, A., and C. Mätzler. (1999). Microwave emission model of layered snowpacks. *Remote Sensing of Environment*, 70, 307–316. doi:10.1016/S0034-4257(99)00046-2.

Williams, T. D., Bennetts, L. G., Squire, V. A., Dumont, D., and Bertino, L. (2013). Wave–ice interactions in the marginal ice zone. Part 1: Theoretical foundations. *Ocean Modelling*, 71, 81–91, doi:10.1016/j.ocemod.2013.05.010.

Wilheit, T. T. (1972). *The Electrically Scanning Microwave Radiometer (ESMR) experiment, Nimbus-5 User's Guide*. NASA Goddard Space Flight Center, Greenbelt, Maryland, 59–105.

Winebrenner, D. P., Farmer, L. D., and Joughin, I. R. (1995). On the response of polarimetric synthetic aperture radar signatures at 24-cm wavelength to sea ice thickness in Arctic leads. *Radio Science*, 30, 373–402, doi:10.1029/94RS02313.

Wohl, G. M. (1995). Operational sea ice classification from synthetic aperture radar imagery. *Photogrammetric Engineering & Remote Sensing*, 61, 1455–1462. [pdf]

Wu, J. (1979). Oceanic whitecaps and sea state. *Journal of Physical Oceanography*, 9, 1064–1068, doi:10.1175/1520-0485(1979)009%3C1064:OWASS%3E2.0.CO;2.

Yueh, S. H. (1997). Modeling of wind direction signals in polarimetric sea surface brightness temperatures. *IEEE Transactions on Geoscience and Remote Sensing*, 35, 1400–1418, doi:10.1109/36.649793.

Yueh, S. H., Kwok, R., and Nghiem, S. V. (1994). Polarimetric backscattering and emission properties of targets with reflection symmetry. *Radio Science*, 29(6), 1409–1420, doi:10.1029/94RS02228.

Zwally, H. J., Comiso, J. C., Parkinson, C. L., Campbell, W. J., Carsey, F. D., and Gloersen, P. (1983). *Antarctic Sea Ice, 1973-1976: Satellite Passive Microwave Observations*. NASA SP-459, National Aeronautics and Space Administration, Washington, DC. [pdf]